OBSERVATIONS WITH C-BASS

A thesis submitted to the University of Manchester
for the degree of Master of Science
in the Faculty of Engineering and Physical Sciences

2013

By

Rachana Bhatawdekar

School of Physics and Astronomy

Contents

Word count: 34858

List of Tables

List of Figures

Abstract

The C-Band All Sky Survey (C-BASS) is a project to image the whole sky at a frequency of 5 GHz, measuring both the brightness and the polarization of the sky. The principal aim of C-BASS is to allow the subtraction of polarized Galactic synchrotron emission from the data produced by Cosmic Microwave Background (CMB) polarization experiments such as *Planck*, Wilkinson Microwave Anisotropy Probe (*WMAP*) and future B-mode polarization experiments. Hence, it is important that the polarization be measured with utmost accuracy.

It is difficult to measure the Stokes parameters correctly because the degree of polarization in astronomical sources is typically small and the radioastronomical receiving system modifies the incoming polarization with instrumental effects. Thus, careful calibration of the polarimeter was a critical step in the development of C-BASS pipeline. In this thesis, calibration of the C-BASS polarimeter was achieved by both developing the polarization calibration module in the pipeline and applying it to the observations of the Orion (an unpolarized source) and Tau A (a polarized source) over a range of parallactic angles over a period of some hours with C-BASS telescope.

The data were reduced in the C-BASS data reduction pipeline. A baseline fit was performed on the reduced data and binned maps of 3 arcmin pixels for Stokes I, Q, U and V were made. Gaussian fits were made on Orion and Tau A maps to determine the flux of the Stokes parameters. Stokes Q and U for Tau A were also corrected for parallactic angle rotation. They showed the presence of leakage.

The binned maps of complete raster schedules were made in beam coordinates in order to determine the leakage parameters. The polarization beams in the maps were found to be not circular, and an offset in Stokes Q and U was also observed. This showed that at least some of the leakage is due to the optics and not the receiver. The observed polarization of Orion was found to be $\approx 2\%$. Since Orion is expected to be intrinsically unpolarized, this was attributed to leakage. A leakage correction was applied to Tau A maps using the leakage parameters derived from Orion and the maps were also corrected for parallactic angle rotation. The effectiveness of the correction process was then verified on Tau A by using Gaussian fitting and calculating polarized intensity, degree of polarization, and the position angle.

The raster schedule after calibration, for which this thesis presents a detailed analysis, shows a degree of polarization of $\Pi = 3.51 \pm 0.13\%$ and a position angle of $\chi = 138.44^\circ \pm 0.39^\circ$. At 5 GHz, a position angle of $141^\circ \pm 3^\circ$ and a degree of polarization between 3.5% and 4.5% is expected for Tau A. Our results are consistent with this.

Declaration

I declare that no portion of the work referred to in this thesis has been submitted in support of an application for another degree or qualification of this or any other university or other institute of learning.

Rachana Bhatawdekar

University of Manchester

Jodrell Bank Center of Astrophysics

Oxford Road

Manchester

Copyright

Acknowledgements

First and foremost, I would like to thank Dr. Patrick Leahy not only for giving me the opportunity to work in his project but also being a great mentor. Without his guidance, discussions and persistent help, this dissertation would not have been possible. I would also like to thank Dr. Clive Dickinson for his guidance in my research.

Secondly, I would like to thank Saurabh for supporting me with my decision of switching fields, from Information Technology industry to Astrophysics, to pursue my childhood dream.

I would also like to thank other postgraduate students, David Boulderstone, Philippa Hartley, Andrew Jones, Constantinos Demetroullas and Nicholas Wrigley for their support and encouragement. Carl Roberts, Sarah Keith and Indy Leclercq, thank you for all the help with proof reading.

Lastly, a massive thanks to PhD student Melis Irfan, who helped me understand C-BASS and without whom I would have never pulled this off.

Thank you all, this was a great experience.

Rachana Bhatawdekar

Jodrell Bank Centre for Astrophysics,

Alan Turing Building,

University of Manchester,

Oxford Road,

Manchester,

M13 9PL.

Supervisor : Dr. Patrick Leahy

Nomenclature

ΛCDM	Lambda Cold Dark Matter
AME	Anomalous Microwave Emission
BICEP	Background Imaging of Cosmic Extragalactic Polarization
BOOMERanG	Balloon Observations Of Millimetric Extragalactic Radiation ANd Geophysics
C-BASS	C-Band All-Sky Survey
CAPMAP	Cosmic Anisotropy Polarization Mapper
CBI	Cosmic Background Imager
CMB	Cosmic Microwave Background
COBE	Cosmic Background Explorer
COSMOSOMAS	COSMOlogical Structures On Medium Angular Scales
DASI	Degree Angular Scale Interferometer
DEC	Declination
DESCART	DE-Striping CARTographer
DMR	Differential Microwave Radiometer
DOE	Department of Energy

DRAO	Dominion Radio Astrophysical Observatory
ESA	European Space Agency
FIR	Far Infrared
FIRAS	Far Infrared Absolute Spectrophotometer
FITS	Flexible Image Transport System
FPGA	Field Programmable Gate Array
FR	Faraday Rotation
FWHM	Full Width at Half Maximum
HA	Hour Angle
HartRAO	Hartebeesthoek Radio Astronomy Observatory
HEALPix	Hierarchical Equal Area isoLatitude Pixelation
IAU	International Astronomical Union
IDL	Interactive Data Language
IRAS	Infrared Astronomical Satellite
ISD	Interstellar Dust
JD	Julian Date
L2C	Linear-To-Circular Converter
LAT	Latitude
LFI	Low Frequency Instrument
LNA	Low Noise Amplifier
LON	Longitude

LSS	Last Scattering Surface
LST	Local Sidereal Time
LTE	Local Thermal Equilibrium
MATLAB	Matrix Laboratory
MJD	Modified Julian Date
NaN	Not-a-Number
NASA	National Aeronautics and Space Administration
NCP	North Celestial Pole
NSF	National Science Foundation
OMT	Orthogonal Mode Transducer
OVRO	Owens Valley Observatory
PPARC	Particle Physics and Astronomy Research Council
QUaD	QUEST at DASI
QUIET	Q/U Imaging ExperimenT
RA	Right Ascension
RF	Radio Frequency
RFI	Radio Frequency Interference
RMS	Root Mean Square
S-Z	Sunyaev-Zeldovich
SHASSA	Southern H-alpha Sky Survey Atlas
UV	Ultra Violet

VLBI	Very Long Baseline Interferometry
VSA	Very Small Array
VTSS	Virginia Tech Spectral-Line Survey
WCS	World Coordinate System
WHAM	Wisconsin H-alpha Mapper
WMAP	Wilkinson Microwave Anisotropy Probe

Chapter 1

Introduction

The C-BASS is a project to image the whole sky at a wavelength of six centimetres (a frequency of 5 GHz), measuring both the brightness and the polarization of the sky. It will produce all-sky maps of both the total intensity and polarized synchrotron radiation emitted by our Galaxy in the C-Band, which will be used primarily in the subtraction of Galactic foregrounds from measurements of the polarized component of the CMB.

I begin this chapter with an introduction to the Cosmic Microwave Background in Section 1.1. Section 1.2 will focus on the four diffuse Galactic foreground components that contaminate the CMB signal - synchrotron, free-free, thermal dust and anomalous emission. Section 1.3 gives a brief introduction to single dish astronomy, emphasising why a single dish is perfect for C-BASS. As my contribution to the project is in the polarization calibration of C-BASS, I conclude the chapter in Section 1.4 with fundamental polarization concepts and the importance of polarization calibration.

1.1 Cosmic Microwave Background

The Cosmic Microwave Background is by far the most powerful cosmological probe (Planck Collaboration et al., 2013b). In 1965 Arno Penzias and Robert Wilson (Penzias & Wilson, 1965), while measuring reflected signals from communication

satellites at $\lambda = 7.35$ cm using a microwave antenna at Bell labs, realised the existence of an 'excess noise'. They tried everything to reduce the noise, but the excess signal was isotropic, unpolarised and constant with time i.e., not associated to any particular astronomical source — they had detected the Cosmic Microwave Background Radiation.

In the Big Bang model, the CMB arises naturally. If mass is conserved in the expansion, then in the past the Universe was denser and hotter. Consider an early dense Universe with $T > 10^4$ K. In such hot conditions, the baryonic matter was fully ionised. There will be scattering between free electrons and photons resulting in an opaque Universe. A dense, hot and opaque body produces blackbody radiation. As the Universe expanded and cooled, at $T \sim 3000$ K, the ionised baryonic component becomes neutral and atoms are formed; this is the epoch of recombination. When the number of free electrons dropped sufficiently, the photons stop interacting with electrons and the Universe becomes transparent; this is termed as photon decoupling ($z \approx 1100$ and $t \backsimeq 350,000$ years). The time when a typical CMB photon has its last scattering from an electron is the last scattering time, and is same as the photon decoupling epoch. Surrounding every observer in the Universe is the last scattering surface (LSS). CMB photons have been travelling from the LSS without any further scattering. Due to the expansion of the Universe there is a drop in CMB temperature and increase in the wavelength.

In 1992, the *COBE* satellite (Smoot et al., 1992) revealed that at any position on the sky, the CMB spectrum is very close to that of a blackbody, and the CMB mean temperature averaged over all locations is:

$$< T >= \frac{1}{4\pi} \int T(\theta, \phi) \sin\theta d\theta d\phi = 2.725 \text{ K} . \tag{1.1}$$

This essentially means that the CMB spectrum is well fitted to a blackbody spectrum with temperature $T = 2.725 \pm 0.001$ K (Fixsen, 2009) (see Fig. 1.1).

The Planck formula for black body intensity radiation is:

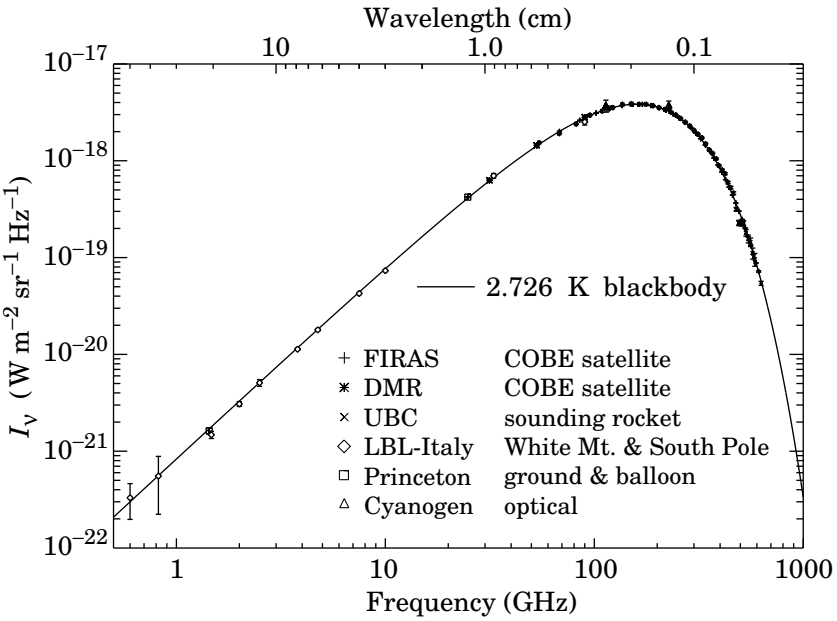

Figure 1.1: CMB spectrum measurements from various experiments (Smoot, 1997).

$$B_\nu = \frac{2kT\nu^2}{c^2}\left[\frac{h\nu/kT}{e^{h\nu/kT}-1}\right] \ , \tag{1.2}$$

where B_ν is brightness temperature, k is the Boltzmann constant, h is the Planck constant and c is the speed of light.

In the Rayleigh-Jeans approximation where $h\nu << kT$, the formula reduces to:

$$B_\nu = \frac{2kT\nu^2}{c^2} = \frac{2kT}{\lambda^2} \ . \tag{1.3}$$

As shown in Fig. 1.1, the ground-based data taken by Penzias and Wilson are on the classical i.e., Rayleigh-Jeans part of the spectrum. The CMB spectrum peaks at ~ 2 mm.

In addition to the above, *COBE* also found that the CMB temperature is extremely smooth across the sky. It varies by about 1 part in 10^5 between different directions. The CMB also has a dipole distortion in temperature because of the doppler shift due to motion of *COBE* (and Earth) relative to a frame where the

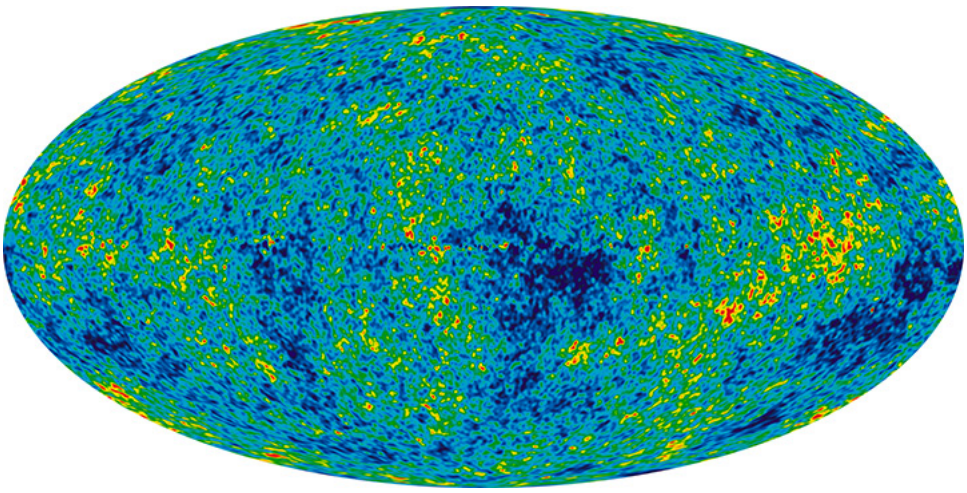

Figure 1.2: *WMAP* map of CMB anisotropies (Image taken from http://map.gsfc.nasa.gov/).

CMB is isotropic. After subtracting the dipole distortion and the Galactic emission contributions, mainly from dust, free-free and synchrotron emission in the Milky way, tiny temperature fluctuations still remain. These residual CMB temperature fluctuations are called the CMB anisotropies. CMB anisotropies represent the seeds for the structure formation in the Universe. These anisotropies detected by *COBE* prove that the CMB is in fact not isotropic. Another satellite, *WMAP* (Bennett et al., 1997), which had an angular resolution of $\sim 0.25^{\circ}$ (better than *COBE* that had an angular resolution of $\sim 7^{\circ}$) was launched to measure these anisotropies and to confirm the fluctuations that *COBE* had detected. Fig. 1.2 shows the *WMAP* map of the CMB anisotropies. These temperature fluctuations are of the order 1 part in 10^5.

The fluctuations are thought to have been generated within 10^{-35} seconds of the Big Bang, and so by studying CMB anisotropies we probe fundamental physics at energy scales many orders of magnitude higher than those accessible to particle accelerators on Earth. CMB anisotropies can be used to fix the values of many of the key parameters that define our Universe, in particular, its geometry, age, and composition (The Planck Collaboration, 2006).

However, much more information about the Universe remains to be extracted from the CMB, especially its polarization. In particular, CMB measurements with

high angular resolution and sensitivity are required to determine the initial conditions for structure evolution, the origin of primordial fluctuations, the existence of topological defects, and the nature and amount of dark matter. CMB polarization is being measured by several current and future ground-based and balloon-borne experiments supported by NSF, NASA, DOE and other agencies. A major goal for these experiments is to measure the B-mode polarization signal, which is expected to provide information about the epoch of inflation - in particular, the energy scale of inflation - and about the physics at grand unification theories (The Planck Collaboration, 2006).

The most recent satellite CMB experiment is the *Planck* mission (Tauber et al., 2010; Planck Collaboration et al., 2011) led by the European Space Agency (ESA). This is the fourth space CMB mission after RELIKT (Strukov & Skulachev, 1984), *COBE* and *WMAP*, and was designed to extract essentially all information available in the temperature anisotropies to an accuracy set by fundamental astrophysical limits, and measure the CMB polarization. To do this, *Planck* was launched on 14 May 2009 to image the the whole sky with an unprecedented combination of sensitivity ($\triangle T/T \sim 2 \times 10^{-6}$), angular resolution (to $5'$), and frequency coverage (30–857 GHz). The *Planck* mission has mapped the full sky at nine frequencies from 30 to 857 GHz (Planck Collaboration et al., 2013a).

However, the CMB intensity and the polarization that are its prime targets are contaminated by foreground emission. Foregrounds are basically anything that emits radiation and that can contaminate the CMB signal. This contamination originates from diffuse Galactic emission, unresolved point sources and the Sunyaev-Zeldovich (S-Z) effect.

There are four diffuse Galactic foreground components — synchrotron, free-free, thermal dust and anomalous emission. The synchrotron emission is caused by the acceleration of relativistic electrons through the Galactic magnetic field, free-free or Bremsstrahlung emission is caused by ions accelerating electrons, thermal emission is from the vibration of dust grains and anomalous emission is due to spinning dust

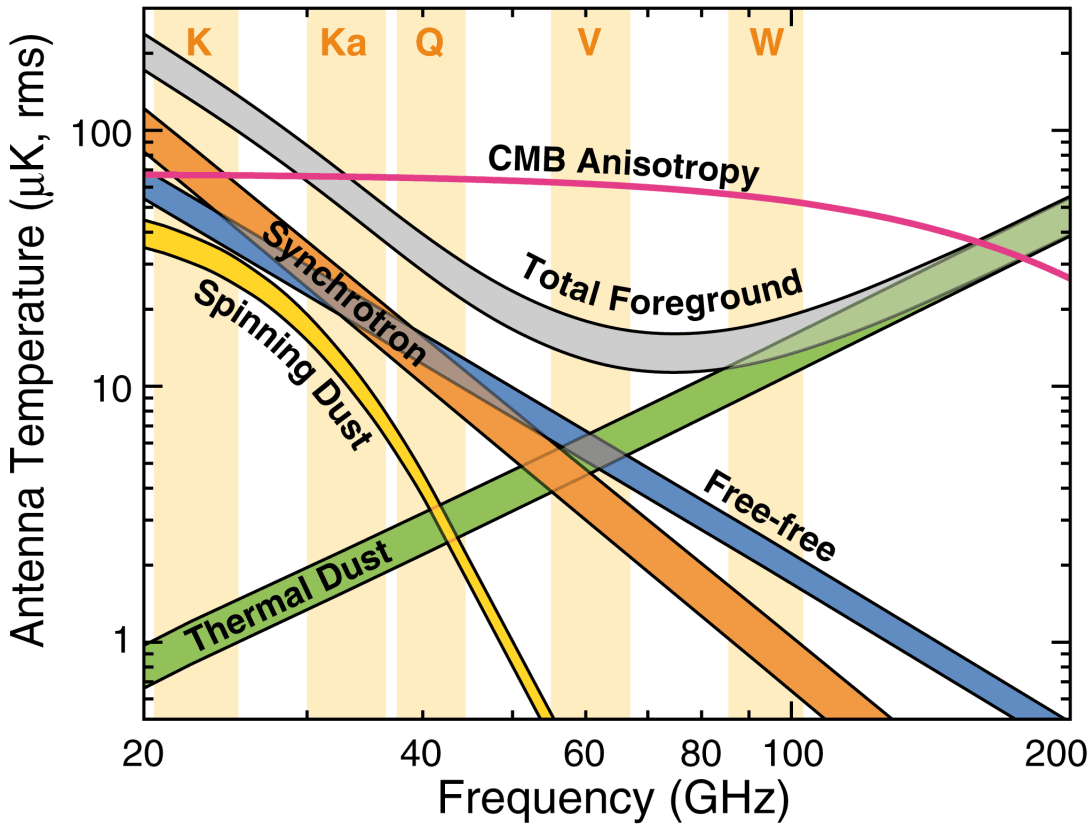

Figure 1.3: Spectra of CMB and foreground anisotropy (Bennett et al., 2012).

grains. Fig. 1.3 shows the root mean square (RMS) anisotropy as a function of frequency from the CMB and sources of foreground emission: synchrotron, free-free, spinning dust, and thermal dust emission.

In addition to the Galactic foregrounds, extragalactic point sources also contaminate the CMB signal. Extragalactic point sources are one of the most menacing foregrounds, for several reasons: (a) Their spectral index varies much more than that of other foregrounds. (b) Many sources exhibit substantial time variability. (c) Their abundance is very poorly known over much of the CMB frequency range (Tegmark & de Oliveira-Costa, 1998).

The Sunyaev–Zel'dovich effect is the result of high energy electrons distorting the cosmic microwave background radiation through inverse Compton scattering, in which low energy CMB photons receive an average energy boost during collision

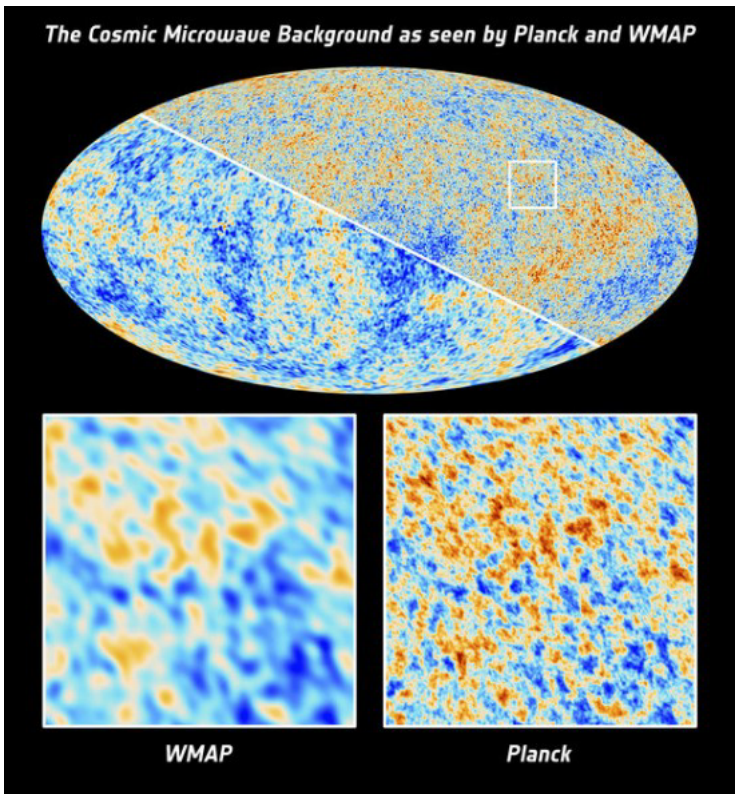

Figure 1.4: The cosmic microwave background as seen by *WMAP* and *Planck* (Image taken from http://sci.esa.int/).

with the high energy electrons. This interaction is most evident in the case of clusters of galaxies because they are so massive (Sunyaev & Zeldovich, 1980). The intensity of cosmic background radiation in the direction of a cluster of galaxies is altered by the inverse-Compton effect. In essence, the Sunyaev-Zel'dovich effect is a signature left in the cosmic microwave background by collapsed structures containing baryons. Although not strictly a foreground, the S-Z effect does interfere with CMB photons, changing CMB observations and rendering them untrue to their intrinsic form. Therefore, the S-Z effect will have to be accounted for and removed from any CMB measurements.

Since *Planck* is designed to recover the CMB signal at the level of a few microkelvin per resolution element of $5'$, it is of utmost importance that the foregrounds are well understood in order to recover the full potential of these sensitive measurements. Fig. 1.4 shows the cosmic microwave background as seen by *WMAP* and *Planck*.

1.2 Diffuse Foreground Emission

1.2.1 Free-Free Emission

Free-free or Bremsstrahlung originates from the acceleration of a charge (e.g., an electron) in Coulomb collisions with other charges (e.g., ions or nuclei). The most common situation is the emission from a hot interstellar medium as the electrons collide with the nuclei due to their random thermal motions. The electron is unbound both before and after the collision, hence the term free-free.

Radio free-free continuum and Hα emission are both generated in the ionized interstellar medium. While ionized hydrogen and helium are both responsible for radio continuum, only ionized hydrogen produces the Hα emission. Optical and radio emission both are functions of electron temperature T_e (Rybicki & Lightman, 1979; Dickinson et al., 2003).

Free-free thermal emission has antenna temperature $T_A \sim \nu^\beta$ high-frequency ($\nu > 10$ GHz) spectrum with spectral index $\beta \approx -2.15$, and a low-frequency rise of $T_A \sim \nu^2$ due to optically thick self-absorption (Rybicki & Lightman, 1979; Bennett et al., 2003b). It is a prominent foreground at frequencies between $\nu = 10$–100 GHz. This is the region where many microwave CMB experiments operate, e.g. DASI, CBI, VSA, *WMAP*, *Planck* (Bennett et al., 1997; Kovac et al., 2002; Mason et al., 2003; Grainge et al., 2003; Planck Collaboration et al., 2013a). The optical Hα line is a good tracer of free-free emission although it requires corrections for dust absorption (Dickinson et al., 2003).

Valls-Gabaud (1998) provide a useful and accurate expression for the Hα intensity based on data from Hummer & Storey (1987), when the emitting medium is optically thick in units of erg cm^{-2}s^{-1}sr^{-1}:

$$I(H\alpha) = 9.41 \times 10^{-8} T_4^{-1.017} 10^{-0.029/T_4} \times (EM)_{\mathrm{cm}^{-6}\mathrm{pc}} \, . \tag{1.4}$$

Here, Emission Measure $EM = \int n_\mathrm{e} dl$, where n_e is the electron density and dl is the path length. T_4 is the electron temperature in the units of 10^4 K.

In the free-free collision, the time for emitting most of the radiation in the radio spectrum is so brief that the acceleration can be approximated by delta function. However, a full calculation requires a summation over all directions, impact parameters, and velocities (Burke & Smith, 2002).

The free-free radio continuum emission for an ionized gas at T_e <550,000 K in Local Thermal Equilibrium (LTE) in terms of a volume emissivity in units of erg $\mathrm{cm}^{-3}\mathrm{s}^{-1}\mathrm{Hz}^{-1}$ is given by (Oster, 1961):

$$\epsilon_\nu^{\mathrm{ff}} = 6.82 \times 10^{-38} Z^2 n_{\mathrm{e}} n_{\mathrm{ion}} T_{\mathrm{e}}^{-1/2} e^{-h\nu/kT} \left\langle \bar{g_{\mathrm{ff}}} \right\rangle \ , \tag{1.5}$$

where $\left\langle \bar{g_{\mathrm{ff}}}\left(Z, \nu, T_{\mathrm{e}}\right)\right\rangle$ is the velocity-averaged Gaunt factor, n_{e} is the electron density, n_{ion} is the ion density with charge number Z per ion. The Gaunt factor comprises all the terms by which the quantum mechanical expressions differ from the classical ones.

The exact form, Eq. 1.5 above, has an exponential cutoff at the high-energy, short-wavelength end of the spectrum, expressing the fact that a colliding electron cannot emit more energy than it possess (Burke & Smith, 2002).

A practical form of this equation, at radio wavelengths, for temperature T_4 measured in units of 10^4 K and frequency in GHz, in units erg $\mathrm{cm}^{-3}\mathrm{sr}^{-1}$ is:

$$j_\nu \approx 3.0 \times 10^{-37} Z^2 n_{\mathrm{e}} n_{\mathrm{i}} T_4^{1/2} \left[13.2 + \ln\left(\frac{T_4^{3/2}}{Z \nu_{\mathrm{GHz}}} \right) \right] \ . \tag{1.6}$$

Due to Thomson scattering the free-free polarisation is expected to be at 10% maximum, but typically it will be much less than that (Davies & Wilkinson, 1999).

So far, the main Hα surveys are the Wisconsin H-alpha Mapper (WHAM) (Reynolds et al., 2002), the Virginia Tech Spectral-Line Survey (VTSS) (Dennison et al., 1998) and the Southern H-alpha Sky Survey Atlas (SHASSA) (Gaustad et al., 2001).

Finkbeiner (2003) assembled a full sky Hα map using data from the WHAM, the VTSS and SHASSA, with the Schlegel et al. (1998) extinction map of the sky,

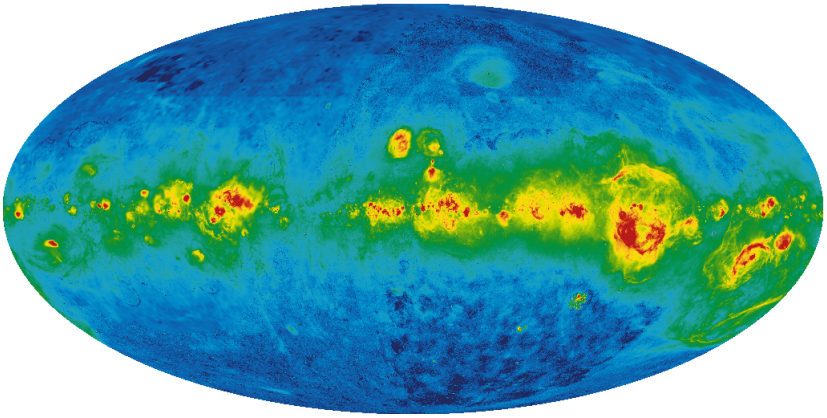

Figure 1.5: A Hα map of the sky corrected for extinction (Image taken from http://lambda.gsfc.nasa.gov/).

as shown in Fig. 1.5.

1.2.2 Synchrotron Emission

Synchrotron emission results from relativistic electrons spiralling around magnetic field lines and dominates at frequencies up to a few GHz with a spectral index $\left(T \propto \nu^{-\beta}\right)$ of $\beta \approx 2.7$–3.2 (Davies et al., 1996). It is seen to extend well above the plane - e.g. the North Polar Spur which extends to Galactic latitude $b \approx 80°$ (Haslam et al., 1982; Reich & Reich, 1988; Jonas et al., 1998).

The frequency of emission is directly related to how fast the electron is travelling. This can be related to the initial velocity of the electron and the strength of the magnetic field. The spectrum of synchrotron emission results from summing the emission spectra of individual electrons (see Fig. 1.6). As the electron spirals around the magnetic field, it emits radiation over a range of frequencies peaking at the critical frequency. The longer the electron travels around the magnetic field, the more energy it loses, the narrower the spiral it makes, and the longer the wavelength of the critical frequency. By summing the spectra from the individual electrons we find that synchrotron emission has a characteristic spectrum, where flux steadily declines with frequency according to the relation:

$$F \sim \nu^{\alpha} \ . \tag{1.7}$$

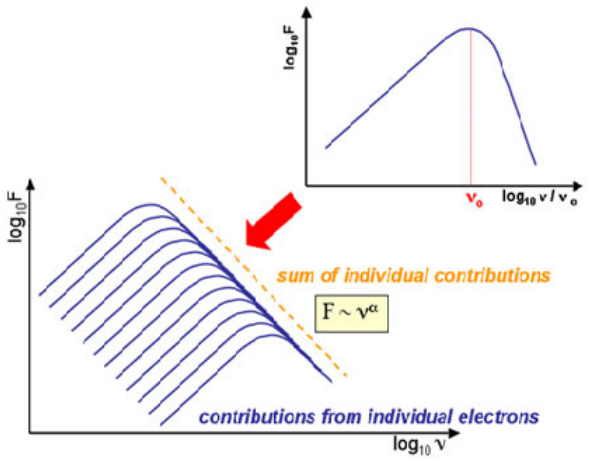

Figure 1.6: The synchrotron emission spectrum follows a power-law decay, and is constructed by adding the contributions from individual electrons (Image taken from http://astronomy.swin.edu.au/cosmos/S/Synchrotron+Emission).

Here F is flux, ν is frequency and α is the spectral index.

The strength of the Galactic magnetic field is such that to maintain synchrotron radiation a continual supply of relativistic electrons is necessary. Typically these are supplied by very powerful energy sources such as supernova remnants. The stars that form supernova remnants also emit UV (Ultra Violet) radiation responsible for the heating of dust grains and ionization of hydrogen in the interstellar medium, and hence synchrotron emission is associated with the star-formation cycle (Bennett et al., 2003b).

Although non-thermal radiation was observed from the Galaxy with the advent of radio astronomy, there was not any clear evidence of its origin. K.O. Kiepenheuer showed that the intensity of the non-thermal Galactic radio emission can be understood by the radiation from relativistic cosmic ray electrons moving in interstellar magnetic field. He found that a field of 10^{-6} Gauss (10^{-10} Tesla) and relativistic electrons of energy 10^9 eV would give about the observed intensity (Smoot, 1999).

An electron moving in a magnetic field B will radiate. For non-relativistic electrons the radiation is called cyclotron radiation and its emission frequency is the

frequency of gyration of the electron in the magnetic field. The cyclotron or (gyration frequency) ω_B in Gaussian units is:

$$\omega_B = \frac{eB}{\gamma mc} \ , \tag{1.8}$$

where e is the electron charge, m is the mass of electron and $\gamma = \frac{1}{\left[1-\frac{v^2}{c^2}\right]^{1/2}}$ is the Lorentz factor.

For extreme relativistic ($\gamma \gg 1$) electrons the frequency spectrum extends to many times the gyration frequency and is called synchrotron radiation. For the extreme relativistic case, the emission spectrum is described by a critical frequency:

$$\omega_c \equiv \frac{3}{2}\gamma^2 \omega_B \sin\alpha = \frac{3\gamma^2 eB}{2mc} \sin\alpha \ . \tag{1.9}$$

The total rate of radiated power by a relativistic electron moving at an angle α to the direction of the field B is (Burke & Smith, 2002):

$$P = \frac{2e^4\gamma^2 B^2 \left(\sin\alpha\right)^2}{3m^2c^3} \ . \tag{1.10}$$

An ensemble of cosmic ray electrons will have different pitch angles and energies E and hence for an isotropic distribution of velocities an average over all angles must be taken. Thus, for an isotropic electron distribution, a highly relativistic electron radiates at the rate:

$$P = \left(\frac{2}{3}\right)^2 r_0^2 c\gamma^2 B^2 = \frac{4}{3}\sigma_T c\gamma^2 U_B \ , \tag{1.11}$$

where $\sigma_T = (8\pi/3)r_0^2$ is the Thomson cross section, $U_B = B^2/8\pi$ is the energy density in magnetic field and r_0 is the classical electron radius e^2/mc^2.

If the electrons' direction of motion is random with respect to the magnetic field, and the electrons' energy spectrum can be approximated as a power law $N(E)dE \propto E^{-p}dE$, where $N(E)$ is the energy distribution, E is the electron energy and p is the spectral index of the energy distribution, then the intensity is given by (Smoot,

1999):

$$I(\nu) = \frac{\sqrt{3}e^3}{8\pi mc^2}\left(\frac{3e}{4\pi m^3c^5}\right)^{(p-1)/2} LN_0B^{(p+1)/2}\nu^{-(p-1)/2}a(p)\ , \qquad (1.12)$$

where $a(p)$ is a weak function of the electron energy spectrum, L is the length along the line of sight through the emitting volume, B is the magnetic field strength, and ν is the frequency. If $N(E)$ varies across the Galaxy, the observed structure of synchrotron sky maps will change considerably with frequency (Bennett et al., 2003b).

Eq. 1.12 shows that the synchrotron flux density spectral index α is related to the electron power law index p by $\alpha = -(p-1)/2$ at frequencies greater than a few 10's of MHz where the self-absorption is negligible. However, at the lowest frequencies synchrotron self-absorption predicts an intensity that increases as $\propto \nu^{5/2}$ (Smoot, 1999).

Synchrotron emission is highly polarized $\sim 75\%$. This is because when the relativistic electron gas is contained in an ordered magnetic field, the electrons in every energy range will produce linearly polarized radiation. For a power-law distribution of index p, the resulting polarization for an isotropic pitch angle distribution is (Burke & Smith, 2002) :

$$\prod = \frac{p+1}{p+7/3}\ . \qquad (1.13)$$

For a typical spectral index of -2.5, the resultant degree of polarization will be 0.72. However, this is almost never observed due to the fact that Faraday rotation (FR) ($\propto \lambda^2$) and non-uniform magnetic field directions along the line of sight reduce the degree of polarization to $< 20\%$ (Bennett et al., 2003b).

Fig. 1.7 shows the 408 MHz sky dominated by synchrotron emission (Haslam et al., 1982).

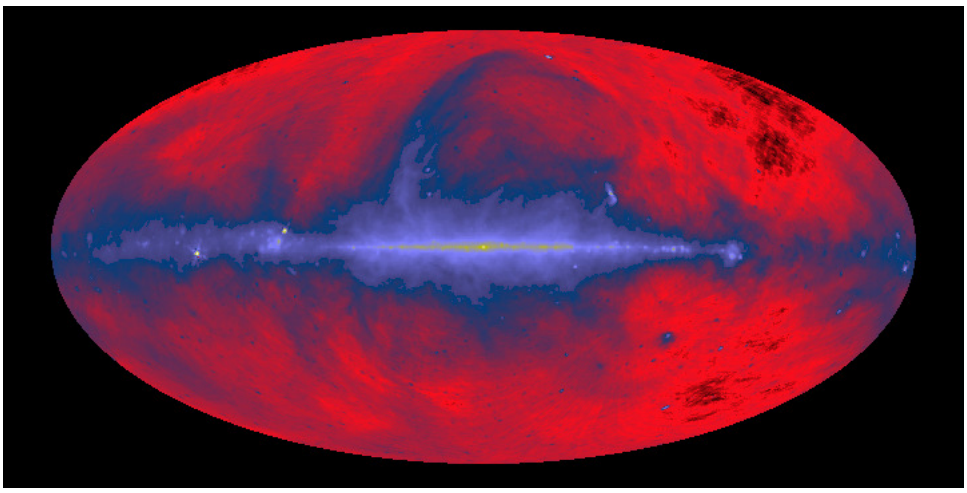

Figure 1.7: The Haslam 408 MHz sky map dominated by synchrotron emission (Haslam et al., 1982).

1.2.3 Thermal Dust Emission

At frequencies above ~ 100 GHz the diffuse emission of our Galaxy is dominated by thermal radiation from large dust grains, heated by the interstellar radiation field to a temperature $T_d \sim 10$–30 K (Masi et al., 2001). The emission is described as a modified black body, rising with frequency in the microwave band. The interstellar dust (ISD) is distributed in filamentary "cirrus"-like clouds and covers the sky even at high Galactic latitudes (Low et al., 1984). The spectrum of this component in the 300–3000 GHz range has been mapped with coarse (7°) angular resolution and high sensitivity by the *COBE-FIRAS* experiment (Wright et al., 1991).

The large dust grains dominate the total dust mass, as well as the observed emission in the far-infrared (FIR) domain (Draine & Li, 2007). They radiate in thermal equilibrium with the interstellar radiation field, and their emission spectrum, assuming fixed dust abundance and a single grain size, is well approximated by:

$$I_\nu \propto \epsilon \left(\frac{\lambda}{\lambda_0}\right)^\beta B_\nu\left(\lambda, T_d\right) \ , \tag{1.14}$$

$$B_\nu = \frac{2h\nu^3}{c^2} \frac{1}{e^{\frac{h\nu}{kT_d}} - 1} \ , \tag{1.15}$$

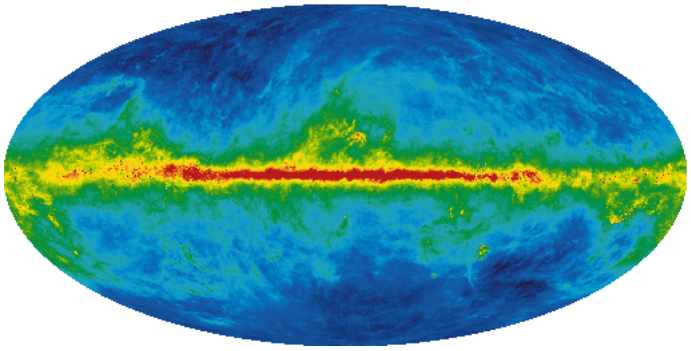

Figure 1.8: The FDS (Finkbeiner, Davis and Schlegel) dust map at 94 GHz based on data from *IRAS* and *COBE* (Bennett et al., 2003b).

where I_ν is the specific intensity or brightness, B_ν is the Planck function, T_d is the dust temperature, ϵ is the emissivity at wavelength λ_0 and β is the emissivity spectral index. Measurements of the thermal dust spectral index generally lie in the range $1.5 \leq \beta \leq 2$ (Paradis et al., 2010).

Thermal dust emission has been mapped over the full sky in several infrared bands, by the *COBE*, *IRAS* (Neugebauer et al., 1984) and *Planck* missions. A full sky template is provided by Schlegel et al. (1998) and is extrapolated in frequency by Finkbeiner et al. (1999) as shown in Fig. 1.8.

A remarkably tight correlation exists between the far-infrared and synchrotron emission of galaxies. Bicay et al. (1989) comment that the synchrotron emission appears spatially smeared relative to the far-infrared distribution in galaxies and they suggest that this likely arises from the diffusion and/or convection of the cosmic ray electrons from their original site of star formation activity.

The grains are magnetized and get aligned locally with the direction of the Galactic magnetic field making the overall emission polarized. The level of polarisation varies from 5 up to 10% on average (Benoît et al., 2004).

1.2.4 Anomalous Dust Emission

In addition to thermal emission from dust, there are various other ways in which dust can radiate at microwave wavelengths. These include electric dipole emission from spinning dust grains and magnetic dipole emission from thermally fluctuating

dust grains (Erickson, 1957; Draine & Lazarian, 1998a,b, 1999).

There is clear evidence for some excess emission, i.e. anomalous emission, which is correlated with dust. It has a rising spectral index towards lower frequencies and a much larger signal than would be expected from thermal dust emission alone in the frequency range 14.5–90 GHz (de Oliveira-Costa et al., 2002). The origin of this emission is still debated; however, the currently favoured explanation is that it is due to very small, rapidly spinning dust grains, which have a peak emission at around 20–30 GHz (Draine & Lazarian, 1998a,b).

Kogut et al. (1996b,a) proposed that the emission was a superposition of thermal dust and free-free emission, which could explain the slope of the observed spectrum (rising signal towards lower frequencies). They disregarded a contribution from synchrotron emission due to the lack of any correlation with the synchrotron templates.

de Oliveira-Costa et al. (1997) and Leitch et al. (1997) carried out observations that supported the superposition theory. However, due to lack of Hα emission, Leitch et al. (1997) inferred that any free-free emission occurring must be originating from a gas of temperature $\geq 10^6$ K.

Draine & Lazarian (1998a,b) calculated that the observed emission would require an energy input rate at least 100 times larger than that provided by a supernova so discarded the superimposition theory proposed by Kogut et al. (1996b,a). To explain this anomalous emission they proposed a model based on very small, rapidly rotating grains, which can be crudely modelled by assuming the equipartition of the rotational degrees of freedom as follows:

$$\frac{1}{2}I\omega^2 = kT \ , \tag{1.16}$$

where I is the moment of inertia, k is Boltzmann's constant and T is the temperature.

For a spherical and homogeneous grain, with $I = \frac{2}{5}mR^2$, radius $R = N \times 10^{-10}$ m, and a mass density $\rho = 1$ kg m^{-3}, the rotational frequency is $\nu = 2 \times 10^3 \sqrt{\frac{T}{N^5}}$ GHz, where N is the number of atoms in the radius. A typical dust temperature is

$T \sim 25$ K, and a very small grain cannot be much less than 100 atoms in radius (so $N = 10^2$), therefore $\nu \sim 30$ GHz (Casassus et al., 2005).

This theory has a spectrum which peaks at 20–30 GHz and then rolls off to either side. The experimental results carried out by de Oliveira-Costa et al. (1999) showed that there was indeed a peak in the spectrum and a turnover at lower frequencies providing a clear evidence for spinning dust theory.

More support for the theory came from Finkbeiner et al. (2002) who observed a rising spectrum at very low frequencies in two regions (later discovered it was only one region by Dickinson et al. (2006)) using the Green Bank telescope, providing the first evidence for the anomalous emission in actual physical regions, rather than just a statistical measurement over large regions of the sky. Banday et al. (2003) used the all sky Hα map by Dickinson et al. (2003) to subtract the free-free component from the COBE DMR (Kogut et al., 1996b) data, and found that the main emission component was anomalous emission.

Battistelli et al. (2006) used the COSMOSOMAS experiment to detect the polarisation of the anomalous emission that Watson et al. (2005) had detected in the Perseus molecular complex and found a total polarisation level of $\prod = 3.4^{+1.8}_{-1.9}\%$, which is consistent with emission from spinning dust whose polarization is limited to $\sim 5\%$. Dickinson et al. (2011) derived new constraints on the polarization of anomalous microwave emission (AME) in nearby molecular clouds and it is found to be limited to $\lesssim$ 1–2%.

1.3 Single dish radio astronomy

In this section I will describe the basic fundamentals of radio astronomy and interferometry with particular emphasis on why a single dish is well suited for C-BASS.

1.3.1 Single dish and interferometers

Radio astronomy is carried out using large radio antennas referred to as radio telescopes either used singularly or with multiple linked telescopes applying the techniques of radio interferometry and aperture synthesis. All radio telescopes must meet two basic requirements: sensitivity and angular resolution. Sensitivity depends on having the largest collecting area possible whereas the basic relation between the angular resolution - the ability of a radio telescope to distinguish fine detail in the sky - and the aperture of a telescope, is given by:

$$\theta \approx \frac{\lambda}{D} \ , \tag{1.17}$$

where λ is the wavelength of observations and D is the size of the telescope. However, it is not possible to increase a telescope's diameter beyond a certain limit to achieve greater resolution (the weight of the reflector and its support structure has set a practical limit of about 100 metres for fully steerable parabolic single dishes).

Since the collecting area puts a limit on the resolution of a telescope, a technique called interferometry, which combines multiple radio antennas to form a single antenna with a far greater collecting area than the individual components, is employed. With interferometry, high angular resolution is achieved, as the resolving power of an interferometer is set by the distance between its components, instead of the size of its components. The distance between the antennas and the rotation of the Earth results in differences in the observed path length from the object under observation. An interference pattern is generated when the data from each of the antennas is combined, and it can be reconstructed to form an image of the observation. It may appear that interferometers would be the ideal tool for performing radio astronomy, and in some cases this is true.

In Fig. 1.9, a parabolic single dish brings an incoming wavefront from a fixed source in the sky to the receiving element at the prime focus. The parabolic shape ensures that all the signals across the wavefront arrive at the focus in phase with

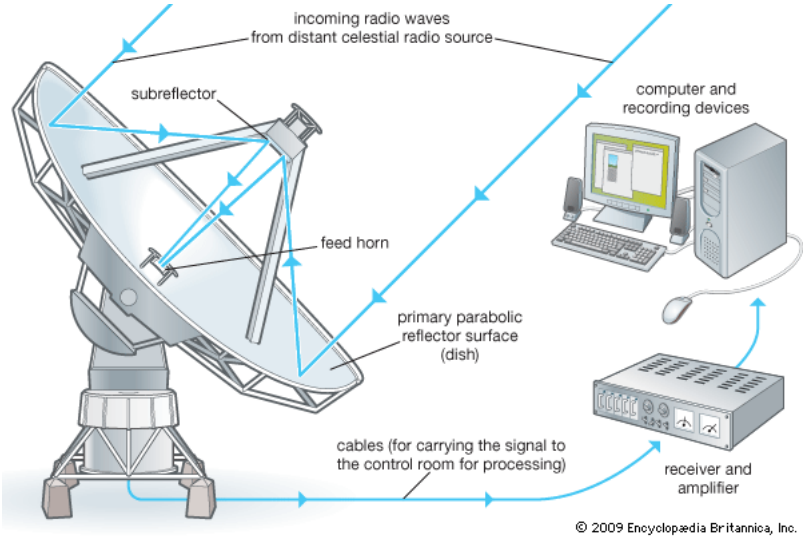

Figure 1.9: A schematic of radio telescope system (Image from http://media-2.web.britannica.com/eb-media/34/4634-004-F96BF4A3.gif.).

each other. At the focal point there is a feed to receive the radiation and a receiver which is nothing but an amplifier followed by a detector. The detector is a square law detector which converts the amplified voltage into power. This is averaged or integrated and hence we measure the average power coming into the antenna from a specified direction.

Fig. 1.10 differs from a parabolic reflector in that a cable brings the incoming signals from the independent dipoles to the focus. Here the voltages are first added before being amplified and detected in the receiver. If we want to observe a source which is directly overhead, and if the lengths of each cable from the dipole to the receiver are all same, then all the individual signals will arrive exactly in phase at the receiver. In order to look at a different point in the sky we could simply make the cables to each dipole of different lengths, such that the dipoles closer to the source have a longer cable to travel through from the ones further away. If the lengths are correct then signals from the desired point will arrive at the receiver in phase and those from overhead will not. The cables from the dipoles to the receiver, however, will have loss and so we need to amplify the signal at each dipole before sending it to the cable. The amplifiers must be closely matched in phase and gain response so that they will add only a little extra background noise to the original signal. This

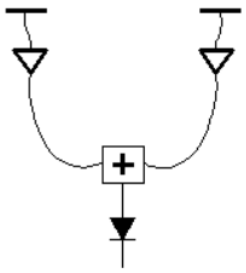

Figure 1.10: Phased array of dipoles. It brings the signals together by making the lengths of the cables equal (Image taken from Emerson (2002)).

makes the phased array simpler mechanically, but more complicated electronically (Emerson, 2002).

In aperture synthesis, instead of all the signals being added together in phase and then detected as in the phased array, pairs of signals are brought to the same location and multiplied together (As shown in Fig. 1.11). With N individual dipoles, there will be $N(N-1)/2$ multiplications. The output of each multiplier is then averaged before being recorded in a computer. Each multiplication gives one Fourier term of a description of the sky distribution within the field of view of each antenna element. The computer combines the products with different permutations of phase offset added to the products. This means that the electronic phase shift that was achieved using the variable cable lengths earlier has been replaced by software. The main advantage here is that in software we can steer the beam over the sky, possibly to several million discrete points and hence it is the ultimate multi-beam system (Emerson, 2002). As multiplying plus averaging is correlation, multiplying interferometers are also called correlation interferometers, and they are nearly immune to receiver gain and noise changes. The aperture synthesis technique is very powerful but it has a drawback.

If we look at this in terms of the relative spatial frequency responses, where spatial frequency is just the reciprocal of particular scale sizes, for a given wavelength the spatial frequency is proportional to the antenna baseline. At zero spatial frequency, it is sensitive to the sum of all the powers of all the sources within its field of

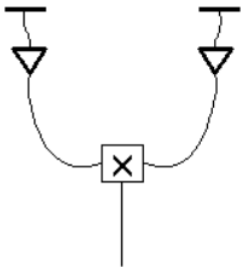

Figure 1.11: Multiplying interferometer. Instead of all the signals being added together in phase and then detected as in phased array, all pairs of signals are brought together to the same location and are multiplied (Image taken from Emerson (2002)).

view. With increasing spatial frequencies, the sensitivity is progressively worse. Beyond its spatial frequency cutoff, a single dish will not be able to distinguish between a series of closely spaced ridges on the sky and a continuous, smooth distribution, albeit it would be able to detect the total flux coming from that part of the sky. The interferometer, on the other hand, has full sensitivity to ridges on the sky that are resonant with its particular spacing in wavelengths, but has no sensitivity to the very large scale structure (Emerson, 2002).

1.3.2 Practical considerations

There are also many technical and practical considerations as follows:

- Instrumentation: The instrumentation of single-dish is simpler than that of an interferometric array. In single-dish, there is only one set of receivers to cover the desired range of wavelengths, whereas with an aperture synthesis array of N telescopes, there have to be N sets of receivers and a cross-correlator able to correlated $N(N-1)/2$ individual baselines. Also, specialised instrumentation may only be available on a single dish rather than each of the antennas in an interferometer because of the cost of the equipment.

- Flexibility: Single-dish instruments do sometimes become elements of interferometric arrays. eg: VLBI. While most large single-dish instruments have

at some time been used for interferometry, very few arrays have been used for single-dish observing. The front-end and the back-end are easier to manage and upgrade as the technology advances with a single-dish telescope, but because of the sheer complexity of an array an interferometer just cannot compete with a single-dish. Hence, general flexibility is a very big plus for single-dish instruments.

- Sensitivity: The larger the collecting area of an antenna, the greater the sensitivity. For some experiments, angular resolution is not an issue and only point-source sensitivity may be all that counts (e.g. pulsars). In such cases the only thing that matters is the effective collecting area of the instrument, be it made up of individual dishes or only a single large dish. In addition, this will be true of an array of smaller antennas. While the total collecting area of an array may be larger, their sensitivity is dependent on the signal collected by each dish.

- Ease of use: Data obtained from a single-dish does not need correlation. Also, there is no need to plan for and coordinate multiple antennas.

From the above discussion we can see that single-dishes are very good at looking at large features and measuring the total amount of energy being received from a given patch of the sky. Correlation interferometers are very good at looking at fine scale structure but are totally blind, for example, to the 3 K background. However, because a single dish does not have the correlation advantage of interferometers, it is very susceptible to changes in the receiver gain and to changes in the receiver noise temperature, which introduces offset to the data. Removing variable baseline offsets can also filter out large-scale structure from the data, which counters one of the main advantages of using a single dish compared to a synthesis array. So in practice, the choice between arrays and single dishes is not a question of absolutes but of making a quantitative comparison of the way the two methods will work in a given situation.

For C-BASS, there was no real prospect of using an array; the hardware cost is dominated by the receiver and it is N times more expensive to put a set of receivers on an array. Also, since C-BASS aims to produce all-sky maps of both the total intensity and polarized synchrotron radiation, we are interested in total flux from extended regions of the sky and hence a single-dish is perfect for the job. To deal with the offset introduced to the data by changes in the receiver gain and the changes in the receiver noise temperature, I have developed my own de-striping software which will be explained in Section 3.3.

1.4 Importance of polarization calibration

Radio sources are often polarized, so even this basic measurement requires a fundamental understanding of polarization. Polarization measurements provide information about the emission region and the emission process e.g:

- Synchrotron radiation from many radio sources, from supernova remnants (e.g. Crab Nebula), normal galaxies e.g. Milky Way, active galactic nuclei – is weakly (typically $< 10\%$) plane polarised.
- Pulsar radiation – coherently emitted and highly polarised.
- CMBR – is very weakly ($<<1\%$) linearly polarised as a result of scattering processes in the early Universe (see Section 2.1.2).

Polarization also provides information about the physical conditions along the propagation path to us:

- Faraday rotation in magnetized plasma rotates the plane of polarization as a function of wavelength λ. It is often the only way to get a direct handle on intervening magnetic fields (see Section 2.1.1).
- Scattering and reflection - polarisation can be induced in unpolarised emission by scattering (as in blue sky) and after reflection.

However, the degree of polarization in astronomical sources is typically small and hence careful calibration is necessary before the results can be interpreted.

1.4.1 Basics of polarimetry

The polarization, along with intensity, wavelength and coherence, is a fundamental property of light. The study of polarized light has led to a deeper understanding of light itself. Christian Huygens was the first to suggest that light was not a scalar quantity and this vectorial nature of light is called polarization (Born & Wolf, 1965). Light is said to be consisting of only transverse components, and if we consider the direction of propagation of light along the z direction, then the transverse components are represented by (Kraus, 1986):

$$E_x(z,t) = E_{0x}\cos(\omega t - kz + \delta_x) \ , \tag{1.18}$$

$$E_y(z,t) = E_{0y}\cos(\omega t - kz + \delta_y) \ . \tag{1.19}$$

The subscripts x and y refer to the components in the x and y directions, E_{0x} and E_{0y} are the maximum amplitudes and δ_x and δ_y are the phases. As the field propagates, $E_x(z,t)$ and $E_y(z,t)$ will give rise to a resultant vector that describes a locus of points in space, and the curve generated by those points gives rise to:

$$\frac{E_x^2}{E_{0x}^2} + \frac{E_y^2}{E_{0y}^2} - 2\frac{E_x}{E_{0x}}\frac{E_y}{E_{0y}}\cos\delta = \sin^2\delta \ , \tag{1.20}$$

where $\delta = \delta_y - \delta_x$.

Eq. 1.20 is recognised as the equation of an ellipse, and shows that at any instant of time the locus of points is described by the optical field as it propagates, is an ellipse, called the polarization ellipse. The presence of the cross-term in equation tells us that the polarization ellipse is rotated through an angle ψ as shown in Fig. 1.12.

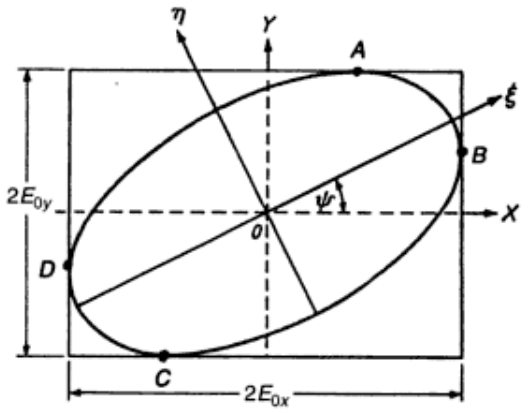

Figure 1.12: An elliptically polarized wave and the polarization ellipse (Image taken from Kraus (1986)).

Typically, completely polarised light is elliptically polarised. But there are certain degenerate forms of the polarization ellipse that are continually encountered in the study of polarized light. The polarization ellipse (Eq. 1.20) degenerates to special forms for different values of E_{0x}, E_{0y} and δ. Without going into the mathematical details (which can be found in Kraus (1986)) I will summarise these results by saying that the degenerate states of the polarization ellipse are (1) linearly horizontal or vertically polarized light (2) linear $+45^\circ$ or -45° polarized light and (3) right or left circularly polarized light.

The polarization ellipse, however, can only describe completely polarized light. It cannot describe unpolarized light or partially polarized light. This is a serious limitation because the emission from celestial radio sources extends over a wide frequency range and within any finite bandwidth, consists of the superposition of a large number of incoherent waves of different polarizations. Typically, the wave is partially polarized i.e., it may be considered to be made up of completely polarized and completely unpolarized parts. This requires us to represent the polarized light in terms of observables.

Since for incoherent (independent) waves the powers add arithmetically, Sir George Stokes (Stokes, 1851) developed a decomposition for partially polarised light in terms of linear combinations of the average powers measured in orthogonal directions. He discovered that the polarization behaviour could be represented in terms

of observables and that any state of polarized light could be completely described by four measurable quantities known as the Stokes polarization parameters. The first parameter describes the total intensity whereas the rest of the parameters describe the polarization state. For a pair of plane waves, which are orthogonal to each other at a point in space at $z = 0$ and represented by Eq. 1.18 and Eq. 1.19, the Stokes polarization parameters are given by:

$$S_0 = I = E_{0x}^2 + E_{oy}^2 \ , \tag{1.21}$$

$$S_1 = Q = E_{0x}^2 - E_{oy}^2 \ , \tag{1.22}$$

$$S_2 = U = 2E_{0x}E_{0y}\cos\delta \ , \tag{1.23}$$

$$S_3 = V = 2E_{0x}E_{0y}\sin\delta \ . \tag{1.24}$$

The above four equations are the Stokes polarization parameters for a plane wave. The first Stokes parameter S_0 is for the total intensity of the light, S_1 describes the amount of linear horizontal or vertical polarization, S_2 describes the amount of linear $+45^\circ$ or -45° polarization and the parameter S_3 describes the amount of right or left circular polarization.

In general, for any state of polarized light, the Stokes parameters always satisfy the relation:

$$S_0^2 \geq S_1^2 + S_2^2 + S_3^2 \ . \tag{1.25}$$

The equality sign is for when we have completely polarized light and inequality when we have partially polarized light or unpolarized light.

The Stokes parameters enable us to describe the degree of polarization Π for any state of polarization. By definition:

$$\Pi = \frac{I_{pol}}{I_{tot}} = \frac{(S_1^2 + S_2^2 + S_3^2)^{1/2}}{S_0} \ , \tag{1.26}$$

where I_{pol} is the intensity of the sum of the polarization components and I_{tot} is the total intensity of the beam. The value of $\Pi = 1$ corresponds to completely polarized light, $\Pi = 0$ corresponds to unpolarized light and $0 < \Pi < 1$ corresponds to partially polarized light.

The position angle is given by:

$$\chi = \frac{1}{2} \tan^{-1} \left(\frac{S_2}{S_1} \right) \ . \tag{1.27}$$

To obtain the Stokes parameters of an optical beam, we must always take a time average of the polarization ellipse. However, the time averaging process can be bypassed if we represent the real optical amplitudes of 1.18 and 1.19 in terms of complex amplitudes:

$$E_x(t) = E_{0x} e^{[i(\omega t + \delta_x)]} = \varepsilon_{0x} e^{(i\omega t)} \ , \tag{1.28}$$

$$E_y(t) = E_{0y} e^{[i(\omega t + \delta_y)]} = \varepsilon_{0y} e^{(i\omega t)} \ . \tag{1.29}$$

where, $\varepsilon_{0x} = E_{0x} e^{(i\delta_x)}$ and $\varepsilon_{0y} = E_{0y} e^{(i\delta_y)}$ are complex amplitudes. The Stokes parameters for a plane wave can be now obtained from the formulas:

$$S_0 = I = E_x E_x^* + E_y E_y^* \ , \tag{1.30}$$

$$S_1 = Q = E_x E_x^* - E_y E_y^* \ , \tag{1.31}$$

$$S_2 = U = E_x E_y^* + E_y E_x^* \ , \tag{1.32}$$

$$S_3 = V = i\left(E_x E_y^* - E_y E_x^*\right) \ . \tag{1.33}$$

1.4.2 The need for calibration

The above equations 1.30−1.33 are simple in theory but not so simple in practice, because the radioastronomical receiving system modifies the incoming polarization with instrumental effects, which must be measured and corrected for. Feeds are almost never perfect, so their polarizations are only approximately linear or circular. Also, typically, no feed has two outputs that are perfectly orthogonal.

A linearly polarized astronomical source has Stokes (Q, U) parameters defined with respect to the north celestial pole (NCP). The first device encountered by the incoming radiation is the telescope. These days all major telescopes are alt-az mounted, which means that the feed mechanically rotates with respect to the sky as the dish tracks the source. The angle of rotation is the parallactic angle (Heiles, 2002). As shown in Fig 1.13, the parallactic angle is the angle between a celestial pole, the target, and zenith. In practice, the Stokes parameters as measured with a single telescope will require correction for cross-coupling effects in the telescope and receiver systems and for the parallactic angle P between the telescope axis and the sky co-ordinates.

The Stokes parameters described in equations 1.30−1.33 can be represented as a column vector, called Stokes vector:

$$S_m = \begin{pmatrix} I_m \\ Q_m \\ U_m \\ V_m \end{pmatrix} \ . \tag{1.34}$$

The measured Stokes parameters are related to the Stokes parameters S_0 of the incoming signal by (Burke & Smith, 2002):

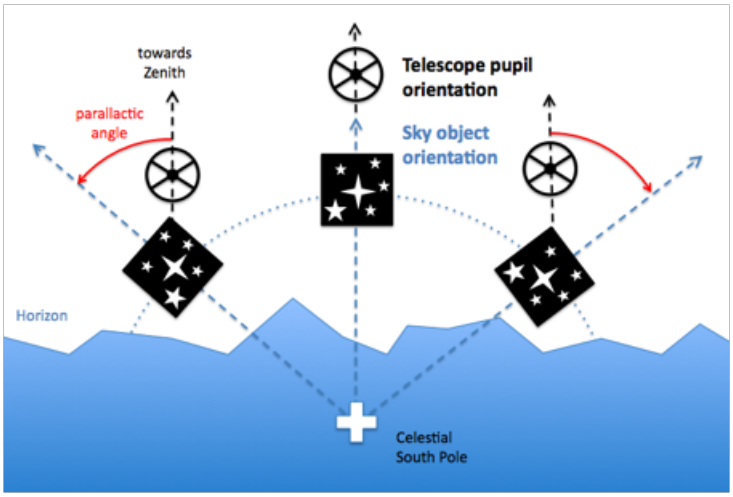

Figure 1.13: The black square with stars is for the sky field that the telescope is tracking across the sky, and the black "crosses" show the orientation of the telescope pupil (Image taken from http://www.mpia.de/homes/thalmann/adi.htm).

$$S_m = M \times S_0 \ , \tag{1.35}$$

where M is the 4×4 Mueller matrix characterizing the total effect of the polarimeter and the parallactic angle. The Mueller matrix essentially describes the modification of the Stokes vector.

The Mueller matrix may be written as the product of two separate matrices, M_p, representing the effects of the parallactic angle, and M_{pol}, representing the polarimeter. M_{pol} may in turn be decomposed into a set of independent matrices representing the polarization characteristics of separate elements in the polarimeter, such as cross-coupling in the telescope feed system, differential phasing in the detector and different gains in the output channel. A further matrix M_{rot} can represent the progress of the signal from the source to the telescope, including Faraday rotation in interstellar space and in the ionosphere. Each element of the combined matrix is an algebraic combination of terms representing the amplitude and phase of the cross-coupling and the differential gains (Burke & Smith, 2002).

The Mueller matrix M_p which accounts for the parallactic angle P is:

$$M_p = \begin{bmatrix} 1 & 0 & 0 & 0 \\ 0 & \cos(2P) & \sin(2P) & 0 \\ 0 & -\sin(2P) & \cos(2P) & 0 \\ 0 & 0 & 0 & 1 \end{bmatrix} . \tag{1.36}$$

The Muller matrix in Eq. 1.35 is then:

$$M = M_{pol} \times M_p . \tag{1.37}$$

The elements of M now contain the variables $\cos(2P)$ and $\sin(2P)$. The calibration of a polarimeter, hence, is achieved by using observations of standard targets such as planets, the Crab Nebula, Orion, etc over a range of parallactic angles over a period of some hours with a telescope.

1.5 Thesis layout

This thesis is concerned with my contribution in the polarization calibration of C-BASS. Chapter 2 describes the C-BASS system. Chapter 3 describes the calibration and data reduction process for C-BASS. Chapter 4 is devoted to the procedure used for generating maps of Stokes parameters for Tau A and Orion. Chapter 5 is for data analysis and finally Chapter 6 is for conclusions and future work.

Chapter 2

C-BASS

The C-band is a portion of the electromagnetic spectrum in the microwave range of frequencies ranging from 4.0 to 8.0 GHz. The C-Band All Sky Survey is a 5 GHz survey of the entire sky in total intensity and linear polarization with a resolution of 0.73°, sensitivity of $\lesssim$ 0.1 mK RMS, and minimal corruption by instrumental errors (King et al., 2010). C-BASS will be the first all-sky survey at 5 GHz playing an important role in the quest for understanding the origin and evolution of our Universe by producing maps of diffuse Galactic emission, where the synchrotron and free-free radiation dominates. This frequency is high enough to be almost unaffected by Faraday rotation and low enough to reach a good sensitivity (i.e., high signal-to-noise ratio). These maps will have an unprecedented sensitivity and accuracy on large angular scales to allow their use primarily in the subtraction of Galactic foregrounds, particularly the polarized synchrotron emission discussed in Section 1.2.2, from the polarized component of the CMB measured by *Planck* and *WMAP* satellites and several other experiments. The maps will also enable new studies of the interstellar medium and magnetic field in the Galaxy and help determine the origin of the poorly-understood anomalous microwave emission.

C-BASS employs very sensitive microwave amplifiers, cooled to within a few degrees of absolute zero, and configured to measure tiny differences in temperature and polarization. They are mounted on two separate telescopes — one at the Owens

Valley Observatory (OVRO) in California, the other at Hartebeesthoek Radio Astronomy Observatory (HartRAO) in South Africa. This allows C-BASS to observe both in the northern and southern hemispheres and hence map the whole sky. The southern telescope is a 7.6-m dish donated to the project by Telkom and the northern telescope is a 6.1-m dish donated by the Jet Propulsion Laboratory. Both telescopes have alt-az mounts. Pictures of the telescopes are as shown in Fig. 2.1.

C-BASS is optimized for measurement of both total intensity I and linear polarization Stokes Q and U. Special attention has been paid to systematic errors and calibration, which have limited the fidelity of previous surveys of both total intensity and polarization e.g. the DRAO 1.4 GHz polarization survey (Wolleben et al., 2006), 1.4 GHz Stockert map (Reich & Reich, 1986), 1.4 GHz Villa Elisa map (Testori et al., 2008), Effelsberg medium latitude survey (Uyaniker et al., 1998) and Sino-German 5 GHz survey (Sun et al., 2007).

In this chapter, Section 2.1 will focus on the science goals for C-BASS survey and Section 2.2 will discuss the survey requirements. Section 2.3 compares the existing surveys with C-BASS and Section 2.4 gives a description of the instrument itself.

2.1 Science goals

2.1.1 Diffuse Galactic Emission

At least four emission mechanisms contribute in the cm-mm range - synchrotron emission, free-free emission, thermal dust emission and anomalous emission (see Section 1.2). A fifth component, known as the microwave haze, also appears to be present near the Galactic centre. Since each component has a different spectral signature, it allows us to separate them from each other and from the CMB. Low frequency data ($\lesssim$ 10 GHz) is dominated by synchrotron (spectral index $\beta \sim -3.0$) and high frequency data ($\gtrsim$ 100 GHz) is dominated by thermal dust emission ($\beta \sim +2.0$) (see Section 1.2.2 and Section 1.2.3). With accurate spectral information we can extrapolate this data to the CMB frequencies ($30 \lesssim \nu \lesssim 150$ GHz). However,

(a) CBASS-N antenna

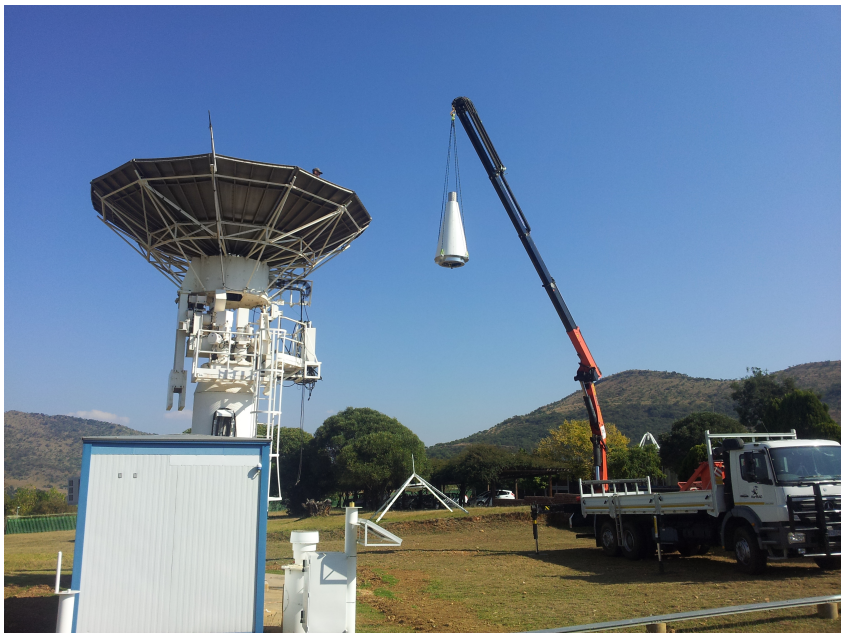

(b) Installing CBASS-S on HartRAO antenna

Figure 2.1: CBASS-N antenna at OVRO in California (top) and CBASS-S antenna at HartRAO in South Africa (bottom) (Pictures taken from http://www.astro.caltech.edu/cbass/pictures.html).

variations in both amplitude and spectral index across the sky, make this difficult without detailed maps of the foregrounds at many frequencies. I have already discussed the emission mechanisms in detail, now I will focus on the role of C-BASS in each of these foregrounds.

Synchrotron Emission

Our knowledge of the intensity of Galactic synchrotron radiation primarily comes from sky surveys at 0.4 GHz, 1.4, 2.3 GHz and 23 GHz (Haslam et al., 1982; Reich & Reich, 1986; Jonas et al., 1998; Gold et al., 2011). As the spectral index of synchrotron emission varies across the sky in the range $-3.3 \lesssim \beta \lesssim -2.4$ (Reich & Reich, 1986; Lawson et al., 1987; Davies et al., 1996; Gold et al., 2009) and the spectrum usually steepens at high frequencies due to energy losses of the cosmic ray electrons, it is difficult to model the synchrotron component accurately.

Synchrotron radiation can be highly polarized (up to $\sim 75\%$) and hence it is expected to be the dominant polarization foreground below ~ 70 GHz (see Section. 1.2.2). The only existing large area polarization surveys below 10 GHz are at 2.3 GHz (Carretti et al., 2009), 1.4 GHz and below and are mostly limited to within a few degrees of the Galactic plane. There is insufficient radio polarization data both in terms of spatial and frequency coverage. Another difficulty is the effect of Faraday rotation at low frequencies. The rotation of the plane of polarization of radiation passing through an ionized medium in a magnetic field is:

$$\triangle PA = \mathrm{RM}.\lambda^2 \ , \tag{2.1}$$

where,

$$\mathrm{RM} \propto \int B.n_e.dl \ , \tag{2.2}$$

is the "rotation measure". n_e is the electron density, B is the magnetic field parallel to the line of sight, dl is the path length and λ is the observing wavelength.

At high latitudes, for many extragalactic sources, the typical RM is ~ 10 rad m^{-2} corresponding to a $\triangle PA \sim 25^\circ$ at 1.4 GHz or $\sim 2^\circ$ at 5 GHz (Wolleben & Reich, 2004). Some regions at high latitude have RMs up to ~ 40 rad m^{-2}, corresponding to $\triangle PA \sim 100^\circ$ at 1.4 GHz and $\sim 8^\circ$ at 5 GHz. Differential FR along the line of sight and within the beam can also cause depolarization, and at 1.4 GHz and 2.3 GHz near the Galactic centre, this is a large effect.

The large area surveys at 1.4 GHz made using the Effelsberg 100-m, DRAO 26-m and Villa Elisa 30-m telescopes detect polarization structures on angular scales of a few degrees or larger (Zainal Abidin et al., 2003; Wolleben et al., 2006; Testori et al., 2008; Reich & Reich, 2009). The typical fractional polarization is ~ 20 % and the RMS polarized intensity is ~ 65 mK. These observations show significant FR and depolarization effects. In high-latitude fields observed with higher resolution, the RMS polarized intensity is ~ 12 mK (Bernardi et al., 2003, 2006; Carretti et al., 2005a, 2006) with only weak FR (Carretti et al., 2005b).

C-BASS at 5 GHz, will be minimally affected by FR and depolarization, an order of magnitude less than the existing 1.4 GHz surveys, and hence will be the first all-sky low frequency survey in which the polarization angles and fractions can be reliably extrapolated to higher frequencies.

Free-Free Emission

As compared to synchrotron and dust emission, free-free has little variation in spectral index; it has a spectral index $\beta = -2.1$ (see Section 1.2.1) with variations $\triangle\beta \sim 0.1$ at CMB frequencies. Free-free can be traced using the optical Hα line but the all-sky maps are limited by absorption of the Hα line by dust and also by Hα reflected from high latitude dust. At high latitudes, free-free emission is generally below synchrotron but it can be dominant in the Galactic plane. In the large HII complexes in the Galactic plane, C-BASS data will be dominated by free-free emission, which will allow verification of the spectral index and constraints on free-free polarization. Although free-free is expected to be inherently unpolarized, it should

not be excluded as a foreground as free-free emission falls off slowly with frequency, so even low levels of free-free polarization may be stronger than the synchrotron emission near the foreground minimum ($\nu \sim 70$ GHz).

Dust

Typical interstellar dust emission at $T \sim 20$ K has a peak at ~ 100 μm (3000 GHz) with $\beta \sim +2$ at lower frequencies (see Section 1.2.3). Thermal dust emission is therefore a dominant foreground at frequencies $\nu \gtrsim 100$ GHz. At 5 GHz, the thermal dust emission will not contribute significantly. Observations at 353 GHz with the Archeops instrument show a mean polarization fraction of 4-5% (A. Benoît et al., 2004; Ponthieu et al., 2005). After extrapolating this to 20 GHz, their estimated contribution to the power spectrum is 0.4 μK RMS. At 5 GHz, the dust polarization will have a negligible contribution.

Anomalous Emission

Theoretical models of anomalous microwave emission (AME) predict a peaked spectrum at range of frequencies (∼10–150 GHz) depending on the properties of the dust grains and their environment (Draine & Lazarian, 1998b; Ali-Haïmoud et al., 2009; Dobler et al., 2009; Ysard & Verstraete, 2010). This spectrum is very different from free-free, synchrotron and thermal dust emission. Spinning dust emission is the best explanation for the AME so far; however, other physical mechanisms like hot free-free emission, hard synchrotron emission or magneto-dipole emission could be contributing at some level (Leitch et al., 1997; Draine & Lazarian, 1999; Bennett et al., 2003b). In order to understand the AME, which may have multiple mechanisms, there is a need of surveys at several frequencies. C-BASS will provide an important diagnostic as it can easily distinguish flat-spectrum synchrotron and spinning dust, precisely because a spinning dust spectrum is not detected at 5 GHz.

The Microwave "Haze"

The fifth component of diffuse emission was discovered over an extended region around the Galactic centre by Finkbeiner (2004) as an excess signal after fitting the other components. Its spectrum is too soft to be free-free and too hard to be synchrotron (i.e., harder than the diffuse interstellar synchrotron). No polarization has been detected, and it is apparently associated with a diffuse gamma-ray component (Dobler et al., 2010; Gold et al., 2011). It is possibly due to flat-spectrum synchrotron from a population of hard electrons, and several theoretical models have been proposed, including the possibility that the electrons are generated by the annihilation of dark matter particles (Cholis et al., 2009; Goodenough & Hooper, 2009; Biermann et al., 2010). Hence, measurements at more frequencies including 5 GHz are required to confirm the nature of the haze.

2.1.2 CMB polarization

The CMB anisotropies have contributed significantly in defining our cosmological model. The angular power spectrum of the fluctuations holds a remarkable wealth of quantitative information about the early Universe, and provides one of the foundations of our current model of the history of the Universe (Spergel et al., 2003; Komatsu et al., 2011). The standard model of cosmology is based upon a spatially flat, expanding Universe whose dynamics are governed by General Relativity and dominated by cold dark matter and a cosmological constant (Λ). *Planck* was able to measure anisotropies on intermediate and small angular scales over the whole sky much more accurately than previous experiments (Planck Collaboration et al., 2013a). The measurement of the cosmological parameters by *Planck* shows that there is an excellent agreement between the *Planck* temperature spectrum at high multipoles ($\ell \gtrsim 40$) and the predictions of the ΛCDM model . All of our current observations can be fit by a six parameter ΛCDM model and *Planck* all-sky temperature maps provides strong constraints on deviations from this model (Planck Collaboration et al., 2013b). *Planck* has not released its polarization data yet, but

several other experiments have already detected the polarization of the CMB and measured its angular power spectrum.

That CMB anisotropies are polarized is a fundamental prediction of the gravitational instability paradigm. Under this paradigm, small fluctuations in the early Universe grow into the large scale structure we see today. If the temperature anisotropies we observe are indeed the result of primordial fluctuations, their presence at last scattering would polarize the CMB anisotropies themselves. The verification of polarization of the CMB on small scales would thus represent a fundamental check on our basic assumptions about the behaviour of fluctuations in the Universe, in much the same way the redshift dependence of the CMB temperature is a test of our assumptions about the background cosmology (Hu & White, 1997). The polarization probes the epoch of last scattering directly as opposed to the temperature fluctuations, which may evolve between last scattering and the present.

CMB polarization at the surface of last scattering is generated by the mechanism of Thomson scattering (Rees, 1968). Consider the distribution of photons scattering off an electron on the LSS. Only a quadrupolar distribution of photons will produce polarized signals (see Fig. 2.2). This is because if the incident radiation is isotropic or a dipole or a higher order multipole than a quadrupole, then the orthogonal polarization directions will cancel. But if the orthogonal directions have different intensities (a quadrupole component), then the scattered radiation will have linear polarization.

The three different scenarios which could be responsible for the quadrupole anisotropy are: scalar perturbations, vector perturbations and tensor perturbations. Scalar perturbations arise due to the density fluctuations in the primordial plasma, vector perturbations result from the vortical motions of the plasma and tensor perturbations are caused by gravitational waves created during inflation (Hu & White, 1997). At the surface of last scattering, the scalar and tensor perturbations dominated (Baumann et al., 2009).

The polarization power spectrum, in addition to containing the information

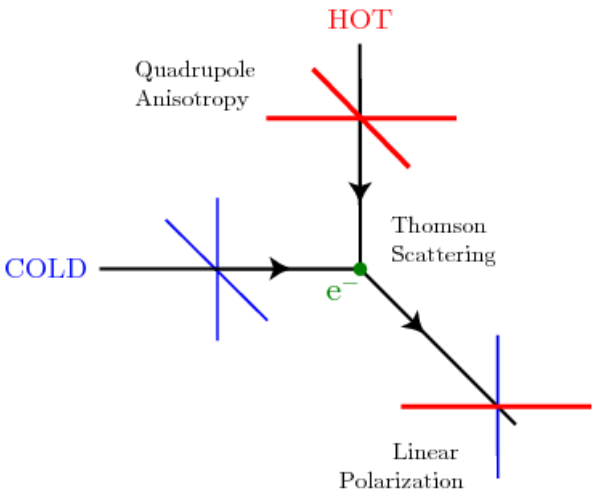

Figure 2.2: Thomson scattering of radiation where quadrupole anisotropy generates linear polarization (Image from http://inspirehep.net/record/872740/plots).

about the conditions at last scattering, also has the potential to provide new information about the epoch of inflation. This is because the gravitational waves created during inflation can induce polarization in the CMB as discussed above, and this component can be separated observationally from the polarization induced by density fluctuation. The amplitude of gravitational waves depends on the energy scale of inflation, which could be the Grand Unified Theory scale, about 10^{16} GeV. Hence, gravitational waves would confirm the prediction of inflation as well as provide information about physical processes at such high energies which are inaccessible on Earth.

The linear polarization of the CMB is described by the Stokes parameters Q and U . But since Q and U are orientation dependent, they produce a rotationally-variant polarization power spectrum. The decomposition of the CMB (Q, U) polarization into two rotationally invariant quantities, called E (characterised as the curl-free part of the polarization vector) and B (divergence-free part of the polarization vector) is given by Kamionkowski et al. (1997) and Zaldarriaga et al. (1997). The E- and B-modes are as shown in Fig. 2.3.

The scalar perturbations create only E-modes, vector perturbations create mainly B-modes (but they are negligibly small). However, tensor perturbations due to gravitational waves create both E- and B-modes. The power in the large scale B-modes

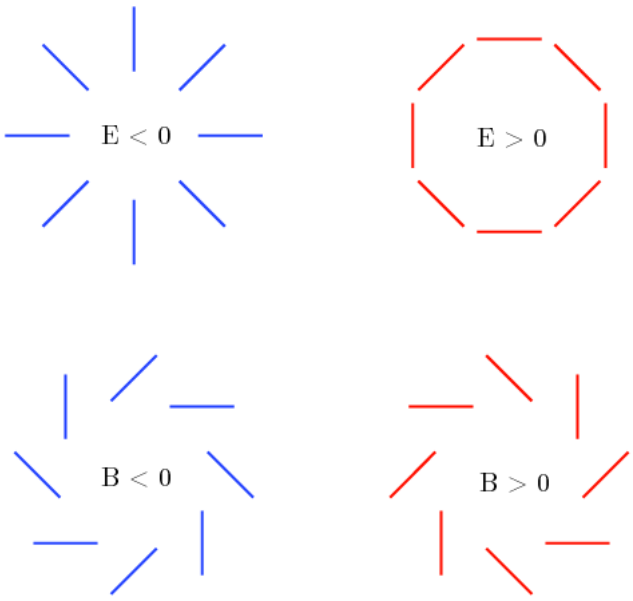

Figure 2.3: Examples of E- and B-mode patterns of polarization (Image from http://inspirehep.net/record/872740/plots).

is a measure of the energy scale of inflaton, and is parameterized by the tensor-to-scalar ratio r. Hence, the CMB B-mode is a direct tracer of gravitational waves from the inflationary period of the Universe (Kamionkowski et al., 1997).

Various experiments like CBI (Sievers et al., 2007), DASI (Leitch et al., 2005), CAPMAP (Bischoff et al., 2008), BOOMERanG (Montroy et al., 2006; Piacentini et al., 2006), QUaD (Brown et al., 2009), BICEP (Chiang et al., 2010), MAXIPOL (Wu et al., 2007), QUIET (QUIET Collaboration et al., 2011), and *WMAP* (Larson et al., 2011) have made measurements of the E-mode and TE cross spectra, but the sensitivity of the experiments is not sufficient to detect the B-mode. A number of experiments have been proposed that should have the sensitivity to detect the B-mode if it is present at the levels predicted in the simplest models of inflation. The current upper limit on B-modes is comparable to the expected foreground contamination (see Fig. 2.4). To reach the goal of removing foregrounds with a precision of better than 10% (see Fig. 2.4) will require reliable foreground polarization maps at a wide range of frequencies. The existing low-frequency surveys cannot be used due to Faraday rotation effects and hence C-BASS will play a crucial role in this.

Practical experiments to search for B polarization face several difficulties. These

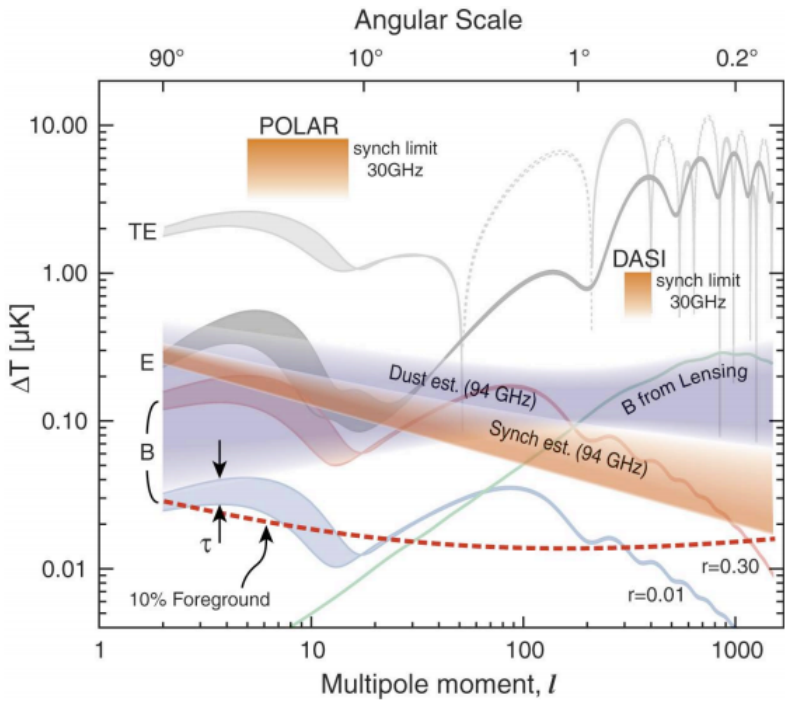

Figure 2.4: Current estimates of polarized Galactic foreground signals at 94 GHz, compared with the CMB polarisation power spectra predicted in the standard cosmological model. Image from (Bock et al., 2006).

include instrumental systematic errors, which can contaminate the polarized signal via "leakage" of the total intensity signal, and can also mix E- and B-modes; the problem of separating B from E which cannot be done completely in an incomplete sky survey; and, most importantly, contamination by foreground emission. The ultimate sensitivity limit that can be achieved with CMB data will be constrained by our knowledge of the foregrounds (Gold et al., 2009; Fraisse et al., 2009). Although the CMB B-mode is much weaker than the E-mode, foregrounds are expected to contribute roughly equally to both modes, so extracting the CMB B-mode in the presence of foregrounds is especially difficult (Fig. 2.4).

2.2 Survey requirements

The primary aim of C-BASS is to allow the accurate removal of polarized foregrounds from B-mode experiments operating in the CMB band (30-150 GHz), this determines the following survey parameters:

2.2.1 Frequency

The goal is to map the Galactic synchrotron radiation at a frequency low enough to minimize contamination by other emission mechanisms but high enough to minimize the effects of Faraday rotation. This suggests a frequency in the range 5−10 GHz. A band centred at 5 GHz is chosen where a full sky survey can be completed in less than a year with a single-feed receiver. As synchrotron emission is $\sim$ 6-7 times fainter at 10 GHz, a full sky survey at 10 GHz would require many years or a more expensive multifeed receiver.

To maximize the sensitivity, a bandwidth of 1 GHz spanning 4.5−5.5 GHz was chosen. A bandwidth larger than 1 GHz runs the risk of contamination from man-made radio sources, and suffers from large colour corrections - spectral index dependent calibration offsets. However, it was found that even at 1 GHz it was already a problem so we had to add radio frequency interference (RFI) filters which reduced the bandwidth to $\sim$ 0.5 GHz.

2.2.2 Resolution

The primordial B-mode spectrum is predicted to be quite smooth, so an important check on this would be the detection of its one feature, the peak at $\ell \sim 90$ or about 2°. To be certain of its detection, measurements up to $\ell \sim 150$ are needed, which fixes the resolution of the survey to about 1°. The full width at half maximum (FWHM) of an antenna beam is calculated using Eq. 1.17. For C-BASS, the resolution of the survey comes out to be 48 arcmin (0.73°), which is well-matched to planned B-mode CMB experiments ($2 < \ell < 300$, angular scales $> 0.5°$).

2.2.3 Sensitivity and survey time

The C-BASS receiver design is a novel hybrid of a pseudo-correlation polarimeter and a pseudo-correlation radiometer. The theoretical RMS noise of the correlation receiver is:

$$\sigma_T = \frac{T_{sys}}{\sqrt{\triangle\nu t}} \tag{2.3}$$

in I,

$$\sigma_T = \frac{T_{sys}}{\sqrt{2\triangle\nu t}} \tag{2.4}$$

in Q and U where T_{sys} is the system temperature, which includes the amplifier noise temperature and the effective sky temperature, $\triangle\nu$ is the receiver bandwidth and t is the integration time.

The usual radiometer equation applies to a single-polarization receiver, say measuring right circular polarization, $I+V$. C-BASS receiver measures both $I+V$ and $I-V$, and when we average them together to get intensity (see Section 3.1) we gain a factor of $\sqrt{2}$ in sensitivity. We lose this again because the cold load is just as noisy as the sky, but has no sky signal, so the theoretical RMS noise in I is as given by Eq. 2.3. A correlation polarimeter looking just at the sky has the property that all four Stokes parameters, I, Q, U, V, have the same RMS. This is $\sqrt{2}$ times better than the classic sensitivity equation for a single polarization: for I and V the reason is as explained above; however, we obtain two measurements each of Stokes Q and U, which can be compared to check for systematic errors (see Section 2.4) and hence there is a factor of $\sqrt{2}$ in the denominator of Eq. 2.4.

In the C-BASS proposal to Particle Physics and Astronomy Research Council (PPARC), it was estimated that the polarized intensity at 5 GHz was > 0.49 mK over 90% of the sky. The target in the proposal was a mean sensitivity of 0.11 mK in each 'pixel' area $\Omega_{\rm pix} = 0.63$ square degrees, calculated by assuming that this is the noise correlation area after smoothing from an instrumental beam of 0.85° to 1° FWHM. We originally expected $T_{sys} = 20$ K and bandwidth $\Delta\nu = 1$ GHz, and using Eq. 2.4, this implies a noise in the time-ordered data of $s = 0.45$ mK Hz$^{-1/2}$, requiring an observing time of 16.5 sec per pixel, or 12.5 days for the summed observing time from telescopes in both hemispheres. We planned to observe for 9

months in each hemisphere, night-times only, and 50% observing efficiency during night-time, so $\eta = 25\%$, which would give a summed observing time of 4.5 months or 137 days. Thus, we expected to exceed our target sensitivity very comfortably.

However, the real system is not as sensitive as planned, because the bandwidth is reduced by the notch filter to $\Delta\nu = 470$ MHz and $T_{sys} \approx 35$ K mainly due to unexpectedly high illumination of the baffles. Measured RMS in the Q or U signals during the best data period (Nov 19 to Dec 31 2012) is around $s = 1.5$ mK Hz$^{-1/2}$. During this period we achieved a survey efficiency of $\eta = 0.21$.

To match C-BASS to the Haslam et al. (1982) map, with resolution 0.85°, we would need a smoothing beam FWHM = 0.435°, giving an averaging area of $\Omega_{\rm pix} = 0.430$ square degrees. To get a 1° beam, we have $\Omega_{\rm pix} = 1.059$ square degrees and to get an RMS of 0.11 mK in the maps with $s = 1.5$ mK Hz$^{-1/2}$, we need to average for $\tau = 186$ s.

To achieve Haslam final resolution, we would need on-source time of 0.566 years over the whole sky, or 0.94 years on each telescope assuming $\eta = 30\%$. To achieve 1° we need 0.382 year (140 days) per telescope. Alternatively, suppose we observe for 6 months in each hemisphere, again at $\eta = 30\%$ then we can afford to divide up the sky into 2×6 months×0.3/186 s =50900 patches, i.e. each of area 0.810°. This corresponds to a smoothing FWHM of 0.598°, giving an effective survey resolution of 0.944°.

2.3 Existing surveys

The early small-area, high-latitude, experiments which measured the EE power spectrum of the CMB focused on low foreground emission areas of the sky where foreground subtraction was not necessary. However, as seen in Section 2.1.2, a robust detection of the much-fainter B-mode power spectrum is likely to require data from large areas of the sky and hence some form of foreground removal, particularly if the tensor-to-scalar ratio r is small (≤ 0.1).

The dominant source of polarized emission at CMB frequencies accessible from the ground is Galactic synchrotron emission. The polarized Galactic synchrotron emission is currently poorly characterized; the current status of moderate-resolution, large sky area surveys in the range 100 MHz to 100 GHz is listed in Table 2.1.

Large-area surveys				
f (GHz)	**Resolution**	**Sky Coverage**	**Reference**	**Type**
0.408	0.85°	All Sky	Haslam et al. (1982)	T
1.410	0.6°	$\delta > -29°$	Wolleben et al. (2006)	P
1.420	0.58°	$\delta > -19°$	Reich (1982)	T
1.420	0.59°	$\delta < -10°$	(Reich et al., 2001)	T, P
2.326	0.33°	$-83° < \delta < 13°$	Jonas et al. (1998)	T
2.3	0.15°	$-87° < \delta < 0°$	Carretti et al. (2009)	P
23, 33, 41, 61, 94	0.82° to 0.21°	All Sky	Bennett et al. (2003a)	T, P

Table 2.1: Existing large-area surveys in the range 0.1 GHz to 100 GHz.

The *WMAP* 23 GHz polarization map has a low signal-to-noise ratio over much of the sky, while the 1.4 GHz polarization surveys are expected to be badly affected by Faraday rotation at low Galactic latitudes and hence they are not useful in extrapolating polarized synchrotron emission to higher frequencies. Fig. 2.5 shows the *WMAP* 9 year map of polarized intensity at 23 GHz (K-Band). C-BASS will make a high signal-to-noise ratio version of this map at a frequency of 5 GHz and aims to plug the gap between the 1.42 GHz survey and the *WMAP* 23 GHz survey.

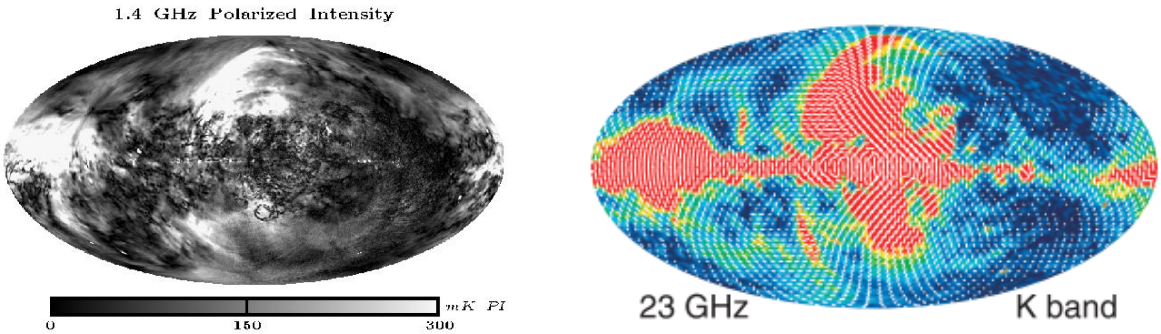

Figure 2.5: Left: Polarized intensity at 1.4 GHz from Reich & Reich (2009). Right: *WMAP* 9-year map of polarized intensity at 23 GHz from Bennett et al. (2012).

2.4 Receiver design

The C-BASS receiver is a novel hybrid of a continuous comparison (or pseudo-correlation) radiometer and a pseudo-correlation polarimeter covering the 4.5 to 5.5 GHz band. A schematic diagram of the receiver is shown in Fig. 2.6. Systematic errors in total intensity, Stokes I, are minimized with a comparison radiometer with balanced loads and errors in linear polarization, Stokes Q and U, are minimized with a correlation polarimeter. The correlation polarimeter is implemented in analog electronics in the northern receiver, but in digital electronics in the southern receiver. An orthomode transducer (OMT) extracts the orthogonal linear polarizations from the sky signal. This is followed by a 90° hybrid to form orthogonal left and right circular polarization. The OMT and first-stage amplifiers are cooled to $\sim$ 10 K in the cryostat.

A weak noise signal is injected into each circular polarization for calibration purposes. The circular polarization signals are then combined with independent reference signals using 180° hybrids. The temperature of the reference loads is controlled by a Cryocon 32B controller to match them to the average sky temperature of about 6 K. A mismatch between sky and load temperature increases the effects of $1/f$ noise, but these are reduced using an r factor as in the *Planck* low frequency instrument (LFI) (Seiffert et al., 2002). The r factor is a gain modulation factor that brings the difference between sky and load temperature as close as possible to zero simultaneously minimizing $1/f$ noise (Mennella et al., 2003). The four signals thus formed are then amplified and filtered.

After filtering and amplification, each signal is split in two. In one arm of the split, the signals are passed through a second stage of 180° hybrids, where the reference signals are discarded. The recovered circular polarizations are then phase switched and split four ways each. They are then correlated in all possible combinations using both 180° and 90° hybrids to obtain two measurements each of Stokes Q and U, which can be compared to check for systematic errors. (When the left-circular and right-circular polarization voltages are correlated using a 180° hybrid we

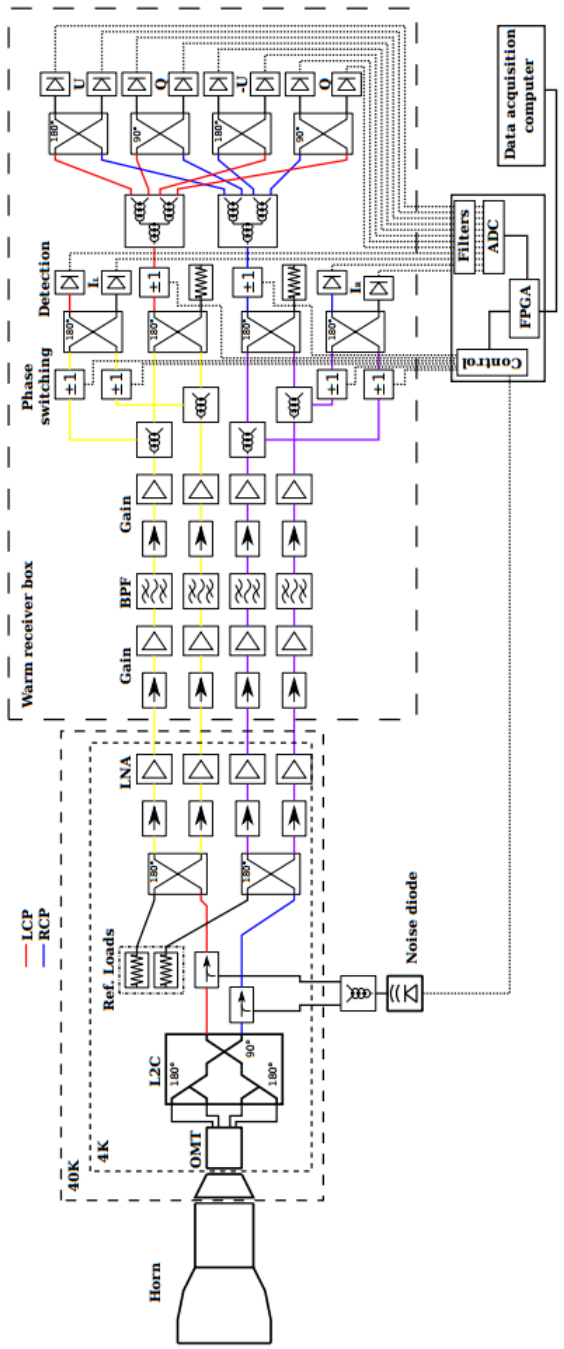

Figure 2.6: Schematic representation of the northern C-BASS receiver. The horn is followed by an OMT plus Linear-To-Circular converter (L2C) which produces orthogonal circular polarizations. A calibration noise signal is injected equally into the circular polarizations. These are then combined with reference load signals using 180° hybrids, followed by low noise amplifiers (LNAs). These signals exit the cryostat and are further amplified and filtered by band-defining filters. Further separation and combination of radio frequency (RF) signals is performed before the RF signals are detected using detector diodes. The detector diode voltages are digitized and further processed by a field programmable gate array (FPGA) (King et al., 2010).

obtain Stokes U. When they are correlated with a 90° hybrid we obtain Stokes Q). In the second arm of the split, the combinations of left and right circular polarization and the reference signals are separately phase switched and pseudo-correlated. Phase switching removes any systematic offset in the detection and readout system, and any leakage from one section of the receiver to another, if the phase switches are driven with orthogonal square wave signals. The outputs of the pseudo-correlating hybrids are connected to detector diodes. These detector diodes produce output voltages proportional to the power of their input signals. The detector output voltages are sent to the digital readout system which performs further signal processing. The final data is read from the digital readout system by a data acquisition computer and then stored to disk. We also calculate and get two measurements of Stokes I. However, we do not know the load temperature accurately enough so what we really get is $I-$offset, where offset is fairly constant but not known.

The cryostat is supported above the dish surface on three legs. The cryostat supports the warm horn, which in turn supports the secondary mirror on a foam cone, so both cryostat and horn are structural elements. The warm part of the receiver is mounted under the cryostat at the dish vertex (see Fig. 2.7).

The system temperature has been measured on the telescope using hot and cold loads and is < 30 K, of which ~ 4 K is contributed by the amplifiers. The contribution of the foam support cone and absorbing tunnels is $\sim 1-3$ K.

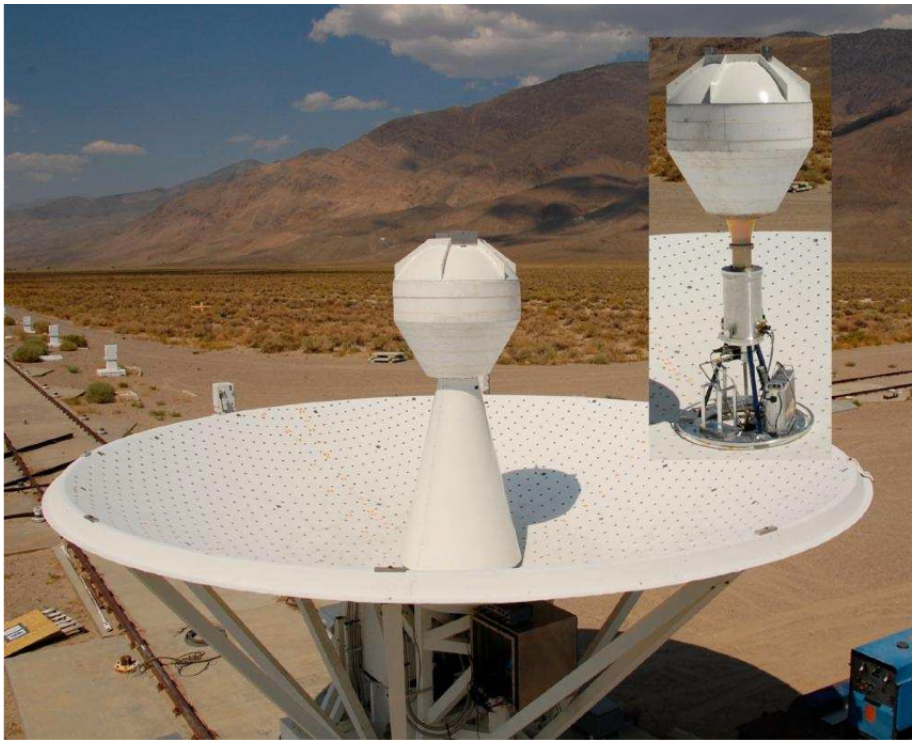

Figure 2.7: Photograph of the C-BASS dish at OVRO, showing the foam cone secondary support. The inset shows the interior of the metal shroud, which houses the cryostat and warm receiver (King et al., 2010).

Chapter 3

Calibration and data reduction

Every telescope is unique. However, this uniqueness makes it difficult to directly compare measurements from one telescope with another. In addition, even measurements taken on a given telescope, at a given frequency, can change over time. These changes may be because of changes in the telescope system temperature, the telescope response or the atmospheric conditions. Because of this, we may record different measurements of the same object with the same telescope over time. Therefore, there is a need to ascertain if the source emission is truly varying with time or if the difference is because of the changes within the telescope. Hence, in order to compare measurements between two telescopes or even between one telescope taken at different times, we need a universal measurement system. This is called the process of data or telescope calibration (O'Neil, 2002).

The C-BASS data reduction package consists of a complete pipeline for flagging, calibrating, and reducing the time-stream data. In the pipeline, the data are converted to physical units, corrected for instrumental gain variations and for the cyclic temperature variations of the cold load; and the polarization angles are aligned to astronomical calibrators (primarily Tau A, the Crab Nebula). Anomalous data are flagged at each step, and the data are filtered to remove corrupting signals which are not at the scan rate. The data are also flagged for RFI. Currently, the C-BASS data is affected by microphonic oscillations at 1.2 Hz due to the pump cycle of the

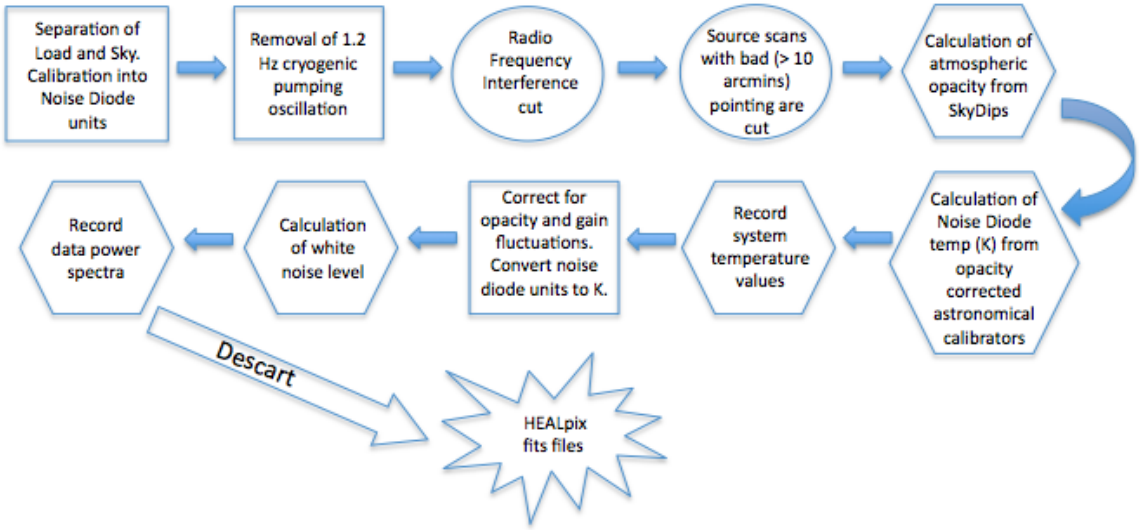

Figure 3.1: Block diagram of C-BASS pipeline.

cryostat. The power coming out of the cold receiver fluctuates at 1.2 Hz. Initially it was thought that this was due to temperature fluctuations of the cold load; so this was isolated from the cold plate to stop the fluctuations. However, that did not fix the issue. So now the 1.2 Hz signal is subtracted using a template-fitting approach, in which templates are calculated in phase with direct cold cycle monitoring on the cold plate. This process is incorporated in the pipeline. The output of the pipeline is calibrated time-stream data, which is saved as Flexible Image Transport System (FITS) files and used to generate maps of the sky. The time-ordered data is assembled into all-sky maps by the DE-Striping CARTographer (DESCART) map-making algorithm, which approximates the maximum-likelihood approach to map-making (Sutton et al., 2009, 2010). It uses prior information of the power spectrum of the instrument noise, obtained from the data, to produce destriped maps of I, Q, and U which are negligibly different from the optimal. This method does not filter the signal or bias the E- or B-mode power spectra of the polarization map. The map-making algorithm identifies and removes both the scan-synchronous offsets and the constant offsets in each channel, and corrects for the telescope polarization axis orientation. Fig. 3.1 shows the complete block diagram of the pipeline.

For my project, I used the 'reduceData' module (developed in MATLAB) from

the existing pipeline which is used for flagging, calibrating and reducing the time-stream data. I then developed my own de-striping software in IDL (Interactive Data Language), instead of using DESCART, in order to remove the baseline from the data. After baseline removal, I used a binning code written by Dr. Patrick Leahy to make maps of Stokes I, Q, U and V. This code can be found in Appendix A.

A brief description of the reduceData module is given in Section 3.1. Section 3.2 deals with the description of the data sets and Section 3.3 will introduce the reader to the method I used for baseline removal of the data.

3.1 Data reduction

The reduceData module is comprised of a number of routines that perform the task of calibration and data reduction. This module reads a customizable script called 'redScript.red' in which all the routines are listed. If the user, for instance, does not want to convert the data from noise diode units to Kelvin, he/she can manually edit the script and remove the routine which performs this task. The reduceData module will then output the data in terms of noise diode units only. A brief description of each routine from redScript.red script is as follows:

1. alpha: The raw data is comprised of 6 channels:

   ch1 = $\left(\frac{I+V}{2} - \text{load}\right)$, ch6 = $\left(\frac{I-V}{2} - \text{load}\right)$, ch2 = $Q1$, ch3 = $U1$, ch4 = $Q2$, and ch5 = $U2$. The alpha routine splits the raw data such that we get 8 channels - ch1–ch8 after separation.

   Channel 1 and channel 8 after alpha are:

   ch1 = $\left(\frac{I+V}{2} - \text{load}\right)$ and ch8 = $\left(\frac{I-V}{2} - \text{load}\right)$. These are averaged later in the pipeline (in module 'getIV') to get intensity.

   Channels 2 to 7 after alpha are:

   ch2 = $Q1$, ch3 = $U1$, ch4 = $Q2$, ch5 = $U2$, ch6 = $Q3$, ch7 = $U3$ where $Q3$, $U3$ are the average Q and average U (Two measurements each of Stokes Q

and U are obtained, which can be compared to check for systematic errors as previously discussed in Section 2.4). This routine also corrects for the leakage between Q and U polarization, makes a note of the system temperature T_{sys}, and puts everything in noise diode units. Putting in noise diode units essentially means that the data is scaled so the amplitude of a noise diode event is 1 unit in polarization and 0.5 unit in intensity. To calibrate noise diode units, standard calibrators like Tau A, CygA and M42 are observed.

2. load: Measures and corrects for 1.2 Hz oscillations in the data. It fits for the phase and amplitude then removes it.

3. stokes: This applies the r-factor (see Section 2.4) to the total intensity data streams, and creates a matrix of Stokes parameters. We have a balanced receiver so it is simply getting multiplied by $r = 1$.

4. rfi: Identifies the RFI in data and flags it.

5. pointing: Corrects the nominal to actual pointing. If a telescope's pointing is accurate, the maxima of the scans will lie in the centre of each cross scan. If the pointing is in error, an offset between the centre of the cross scans and the peak intensity measured by the observation will be seen. This routine makes a note of the source we are looking at, calculates the encoder offset and flags the data.

6. noise: Calculates the temperature of the noise diode. It looks for standard calibrators like CygA, CassA, and Tau A and puts the noise diode temperature in K - this essentially means that it fits their amplitudes using a 2-D Gaussian fitting and finds the conversion factor from noise diode units to K. It also writes the temperature out to a file.

7. tau: This routine is for opacity calculation. It calculates the atmospheric opacity using sky dips and writes it out to a file. Later this file is read to correct for opacity.

8. tsys: Makes a note of the system temperature, multiplies the T_{sys} in noise diode units into the factor needed to get it in K.

9. astro: Converts the data to K, multiplying it by noise diode units, and also corrects for the opacity using:

$$T_A^{'} = T_A e^{\tau/\sin(el)} \ , \tag{3.1}$$

where $T_A^{'}$ is the antenna temperature, τ is zenith opacity and el is the elevation.

10. rms : Calculates the RMS noise (white noise level) from the survey and makes a note of it. It bins the data in steps of 1 sec, 10 sec, 100 sec and 1000 sec to produce plots of RMS noise vs integration time.

11. power: Makes the power spectra of the data.

12. overf: Calculates the $1/f$ noise. To do this, it takes the power spectra of the data and fits it to see where the f_{knee} (knee frequency) is to make sure it is as low as possible. Knee frequency is where the RMS receiver output due to thermal noise fluctuations and gain fluctuations is equal.

13. fits: Takes the data and arranges it in a FITS file.

3.2 Selection of the data sets

The C-BASS collaboration maintains a log of observations done on each day by the telescope called 'obs_logs'. The log contains the date of observation, the start and end time of the observation, and the schedule (it tells if is a C-BASS survey schedule, a calibrator scan, a raster scan etc). As described in Section 1.4.2, the calibration of a polarimeter is achieved by using observations of standard targets such as planets, the Crab Nebula, Orion etc, over a range of parallactic angles over a period of some hours with a telescope. It was necessary to look at both a polarized source (Tau A) and an unpolarized source (Orion nebula) as a polarization calibrator to achieve

proper calibration of the polarimeter. I selected a number of raster scans for this purpose, which are listed in Table 3.1 and Table 3.2.

Since I started working on the project, the telescope was off from 24th Sept'12 to 18th of Nov'12 so no observations were done. From 19th Nov'12 till 31st Dec'12 the telescope was working and we had good data. On 1st Jan'13 the cold head broke so the receiver was warm and we had no data. From 18th Feb'13 the telescope was back in working condition, however, the data quality was poor because it was affected with 1.2 Hz oscillations. The raster scans I selected are from these different periods when the data were good and when the data were affected with 1.2 Hz. Here, I will give a detailed analysis of raster scans done on 17-Jul-2013 and 28-Apr-2013 for Tau A and Orion nebula respectively, mainly because of the quality of the data, and because the observations were of long duration, a range of parallactic angles was covered. For the rest of the scans I shall only present and compare the results as data analysis method is the same for all of them.

The Crab Nebula (also known as M1, NGC 1952, Taurus A) at coordinates $\alpha = 5^{\mathrm{h}}34^{\mathrm{m}}32^{\mathrm{s}}$ and $\delta = 22°0'52"$ is a supernova remnant and pulsar wind nebula in the constellation of Taurus. It emits a highly polarized signal due to both the synchrotron emission of the central pulsar and its interaction with the surrounding gas (Hester, 2008). The Orion Nebula (also known as Messier 42, M42, or NGC 1976) at coordinates $\alpha = 5^{\mathrm{h}}35^{\mathrm{m}}17^{\mathrm{s}}$ and $\delta = -5°23'28"$, on the other hand, is a diffuse nebula situated south of Orion's Belt in the constellation of Orion and is an unpolarized source. Since Orion is an unpolarized source, ideally the Stokes Q, U and V would be equal to zero. By making maps of Stokes I, Q, U and V we can identify the leakage from Stokes I into Stokes Q, U and V. With an extensive study of Orion, we can recover the parameters needed to correct for this effect with improved precision. We can then verify the effectiveness of the correction process on a strong polarized source such as the Crab Nebula.

Tau A				
Scan No.	Start Time (UTC)	Stop Time (UTC)	Schedule	Hours
1	17-Jul-2013:13:53:34	17-Jul-2013:21:57:50	source_raster_8x4x0.05.sch(8h, taua)	8
2	15-Jul-2013:17:26:28	15-Jul-2013:20:41:57	source_raster_8degM.sch(3h, taua)	3
3	29-Jun-2013:16:57:15	30-Jun-2013:03:07:34	source_raster_8degM.sch(10h, taua)	10
4	25-Mar-2013:22:55:18	26-Mar-2013:06:29:04	source_raster_8x4x0.05.sch(7h:30m, taua)	7.30
5	13-Dec-2012:05:50:12	13-Dec-2012:15:54:05	source_raster_8x4x0.05.sch(10h, taua)	10
6	12-Dec-2012:03:05:38	12-Dec-2012:13:39:01	source_raster_8x4x0.1.sch(10h:30m, taua)	10.30
7	07-Nov-2012:07:22:02	07-Nov-2012:17:30:34	source_raster_8degM.sch(10h, taua)	10

Table 3.1: Tau A raster scans from the observations log.

Orion				
Scan No.	Start Time (UTC)	Stop Time (UTC)	Schedule	Hours
1	16-Jul-2013:13:48:20	16-Jul-2013:21:08:10	source_raster_8x4x0.05.sch(10h, m42)	10
2	11-Jun-2013:17:14:41	12-Jun-2013:00:54:33	source_raster_8degM.sch(7h:30m, m42)	7.30
3	28-Apr-2013:18:16:18	29-Apr-2013:03:41:36	source_raster_8x4x0.05.sch(9h, m42)	9
4	20-Nov-2012:10:10:58	20-Nov-2012:12:26:22	source_scans.sch(2h, m42)	2
5	13-Nov-2012:06:46:02	13-Nov-2012:12:55:49	source_raster_8degM.sch(6h, m42)	6

Table 3.2: Orion nebula raster scans from the observations log.

3.3 Baseline removal

The derived antenna temperature includes sky emission as well as changes in the atmospheric opacity or ground pickup. The system temperature also introduces DC offset to the data. Fitting a low-order polynomial to areas of the data thought to be devoid of emission eliminates most of these unwanted factors (Maddalena, 2002).

Baseline fitting to the on-source records is the simplest and most efficient of the methods for obtaining blank sky information for the observations. The data can be thought of as:

$$\text{data} = \text{source} + \text{noise} + \text{offset} \ . \tag{3.2}$$

When we are off-source, the source term is zero. The idea is to fit a baseline to those regions of an observation which are known to contain no signal from the object of interest. In other words, the aim is to use a cut to get rid of the points where the source is larger than the noise, and then work out the median and/or mean of the remaining points to get an approximate zero level.

Although this procedure is extremely efficient, it has several drawbacks. If the baseline is not reasonably flat for any reason, then this option should not be used because a poor fit can artificially add or subtract considerable emission to the observation of interest. Errors induced from the baseline fitting method come primarily from the quality of fit (O'Neil, 2002).

Therefore, it was important to look at the data of interest first before going ahead with baseline fitting. In order to do this, I first read the observational data from the obs_logs into the pipeline. After this, I reduced the data using the reduceData module described in Section 3.1 with routines alpha, load, stokes, rfi, pointing, noise, tau, tsys, astro, rms, power, overf and fits. The output of the pipeline, the calibrated time-stream data, was saved as a FITS file. The raw data and the reduced data for 17-Jul-2013 Tau A raster is as shown in Fig. 3.2 and Fig. 3.3 respectively. Similarly, the raw data and the reduced data for 28-Apr-2013 Orion raster is as shown in

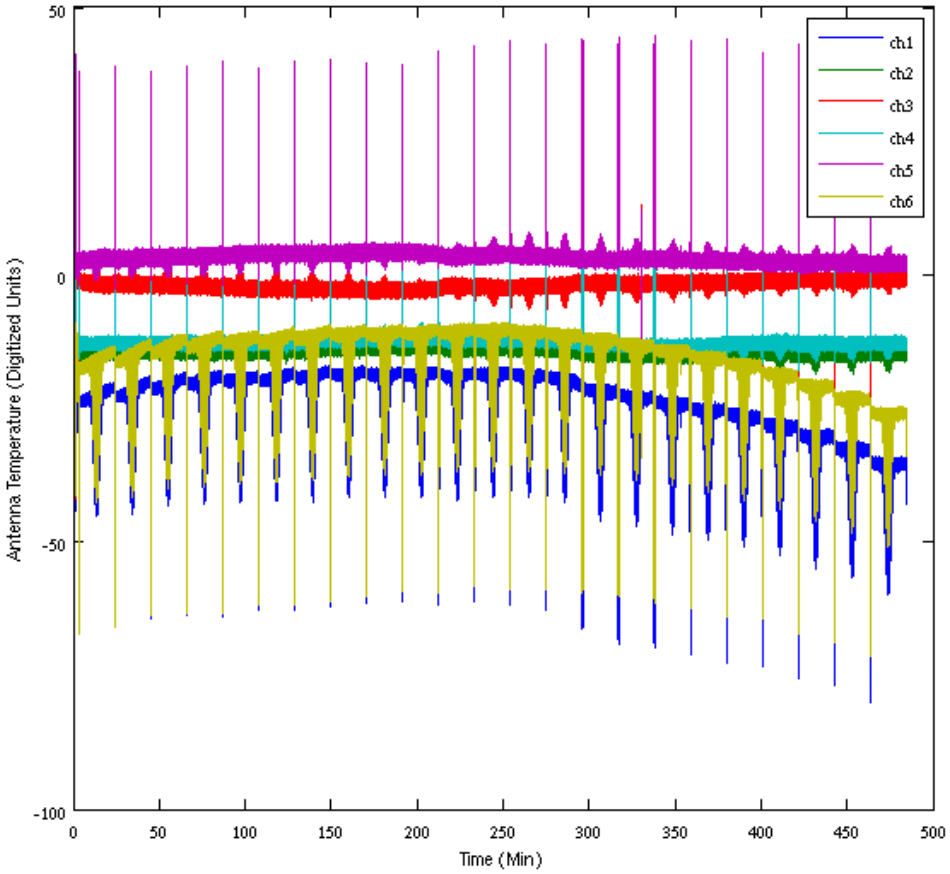

Figure 3.2: Tau A raw data before running through the pipeline. The bumps are where the source is encountered in the raster scan and the vertical bars are the noise diode events. Channels 1 to 6, before data reduction, are also clearly seen in the raw data.

Fig. 3.4 and Fig. 3.5 respectively. In Fig. 3.2 of Tau A raw data for example, the bumps are where the source is encountered in the raster scan and the vertical bars imply noise diode events. Channels 1–6 as described in Section 3.1 are clearly seen in the raw data. After data reduction we get 8 channels, and these are shown in Fig. 3.3. We can see the presence of two intensity channels in the reduced data, and this is because after reduction, ch1 $= \left(\frac{I+V}{2} - \text{load}\right)$ and ch8 $= \left(\frac{I-V}{2} - \text{load}\right)$, as previously discussed in Section 3.1. I looked at the reduced data also to make sure that there are no huge spikes, due to RFI, present in the data after data reduction, and that the reduction process has indeed worked well.

The FITS file produced by reduceData module is a structure of data values like

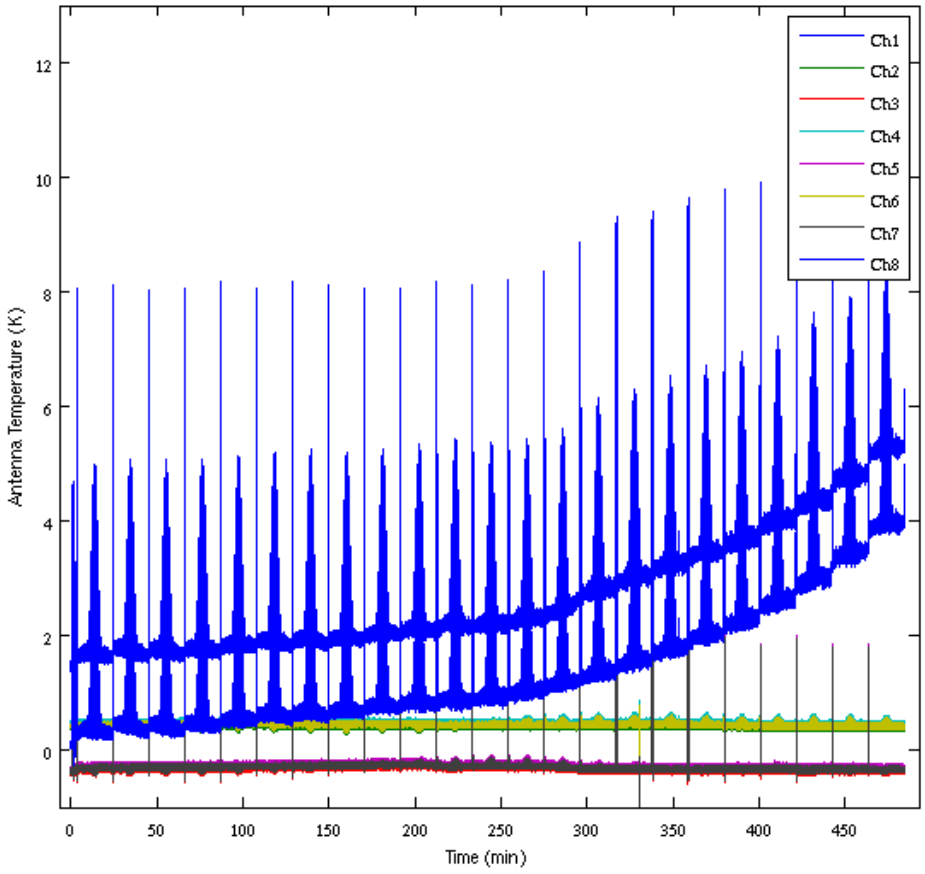

Figure 3.3: Tau A reduced data after running through the pipeline. Channels 1 to 8 after data reduction are clearly seen in the plot. The presence of two intensity channels in the reduced data is because after reduction, ch1 = $\left(\frac{I+V}{2} - \text{load}\right)$ and ch8 = $\left(\frac{I-V}{2} - \text{load}\right)$.

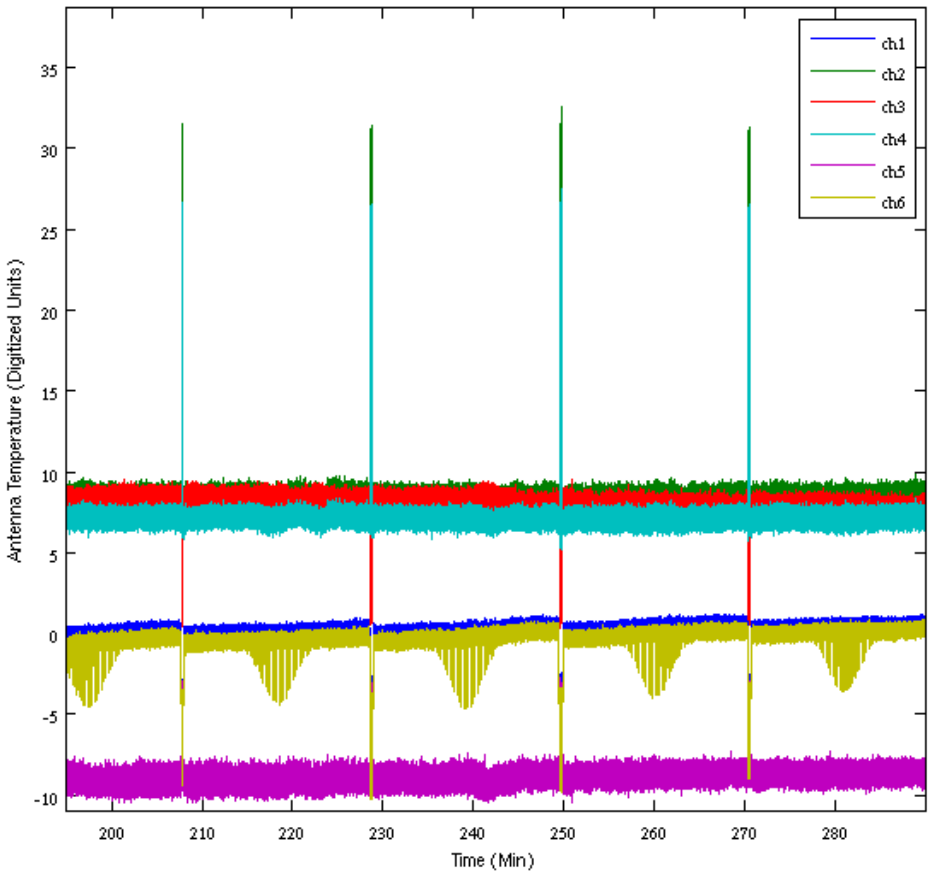

Figure 3.4: Orion raw data before running through the pipeline. The bumps are where the source is encountered in the raster scan and the vertical bars are the noise diode events. Channels 1 to 6, before data reduction, are also clearly seen in the raw data.

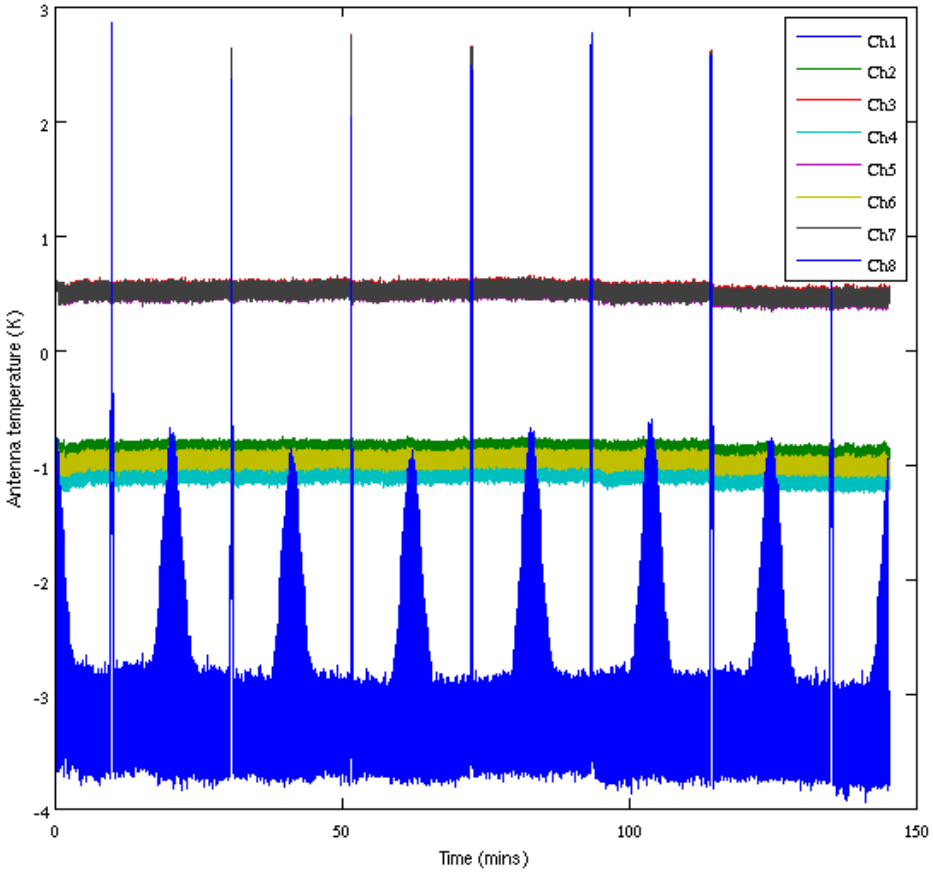

Figure 3.5: Orion reduced data after running through the pipeline. Channels 1 to 8 after data reduction are clearly seen in the plot. The presence of two intensity channels in the reduced data is because after reduction, ch1 = $\left(\frac{I+V}{2} - \text{load}\right)$ and ch8 = $\left(\frac{I-V}{2} - \text{load}\right)$.

time, RA (Right Ascension), Dec (Declination), Lat (Latitude), Lon (Longitude), Stokes I, Stokes U, Stokes Q, Stokes V etc. I read this file in IDL using the standard Healpix/IDL subroutine 'read_fits_s', which reads in any type of FITS file (Image, Binary table or ASCII table) and outputs the data in IDL structures. This helped me generate a plot of intensity vs time for both Tau A and Orion as shown in the Fig. 3.6. The plots show a single scan (on a much shorter time scale) from the series of scans in Fig. 3.3 and Fig. 3.5 for Tau A and Orion respectively. Each raster starts by pointing the telescope directly at the source. Then the telescope moves off to the bottom left-hand corner of the raster pattern, and starts the zig-zag series of rasters. The series of spikes in the plot are the set of zig-zags that make up a raster. The purpose of this exercise was to see if the baseline was flat, and because it looks reasonably flat, I went ahead to develop a program in IDL that would perform the job of baseline removal.

While developing the baseline removal software, the first step was to convert the time scale from modified julian date (MJD), which is of the order 10^4, to seconds starting from zero, as this is an easier number to deal with. I then identified the individual scans that make up the whole raster schedule. For 17-Jul-2003 Tau A, 23 and for 28-Apr-2013 Orion, 18 such scans were found (These scans are also seen in Fig. 3.2−Fig. 3.5). I then worked out the median of each such scan. A polynomial was then fit to the data (which lay below the median) as a function of time using 'POLY_FIT', a standard IDL routine. The POLY_FIT function performs a least-square polynomial fit and returns a vector of coefficients. I first fitted and subtracted a 1st-order polynomial, which is only a straight line fit, as shown in Fig. 3.7.

However, because the baseline was drifting significantly, I decided to subtract a 4th-order polynomial in time to the data for each Stokes parameter from the FITS file and scan (i.e., to the complete set of zig-zags for each of the 23 scans for Tau A and 18 scans for Orion), the result of which is as shown in Fig. 3.8.

The standard deviation was calculated for the data, which shows how much variation or dispersion exists from the median or the expected value. The fitting

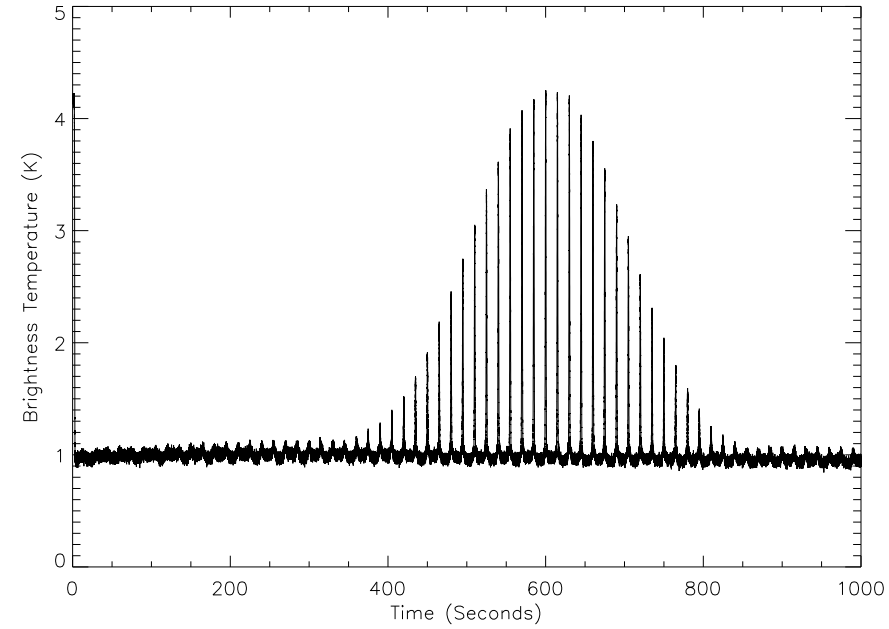

(a) Tau A scan

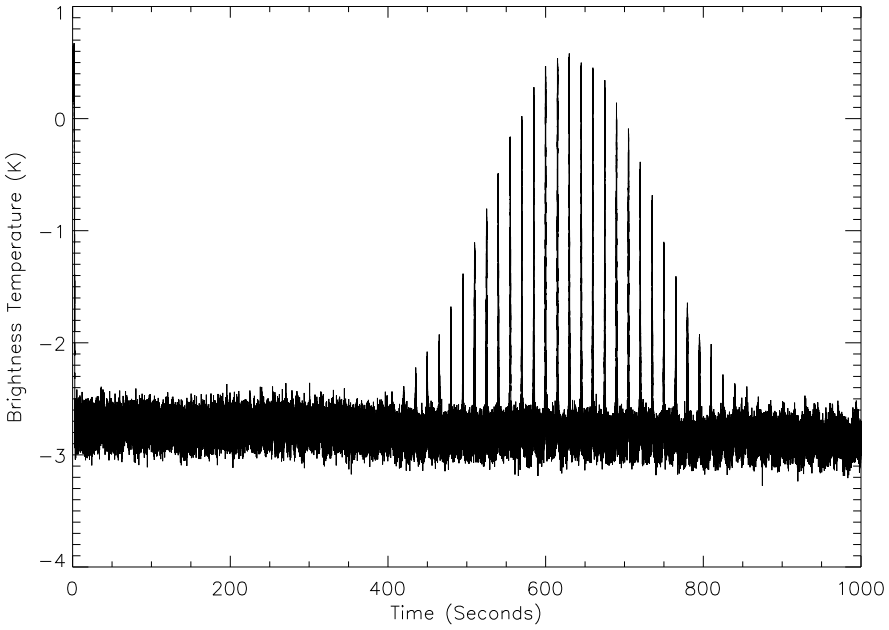

(b) Orion scan

Figure 3.6: A single scan of Tau A (top) and Orion (bottom) showing a reasonably flat baseline.

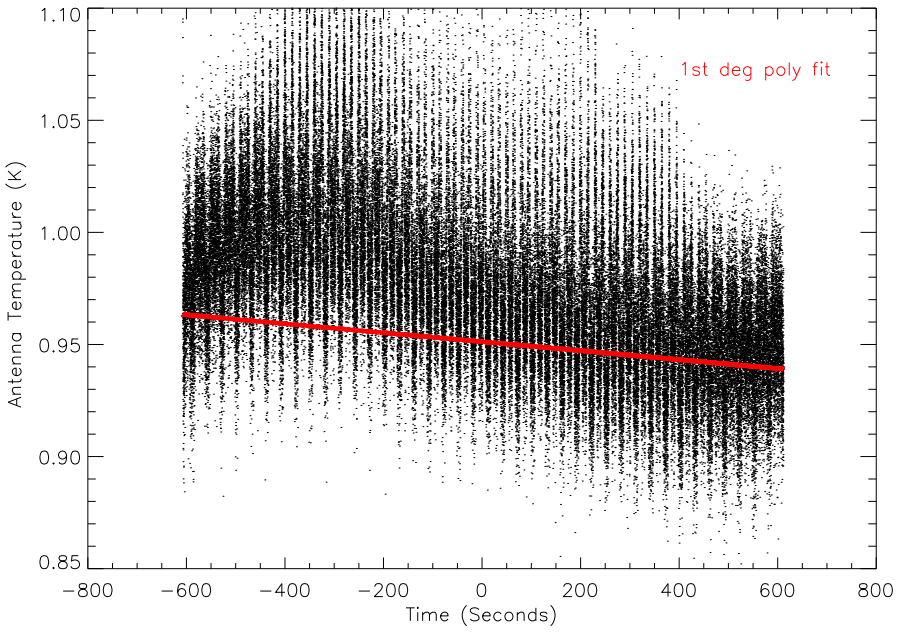

(a) Tau A scan

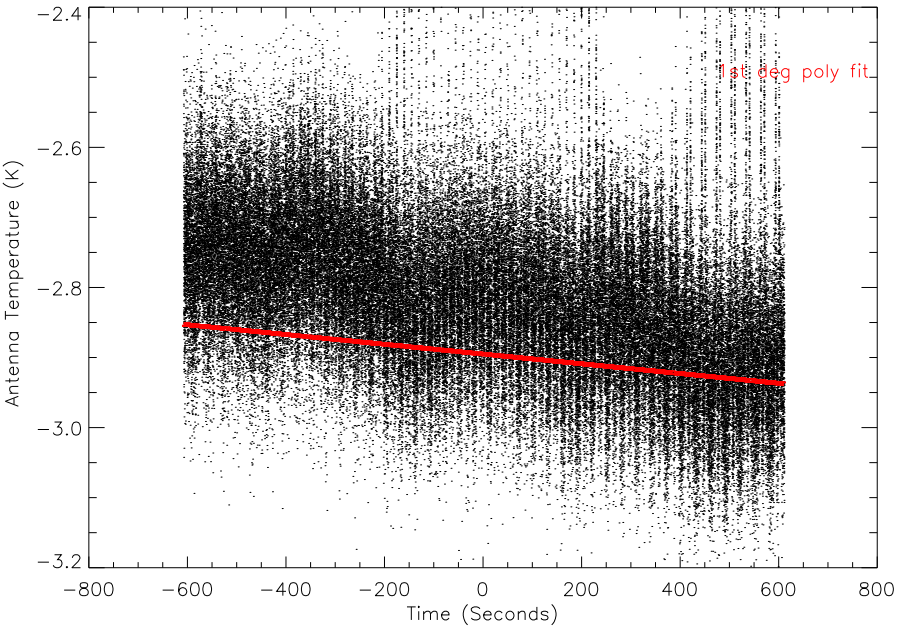

(b) Orion scan

Figure 3.7: First degree polynomial fitting on Tau A scan (top) and Orion (bottom). The plot shows first-order polynomial fit in time, which is only a straight line fit, to Stokes I data.

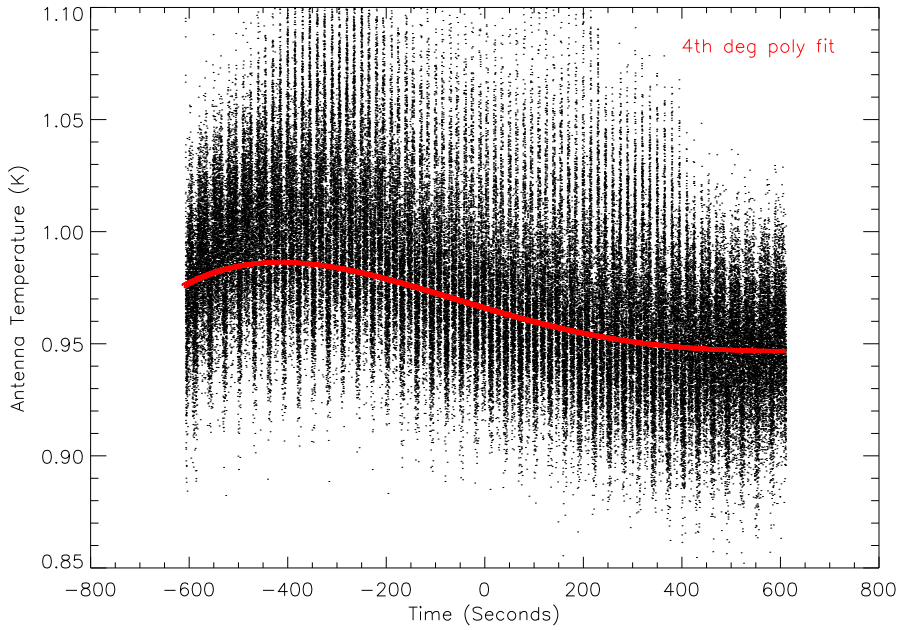

(a) Tau A scan

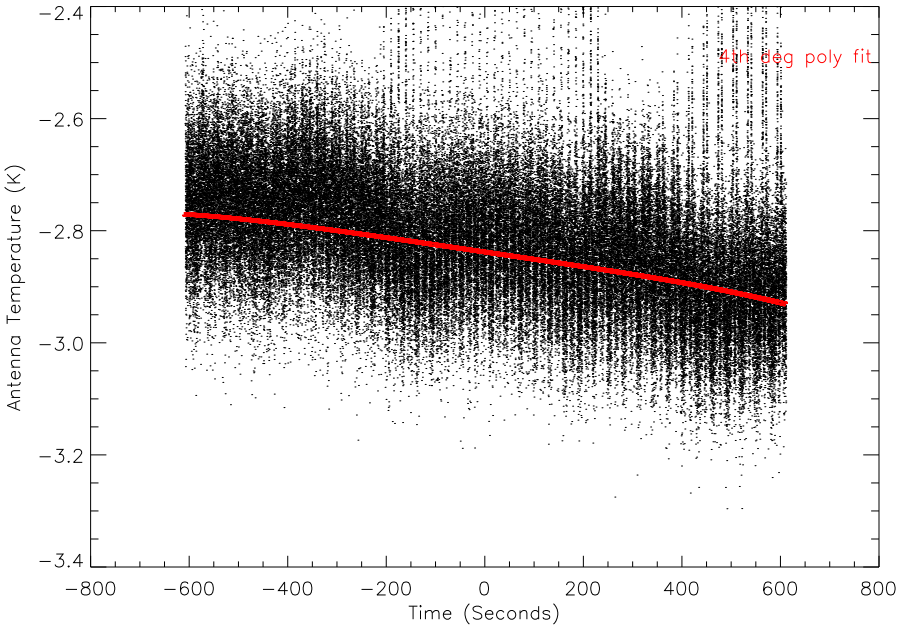

(b) Orion scan

Figure 3.8: Fourth degree polynomial fitting on Tau A scan (top) and Orion (bottom). The plot shows fourth-order polynomial fit in time to Stokes I data.

was iterative, clipping points more than 3 standard deviations from the best-fit polynomial on each iteration; this converges in 1 or 2 cycles. This procedure removes the baseline from each Stokes parameter. Fig. 3.9 shows the resulting data after baseline removal, which sits on an approximate zero level (the baseline removal program that I developed can be found in Appendix A). As discussed earlier, each raster starts by pointing the telescope directly at the source. Then the telescope moves off to the bottom left-hand corner of the raster pattern, and starts the zig-zag series of rasters. The big vertical line seen in the plots (in Fig. 3.9) is when the telescope moves off to the bottom left-hand corner of the raster pattern to start the zig-zag series of rasters. Larger noise in Orion scan in Fig. 3.9 is very obvious as this was from the period where the data were affected by the 1.2 Hz oscillations and was much noisier. Also, a tiny bump in seen right next to the source in the Orion scan, which indicates the presence of Orion B.

As seen in Fig. 3.8, both the red lines are a bit low relative to the points, i.e. there seem to be noticeably more points above than below. This is due to the way we do the fit, starting by excluding all points above the median, so obviously the first attempt at a baseline fit will be pretty low. Then we re-do, excluding points which are greater than 3 standard deviations from the first baseline fit. But since that was low, the excluded points will nearly all be above the line, including not just the on-source points but also noise and points where the baseline is high, e.g. the ones near t = −400 sec in the Tau A scan. So the next fit is still a bit low. We iterate to reduce this effect but it does not completely go away. Nevertheless, the fitted baseline removes the obvious trend which is the main point.

The next step was to create a data structure for each scan, with data elements I, Q, U, V, RA, Dec and time, and use it to create maps of the Stokes parameters for further analysis.

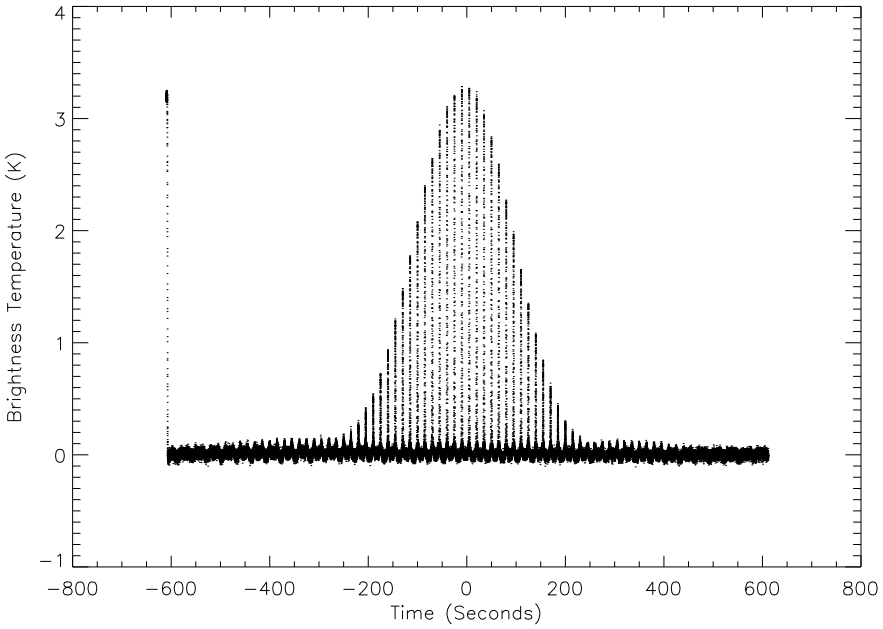

(a) Tau A scan

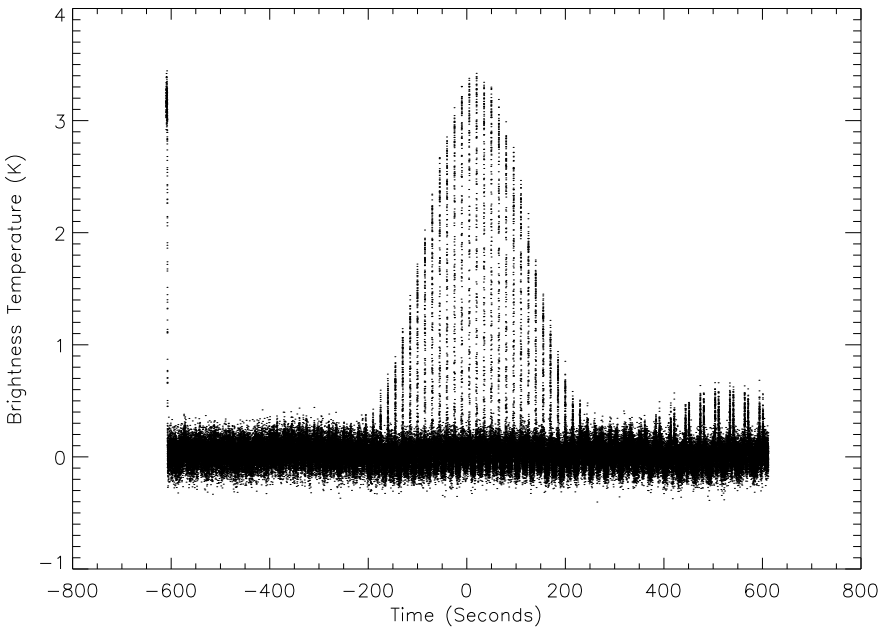

(b) Orion scan

Figure 3.9: Resulting data for Tau A (top) and Orion (bottom) after baseline removal.

Chapter 4

Generating maps of Stokes

Once the baseline was removed, the next step was to make maps of Stokes I, Q, U and V. In this chapter, Section 4.1 gives a description of the code (written by Dr. Patrick Leahy) I used to generate maps of the Stokes parameters and Section 4.2 presents the maps for various scans of Tau A and Orion.

4.1 Method for making maps of Stokes parameters

To generate maps, the first step was to set up parameters for map size and projection. I first calculated the map centre (in degrees) for Tau A and Orion in RA and Dec. Tau A is at coordinates $\alpha = 5^{\mathrm{h}}34^{\mathrm{m}}32^{\mathrm{s}}$ and $\delta = 22°0'52"$, which is 83.63° in RA and 22.01° in Dec. Similarly, Orion is at coordinates $\alpha = 5^{\mathrm{h}}35^{\mathrm{m}}17^{\mathrm{s}}$ and $\delta = -5°23'28"$, which is 83.82° in RA and −5.39° in Dec. The size of the map in RA and Dec was taken to be 10×10 degrees. The size of pixels was decided to be 0.05°. The usual rule of thumb for pixel size is 1/3 FWHM, but the reason behind this particular size of pixels I set was because the FWHM of C-BASS beam is $48'$, and I wanted to map the beam pattern in detail, I had to set the pixel size to be much less than the FWHM of the beam. If I had made the pixel size too small, I would have got less data in each pixel, and more pixels missed completely. I could have probably

doubled it or halved it without having much effect on the results, but in this case 0.05° worked perfectly and maps of size 200×200 pixels were made.

After setting the parameters, I used Dr. Patrick Leahy's 'binmap' code to generate the maps. This code performs the quick binning of time-ordered data stored in a structure. Given the data structure, the co-ordinate system, the map centre in RA and Dec (in degrees), size of map in RA and Dec (in degrees), size of pixel (in degrees) and the list of channels to be binned (I, Q, U, V), it outputs a structure containing the basic fits header, the binned channels map and the hit count map. Each hit-count-map pixel represents the number of samples contributing to the corresponding sky map pixel.

Firstly, this code calculates the exact dimensions of the map from the parameters provided. Once the map size is determined, it also sets the projection (tangent projection in this case). A FITS header is created using astrolib routine 'MKHDR' (with required keywords BITPIX, NAXIS, NAXIS1 etc) and then the 'PUTAST' astrolib routine was used to put the WCS (World Coordinate System) astrometry parameters (such as CDELT, CRPIX, CRVAL and CTYPE) into the FITS header. 'ADXY' astrolib routine was then used to convert the astronomical to pixel coordinates, which uses the image header to compute X and Y positions, given the RA and Dec in decimal degrees.

Once the RA and Dec are converted into pixels, the data points in the region covered by the map are calculated. This also involves discarding the pixels where NaNs (Not-a-Number) are present. The good data points that are in the region covered by the map are then filled with I, Q, U, V values. A two dimensional map is binned with the Stokes parameters and a hits count map is also made using the 'HISTOGRAM' routine with a bin size of 1. Finally, a map structure is created which has the structure elements: header, I, Q, U, V and hit count. The structure elements (except header) are of size [200, 200] where 200×200 is the number of pixels in the map. The binmap script I used to generate maps can be found in Appendix A.

Fig. 4.1 shows the intensity map of Tau A and Orion for the complete raster schedule (i.e., all raster scans combined) projected in RA/Dec (tangent plane) and binned into 3 arcmin pixels. These were made using 'ximview', a program written by Dr. Patrick Leahy.

The "butterfly pattern" of the map we see is because we are doing a series of scans through a source and each scan is at constant elevation, i.e., just moving in azimuth. However, the elevation changes between scans to follow the source rise and set. When I translate the Az-El coordinate system to RA-Dec, I see that the position angle (orientation) of each scan on the sky changes with elevation. The difference in position angle between scans is in fact just the difference in parallactic angle. I have also made plots of parallactic angle vs time (see Fig. 5.3 in Section 5.3) and in the plots it is seen that most of the change in angle happens over a relatively short space of time, just around the time the source reaches its maximum elevation, when it crosses the meridian. So the net effect is that at first there is not much change in angle between scans when the source is at low elevation and the scans are long. Then, when the scans are really short, the angle swings quite sharply but this does not affect the outline on the map because the short new scans fit inside the long old ones. Finally, as the source begins to set, the scans get longer again, but more or less at the final parallactic angle, which gives us the second pair of wings on the butterfly pattern.

The intensity map in Fig. 4.1 is produced after doing baseline removal. However, I also wanted to see the original data, which had not undergone baseline removal, to see if my baseline fitting code had improved the quality of the data. So I used ximview and binmap to see the original data, and this is as shown in Fig. 4.2. It clearly shows that baseline removal has significantly improved the quality of the maps.

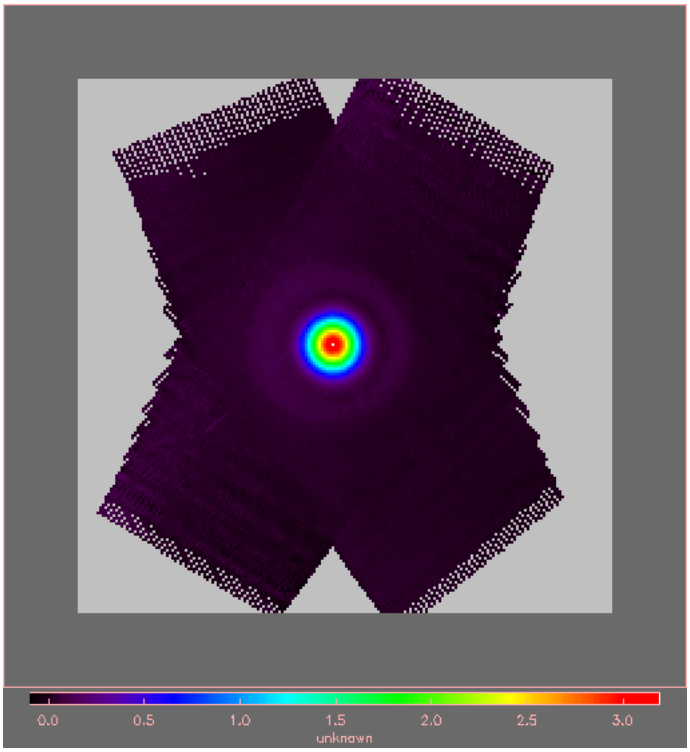

(a) Tau A Intensity map

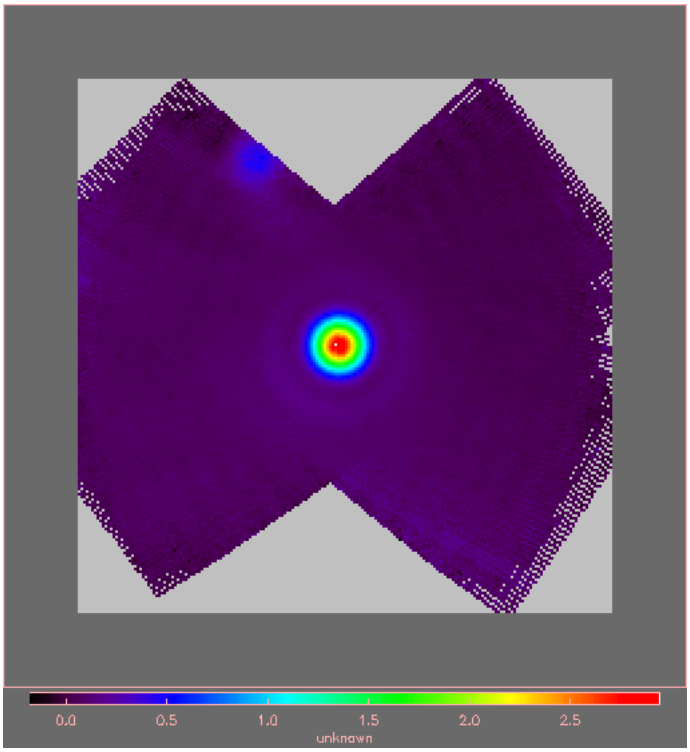

(b) Orion Intensity map

Figure 4.1: Intensity map of Tau A (top) and Orion (bottom) in RA/Dec (tangent plane) binned into 3 arcmin pixels for the complete raster schedule, in antenna temperature (K). The numerical scale of the colour table is in range [0.0,3.0] for Tau A and [0.0,2.5] for Orion.

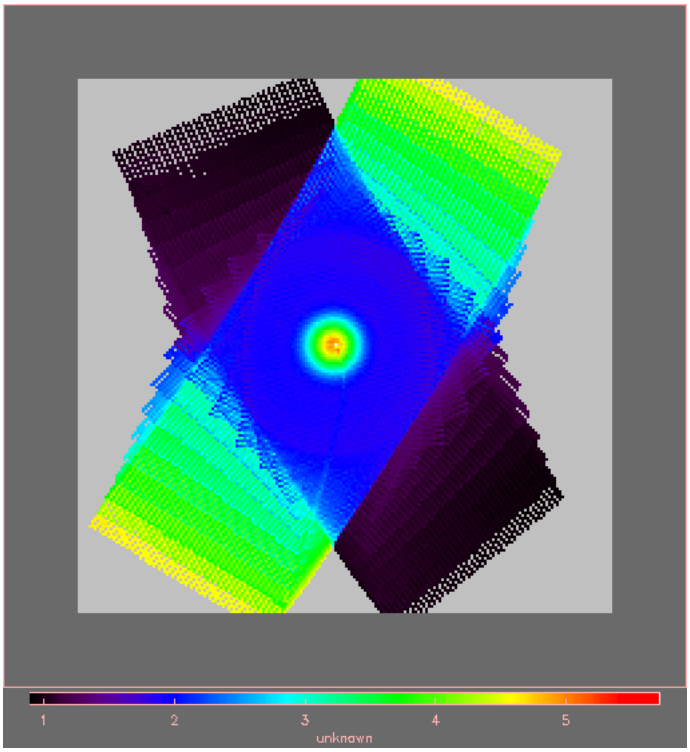

(a) Tau A Intensity map

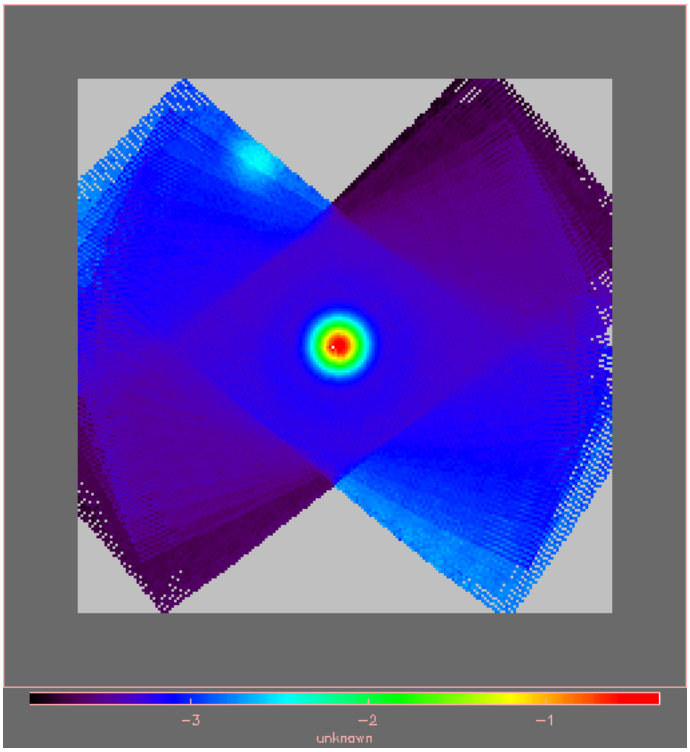

(b) Orion Intensity map

Figure 4.2: Intensity map of Tau A (top) and Orion (bottom) in RA/Dec (tangent plane) binned into 3 arcmin pixels for the complete raster schedule, in antenna temperature (K), before undergoing baseline removal. The numerical scale of the colour table is in range [1,5] for Tau A and [-3,-1] for Orion.

4.2 Maps of Tau A and Orion

Once the maps of whole raster schedule were made, the next task was to generate maps of individual scans of Tau A (17-Jul-2013 data) and Orion (28-Apr-2013 data). These are shown in Fig. 4.3 - Fig. 4.9 for Tau A and Fig. 4.10 - Fig. 4.14 for Orion. I am not presenting maps of all the scans here, selecting mainly those showing the effect of rotating parallactic angle on the source scans. The maps were auto-scaled in ximview and a transfer function 'Asinh' was applied to them. The original image data in ximview is converted to displayed colour in a two-stage process. First, the image data is scaled into the range [0, 255] via a "transfer function", then these values are interpreted as colours via the colour table. Auto-scaling scales the image so that "noise-like" fluctuations around the zero level are visible but don't use up too much of the colour scale, such that the bright features are visible rather than being completely saturated.

One particular thing to notice about these maps is that they differ in size. The first few maps are large, then they get smaller with elevation, followed by larger maps again at the end of the scan. This is because the rasters consist of a zig-zag series of scans at constant elevation as explained earlier, at a range of offsets from the elevation of the target source, so as to sweep out a rectangular region centred on the source. The length of each scan in azimuth is always the same. The length on the sky in degrees of a scan of fixed length in azimuth gets shorter as the elevation increases, until at the zenith (el=90) we can scan as much as we like in azimuth but we still are just observing a single point. During a single raster, the elevation does not change enough for the effect to be noticeable. But if we spend 7–12 hours doing a series of rasters, in this time the source will be rising at first, then gradually setting. As it rises, the source elevation increases. Obviously, this means that rasters when the source is near its maximum elevation (near the middle of the series), will correspond to shorter sky patches.

The Tau A maps clearly show Q and U polarization as expected. This is the true

polarization of Tau A (rotating with parallactic angle) plus the leakage from intensity. Any offsets in Q and U have been removed by the baseline fitting. However, the maps also show some V polarization, which denotes the presence of circular polarization. Since Tau A is only linearly polarized, V polarization should be absent. Therefore, there may be some instrumental leakage, but to confirm it I also looked at maps of Orion. Orion maps Fig. 4.10 - Fig. 4.14 also show some Q, U and V polarization. Since Orion is an unpolarized source, Q, U and V polarization should be absent, and their presence indicates instrumental leakage.

Also, there is a "Washboard pattern" - a pattern of ripples perpendicular to the scan lines observed in the maps. It varies dramatically in amplitude with time, even within a scan. It is pretty strong in I and clearly visible in all the maps. In general it seems stronger in Q than U. This is due to the presence of 1.2 Hz oscillations in C-BASS data. The pattern repeats at fixed azimuths, otherwise it would not produce stripes perpendicular to the scan direction; this essentially means that the scan pattern is synchronous with 1.2 Hz oscillations.

A strong interference was also present in the data, which was flagged by the pipeline RFI code, leaving the blank strip near the middle in Tau A scan 15.

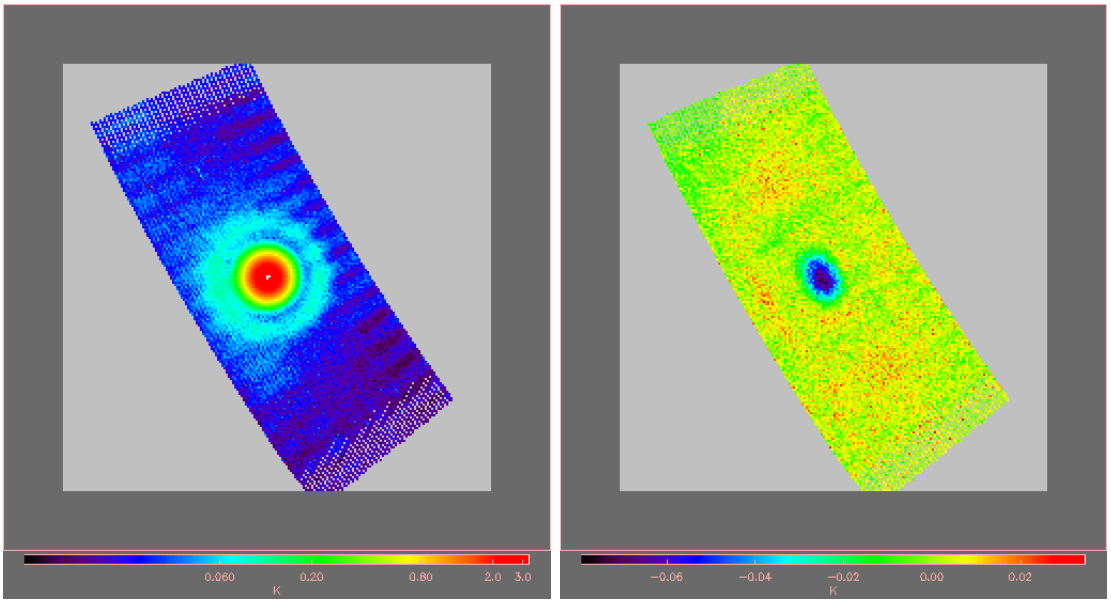

(a) Stokes I (b) Stokes Q

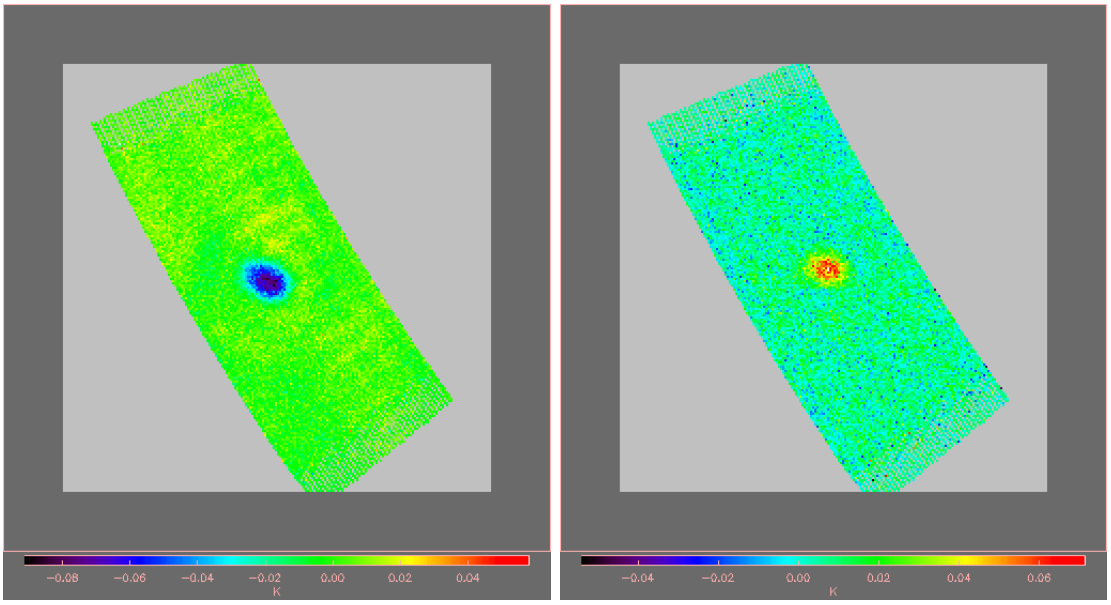

(c) Stokes U (d) Stokes V

Figure 4.3: Maps of Tau A at 5 GHz in antenna temperature (K) for intensity I (top-left), Q polarization (top-right), U polarization (bottom-left) and V polarization (bottom-right) binned into 3 arcmin pixels for scan 0. The numerical scale of the colour table is in range [0.060,3.0] for Stokes I, [-0.06,0.02] for Stokes Q, [-0.08,0.04] for Stokes U and [-0.04,0.06] for Stokes V respectively.

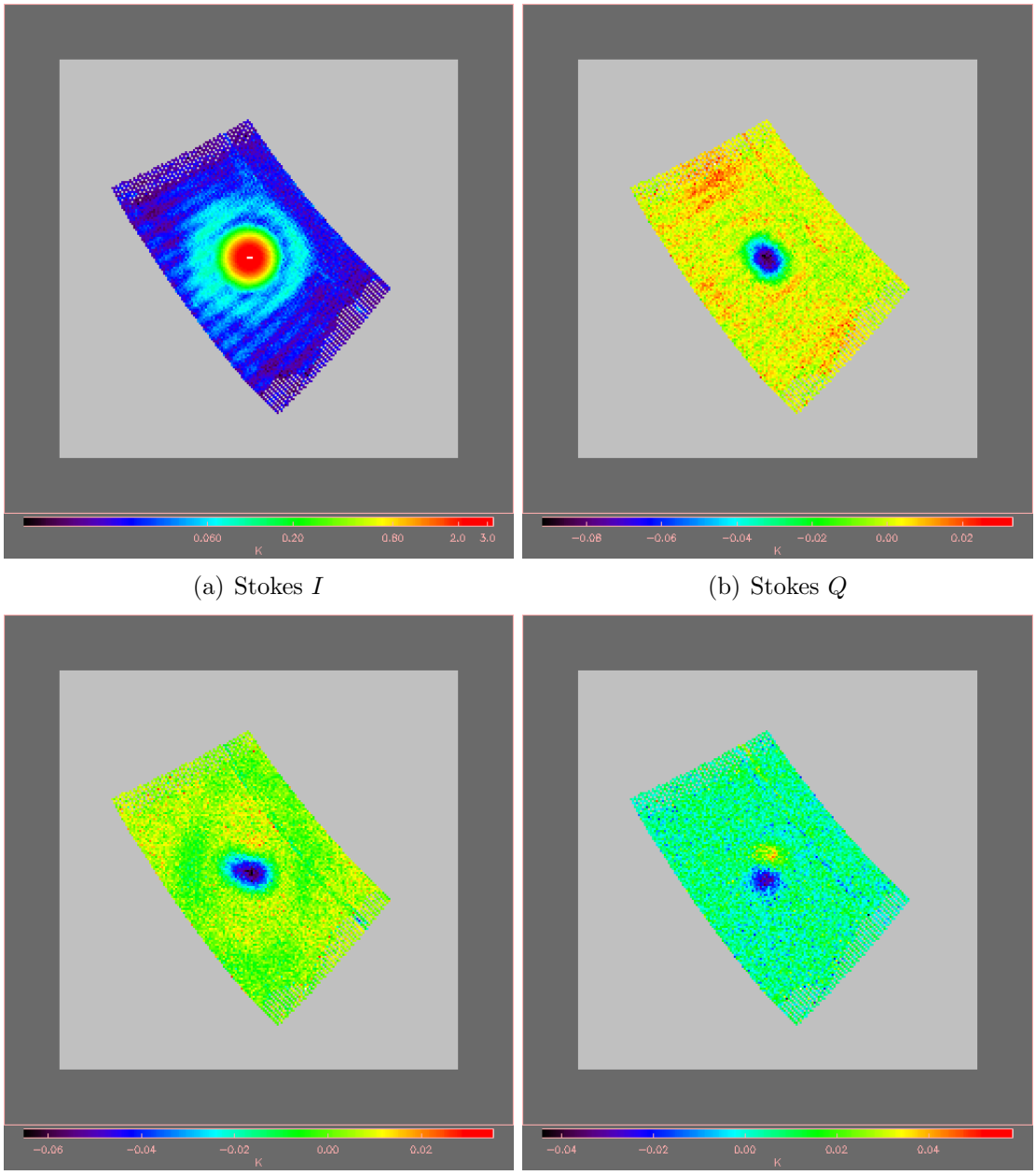

(a) Stokes I (b) Stokes Q

(c) Stokes U (d) Stokes V

Figure 4.4: Maps of Tau A at 5 GHz in antenna temperature (K) for intensity I (top-left), Q polarization (top-right), U polarization (bottom-left) and V polarization (bottom-right) binned into 3 arcmin pixels for scan 5. The numerical scale of the colour table is in range [0.060,3.0] for Stokes I, [-0.08,0.02] for Stokes Q, [-0.06,0.02] for Stokes U and [-0.04,0.04] for Stokes V respectively.

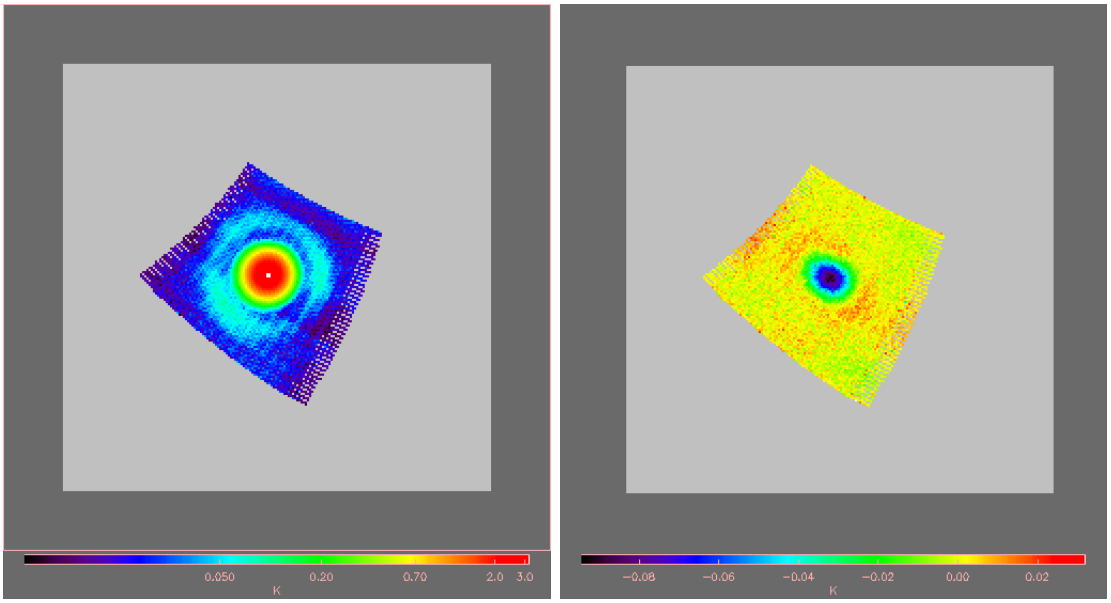

(a) Stokes I (b) Stokes Q

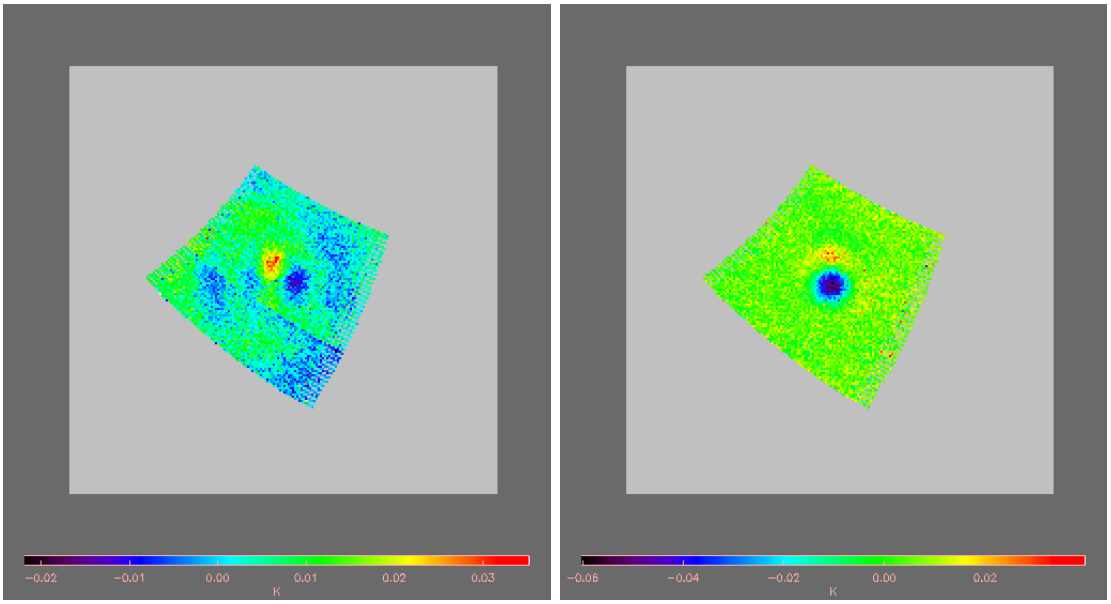

(c) Stokes U (d) Stokes V

Figure 4.5: Maps of Tau A at 5 GHz in antenna temperature (K) for intensity I (top-left), Q polarization (top-right), U polarization (bottom-left) and V polarization (bottom-right) binned into 3 arcmin pixels for scan 8. The numerical scale of the colour table is in range [0.050,3.0] for Stokes I, [-0.08,0.02] for Stokes Q, [-0.02,0.03] for Stokes U and [-0.06,0.02] for Stokes V respectively.

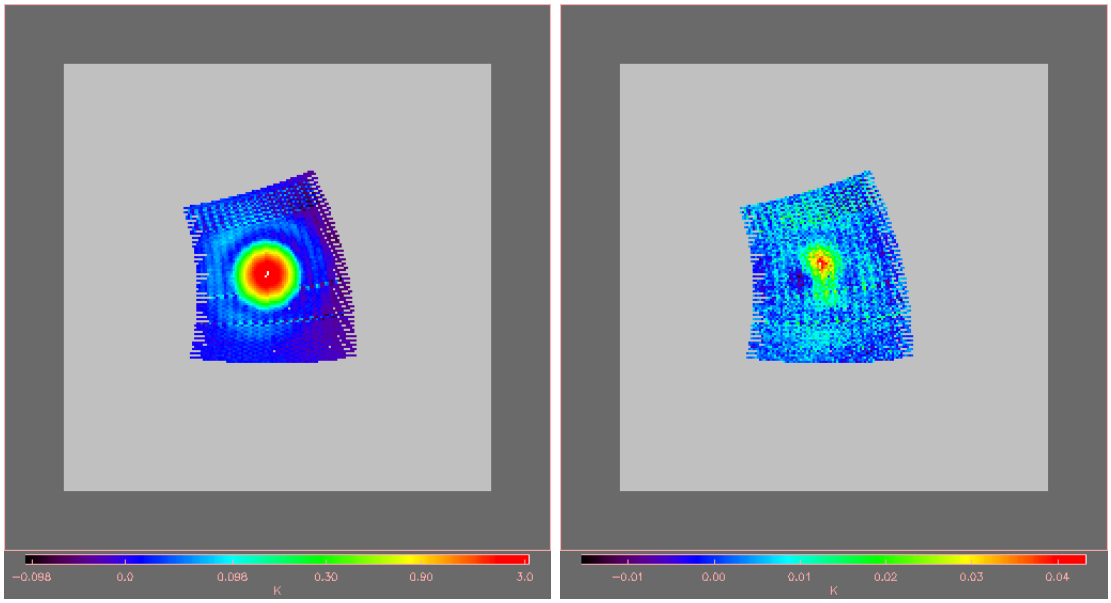

(a) Stokes I (b) Stokes Q

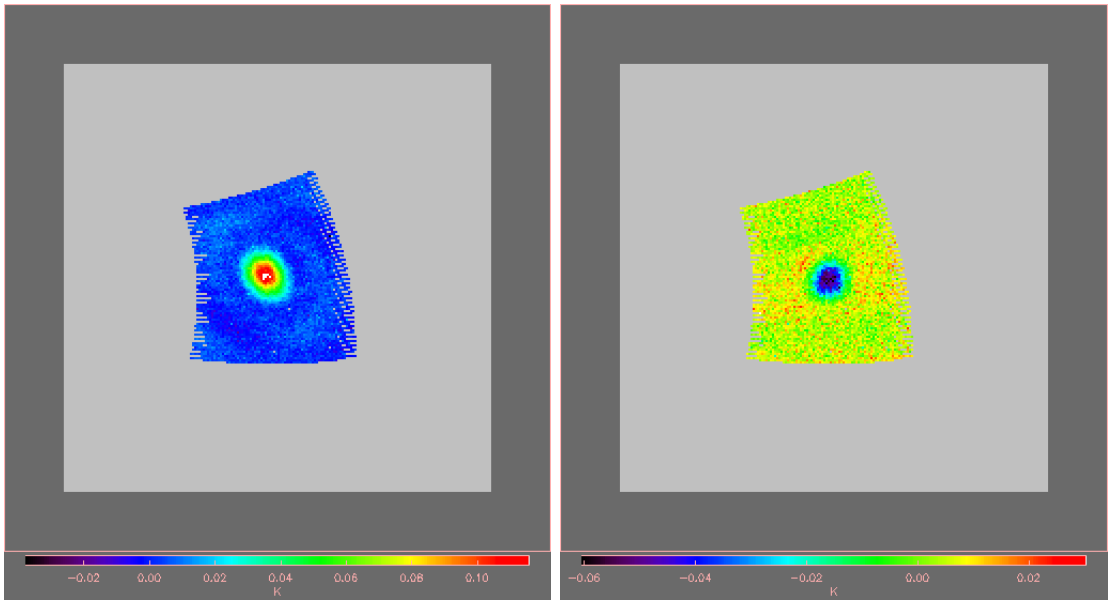

(c) Stokes U (d) Stokes V

Figure 4.6: Maps of Tau A at 5 GHz in antenna temperature (K) for intensity I (top-left), Q polarization (top-right), U polarization (bottom-left) and V polarization (bottom-right) binned into 3 arcmin pixels for scan 11. The numerical scale of the colour table is in range [-0.098,3.0] for Stokes I, [-0.01,0.04] for Stokes Q, [-0.02,0.10] for Stokes U and [-0.06,0.02] for Stokes V respectively.

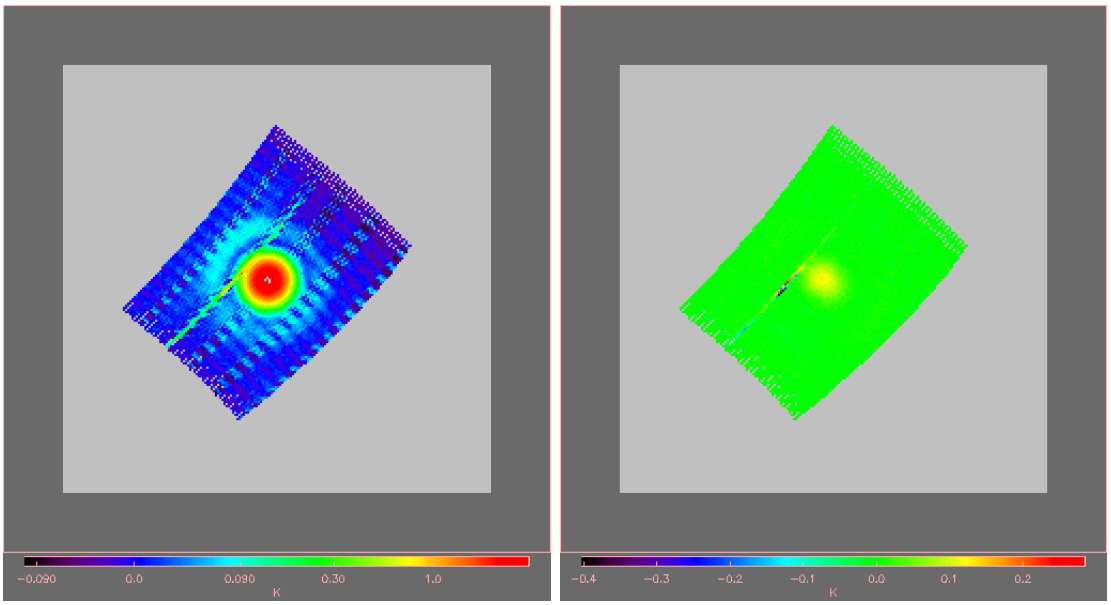

(a) Stokes I (b) Stokes Q

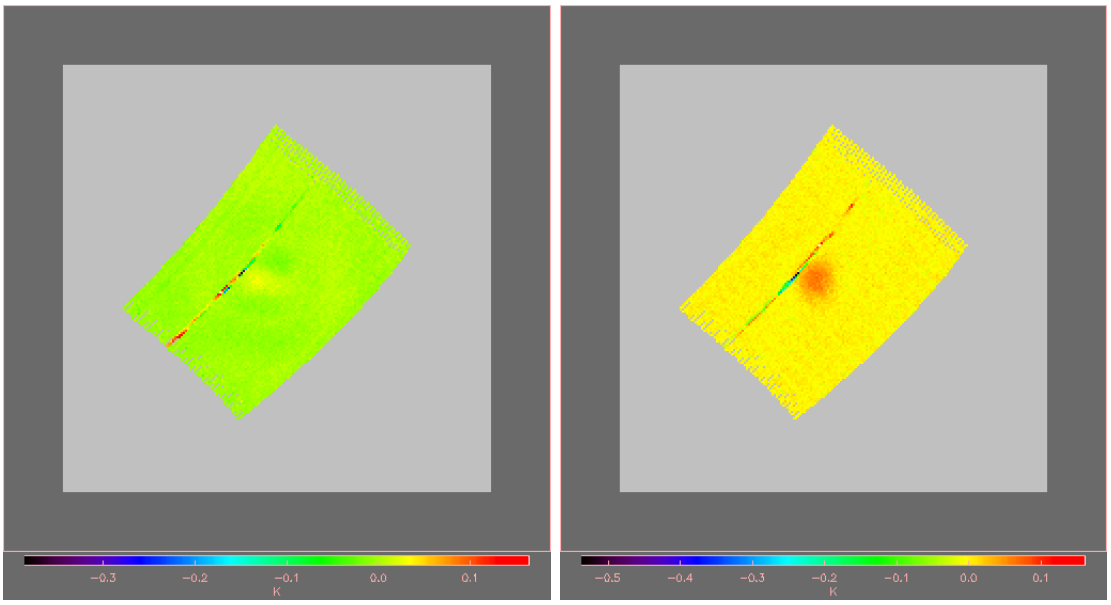

(c) Stokes U (d) Stokes V

Figure 4.7: Maps of Tau A at 5 GHz in antenna temperature (K) for intensity I (top-left), Q polarization (top-right), U polarization (bottom-left) and V polarization (bottom-right) binned into 3 arcmin pixels for scan 15. A strong interference present in the data was flagged by the pipeline RFI code, leaving the blank strip near the middle in the scan. The numerical scale of the colour table is in range [-0.090,1.0] for Stokes I, [-0.4,0.2] for Stokes Q, [-0.3,0.1] for Stokes U and [-0.5,0.1] for Stokes V respectively.

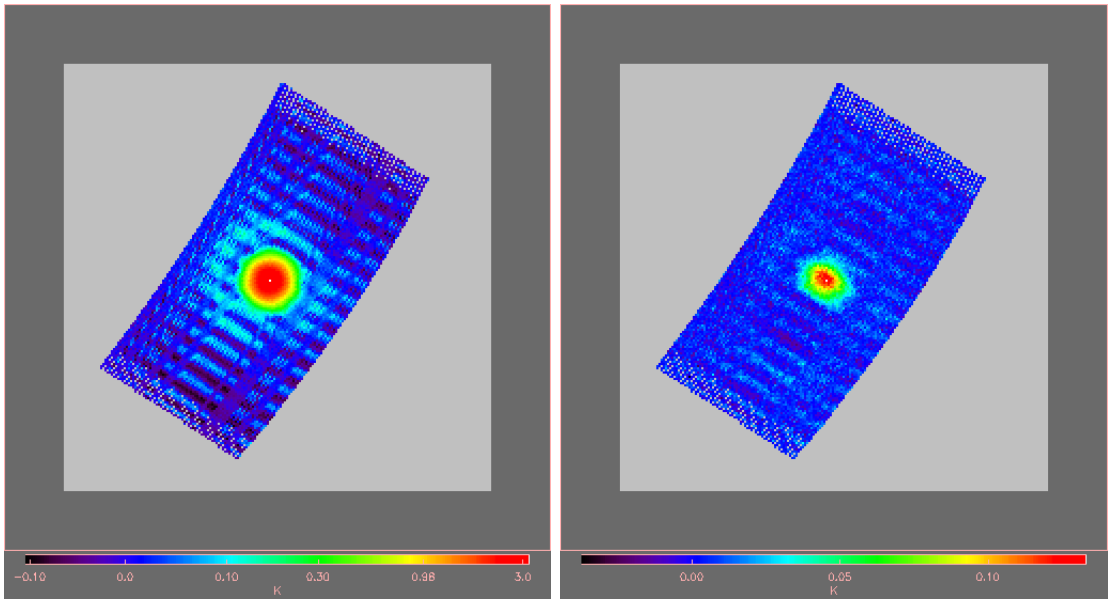

(a) Stokes I (b) Stokes Q

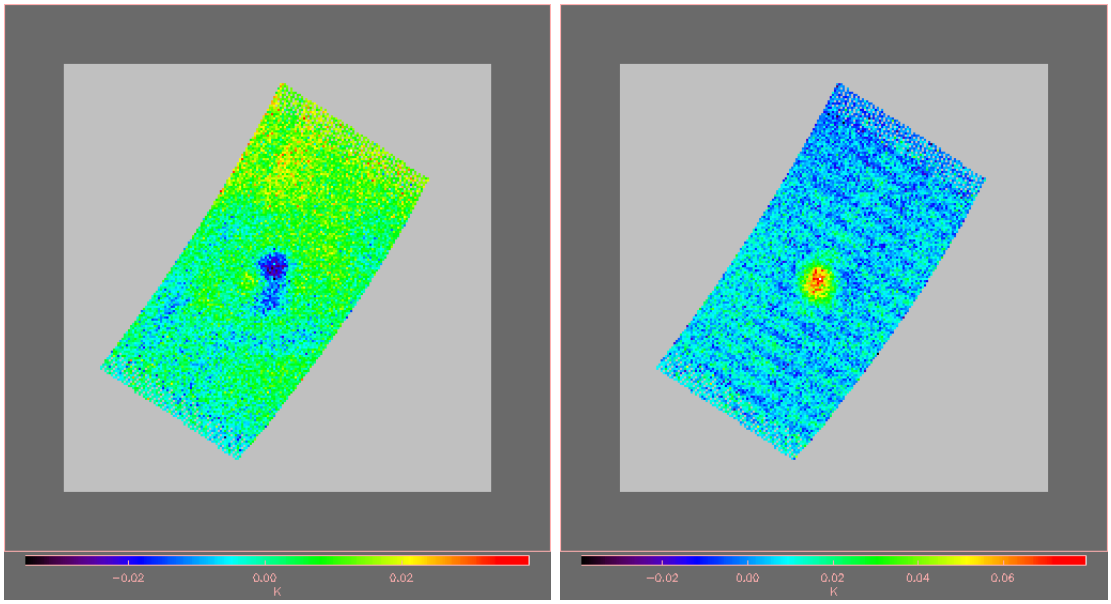

(c) Stokes U (d) Stokes V

Figure 4.8: Maps of Tau A at 5 GHz in antenna temperature (K) for intensity I (top-left), Q polarization (top-right), U polarization (bottom-left) and V polarization (bottom-right) binned into 3 arcmin pixels for scan 18. The numerical scale of the colour table is in range [-0.10,3.0] for Stokes I, [0.00,0.10] for Stokes Q, [-0.02,0.02] for Stokes U and [-0.02,0.06] for Stokes V respectively.

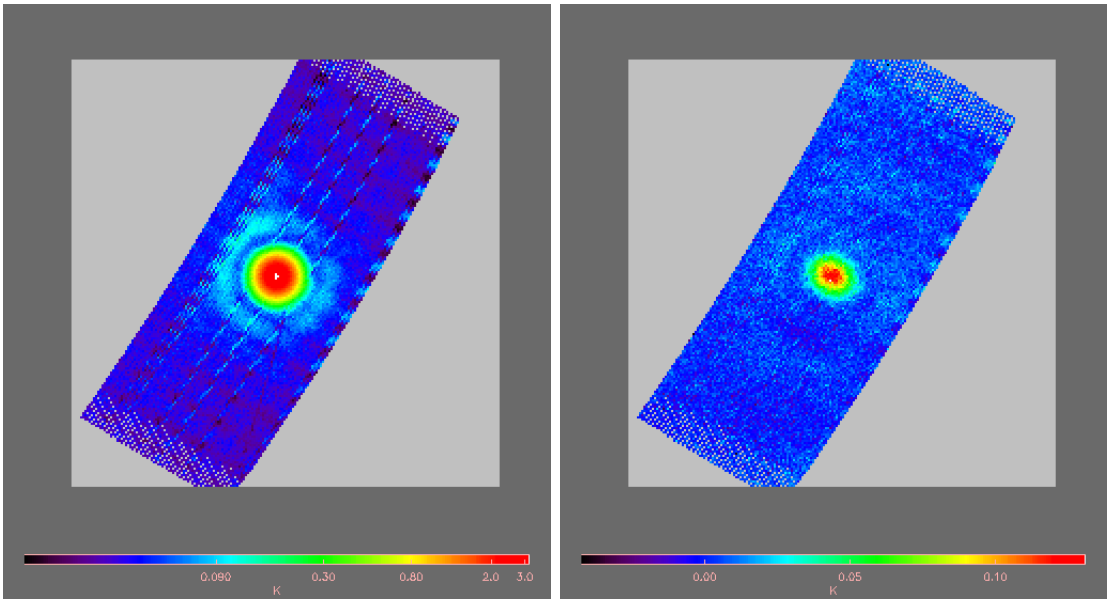

(a) Stokes I (b) Stokes Q

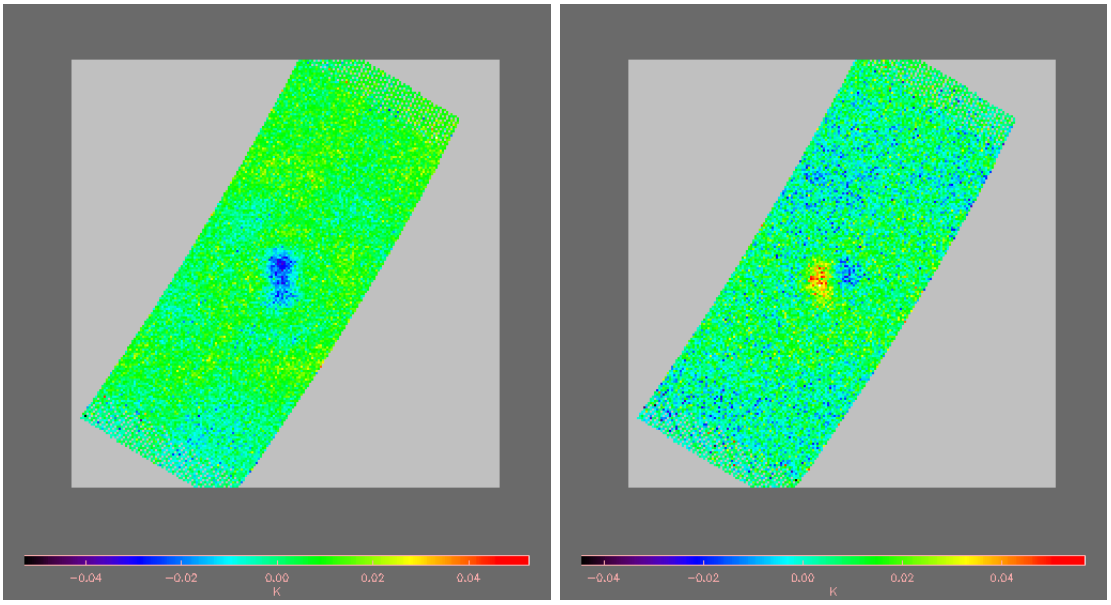

(c) Stokes U (d) Stokes V

Figure 4.9: Maps of Tau A at 5 GHz in antenna temperature (K) for intensity I (top-left), Q polarization (top-right), U polarization (bottom-left) and V polarization (bottom-right) binned into 3 arcmin pixels for scan 22. The numerical scale of the colour table is in range [0.090,3.0] for Stokes I, [0.00,0.10] for Stokes Q, [-0.04,0.04] for Stokes U and [-0.04,0.04] for Stokes V respectively.

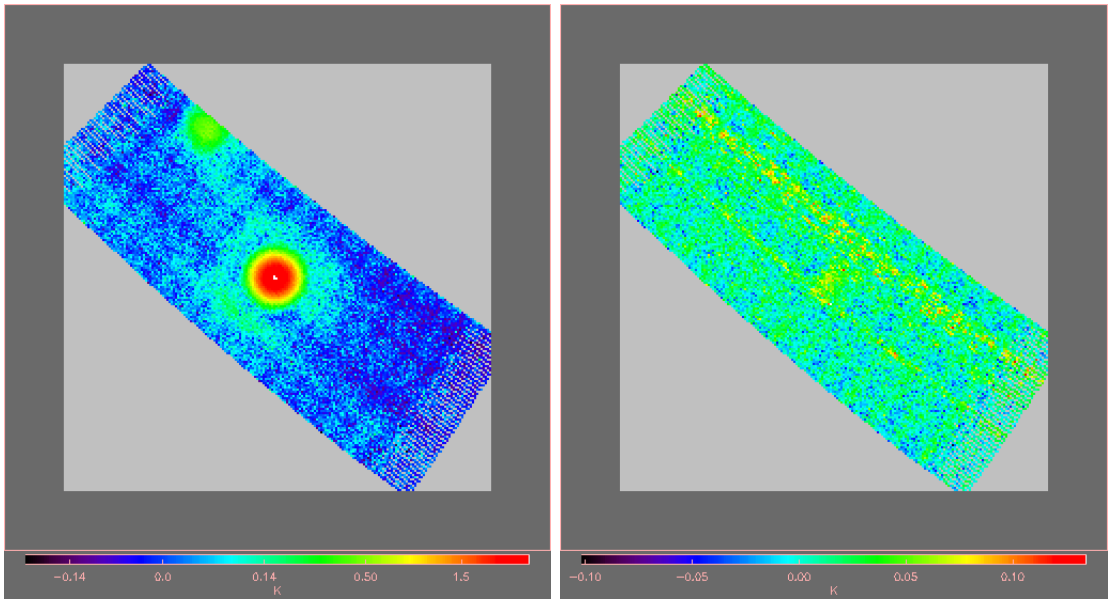

(a) Stokes I (b) Stokes Q

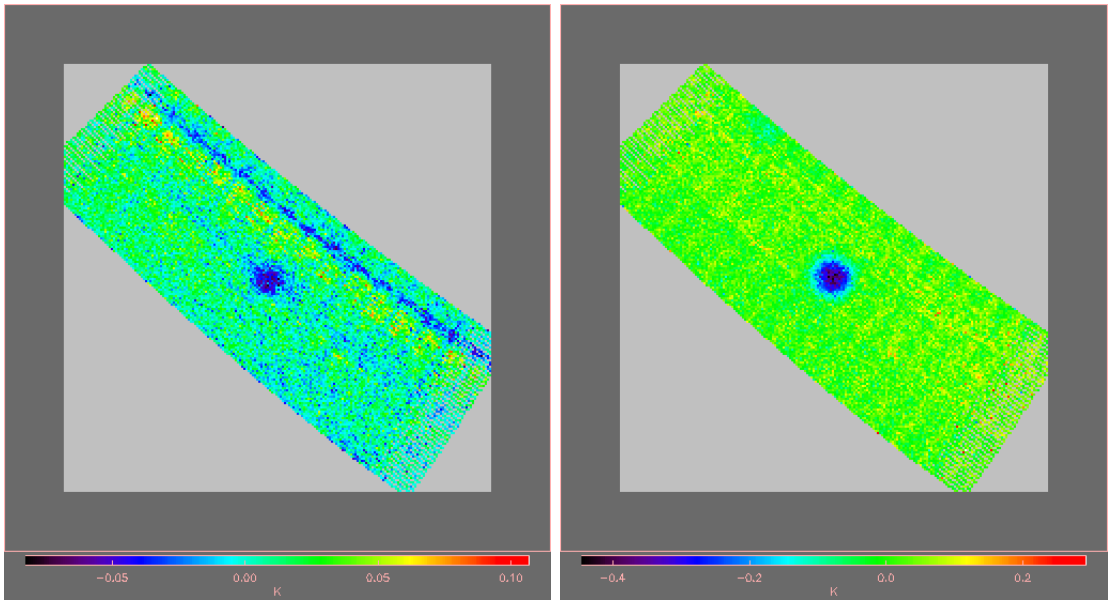

(c) Stokes U (d) Stokes V

Figure 4.10: Maps of Orion at 5 GHz in antenna temperature (K) for intensity I (top-left), Q polarization (top-right), U polarization (bottom-left) and V polarization (bottom-right) binned into 3 arcmin pixels for scan 0. The numerical scale of the colour table is in range [-0.14,1.5] for Stokes I, [-0.10,0.10] for Stokes Q, [-0.05,0.10] for Stokes U and [-0.4,0.2] for Stokes V respectively.

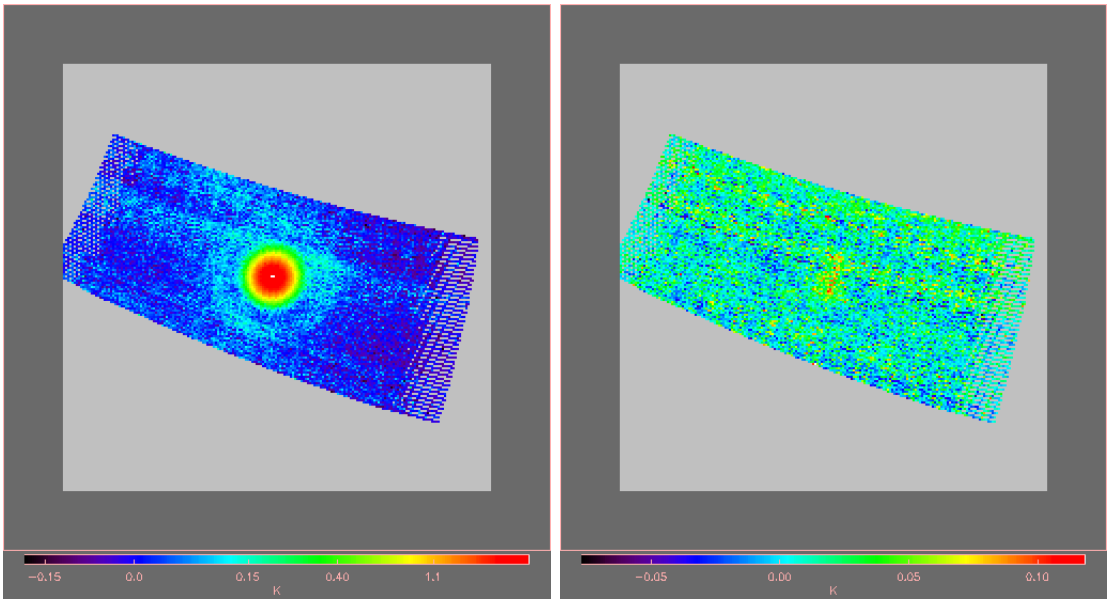

(a) Stokes I (b) Stokes Q

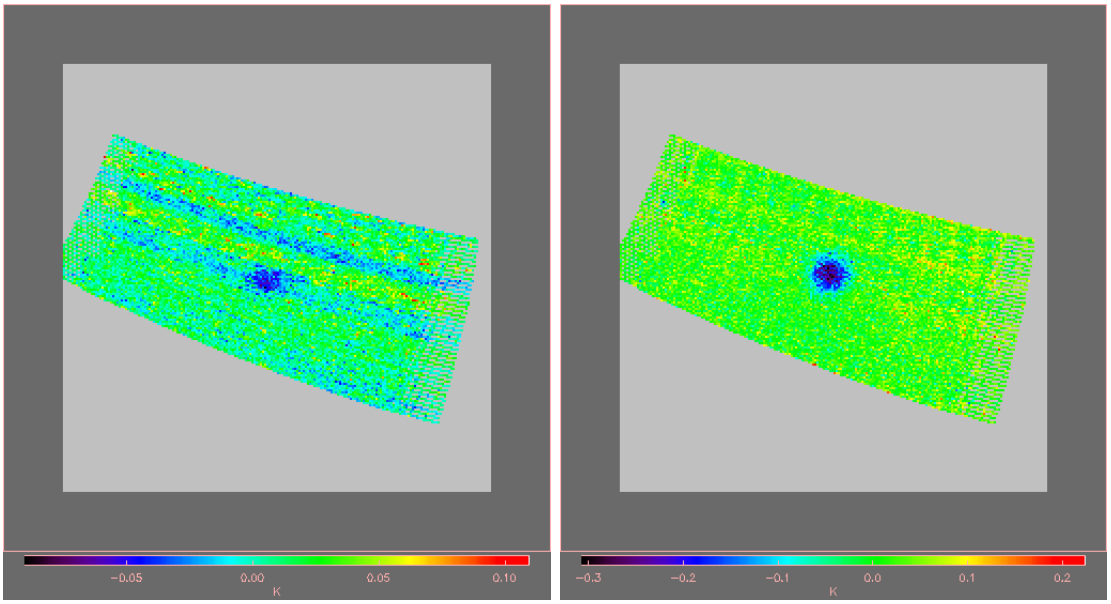

(c) Stokes U (d) Stokes V

Figure 4.11: Maps of Orion at 5 GHz in antenna temperature (K) for intensity I (top-left), Q polarization (top-right), U polarization (bottom-left) and V polarization (bottom-right) binned into 3 arcmin pixels for scan 5. The numerical scale of the colour table is in range [-0.15,1.1] for Stokes I, [-0.05,0.10] for Stokes Q, [-0.05,0.10] for Stokes U and [-0.3,0.2] for Stokes V respectively.

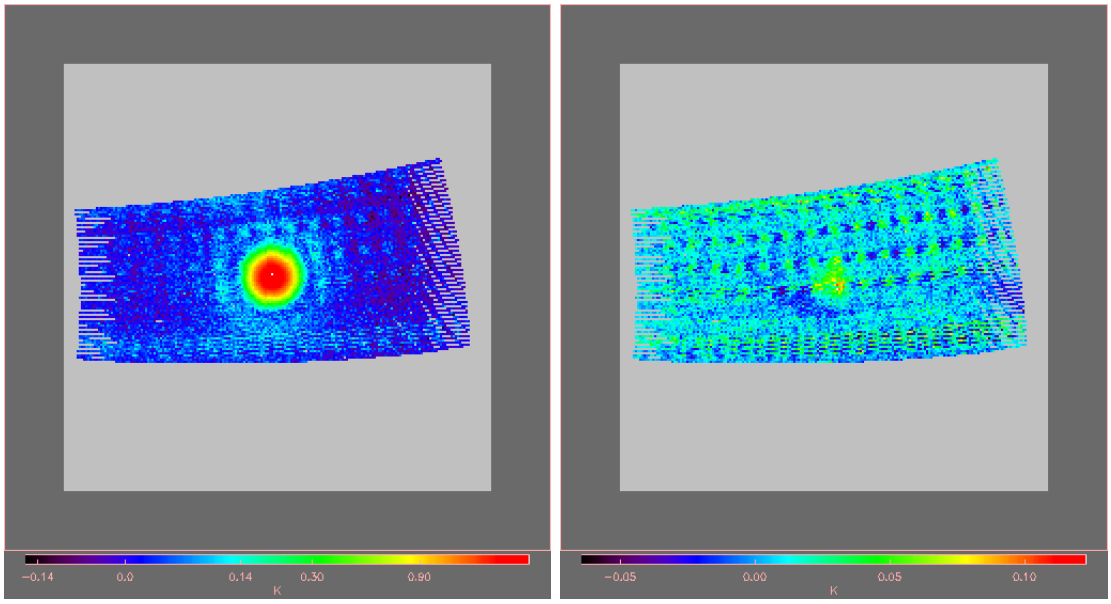

(a) Stokes I (b) Stokes Q

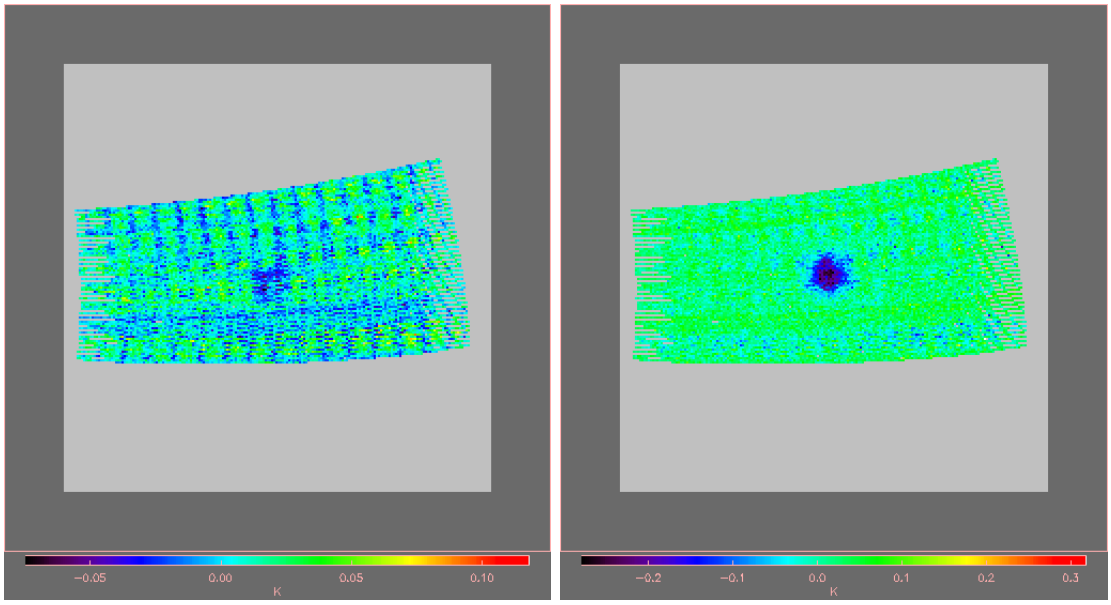

(c) Stokes U (d) Stokes V

Figure 4.12: Maps of Orion at 5 GHz in antenna temperature (K) for intensity I (top-left), Q polarization (top-right), U polarization (bottom-left) and V polarization (bottom-right) binned into 3 arcmin pixels for scan 9. The numerical scale of the colour table is in range [-0.14,0.90] for Stokes I, [-0.05,0.10] for Stokes Q, [-0.05,0.10] for Stokes U and [-0.2,0.3] for Stokes V respectively.

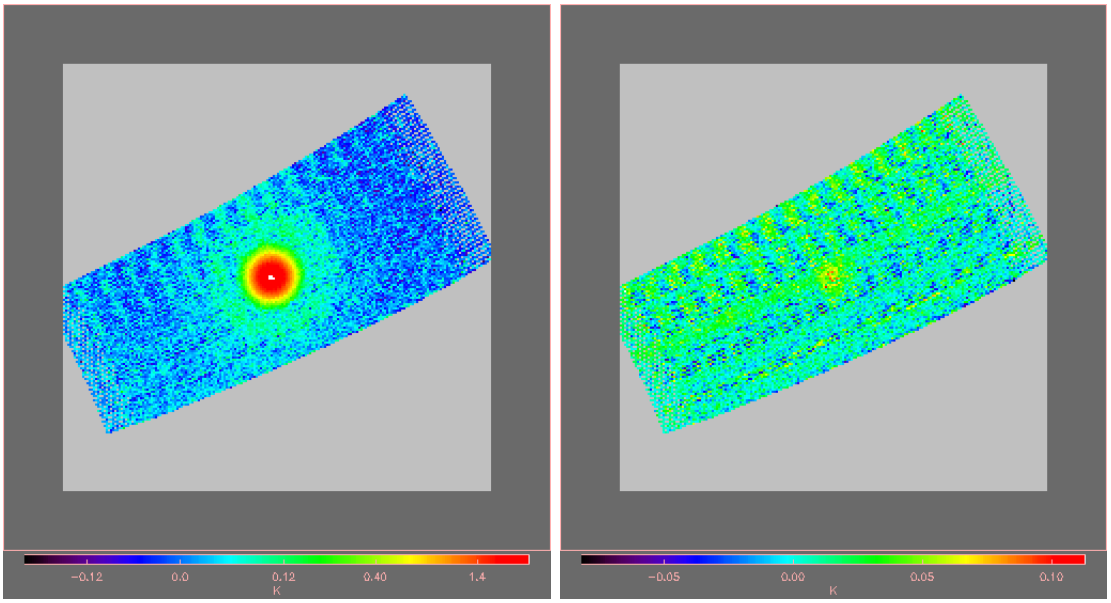

(a) Stokes I (b) Stokes Q

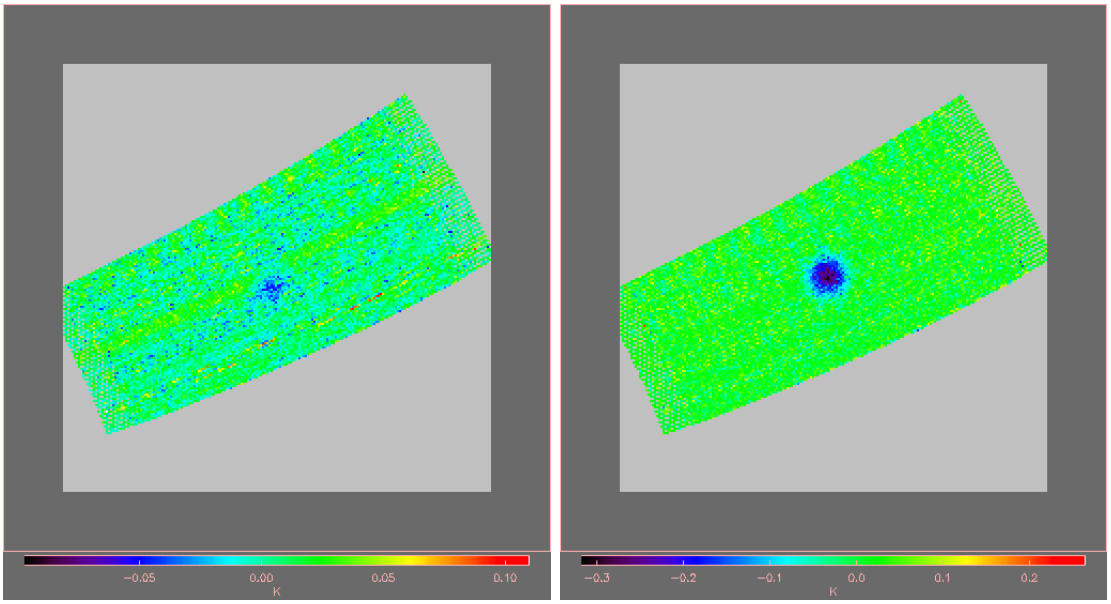

(c) Stokes U (d) Stokes V

Figure 4.13: Maps of Orion at 5 GHz in antenna temperature (K) for intensity I (top-left), Q polarization (top-right), U polarization (bottom-left) and V polarization (bottom-right) binned into 3 arcmin pixels for scan 13. The numerical scale of the colour table is in range [-0.12,1.4] for Stokes I, [-0.05,0.10] for Stokes Q, [-0.05,0.10] for Stokes U and [-0.3,0.2] for Stokes V respectively.

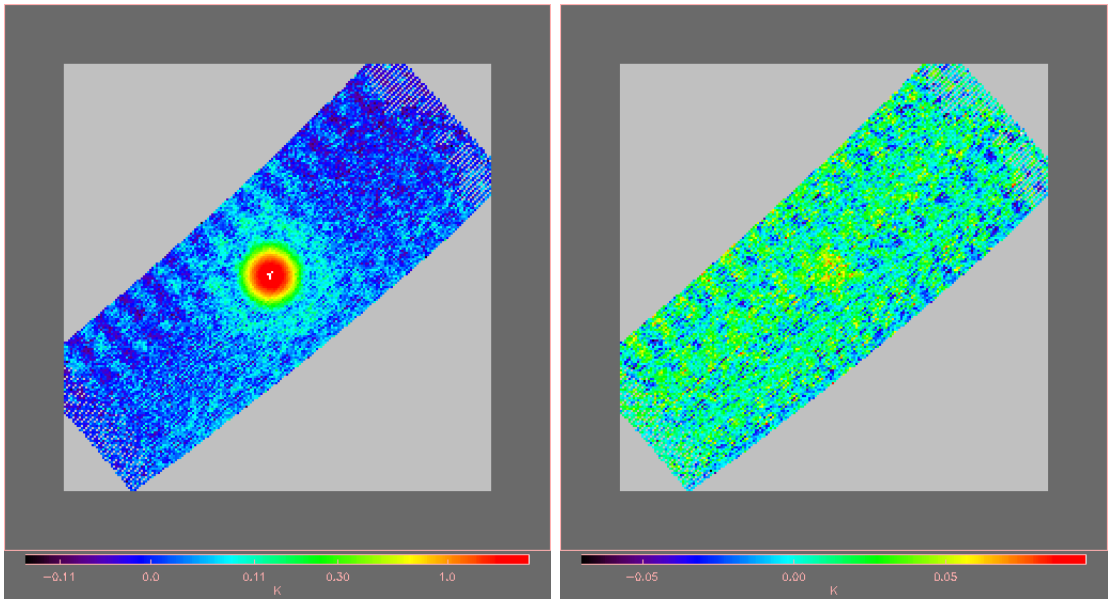

(a) Stokes I (b) Stokes Q

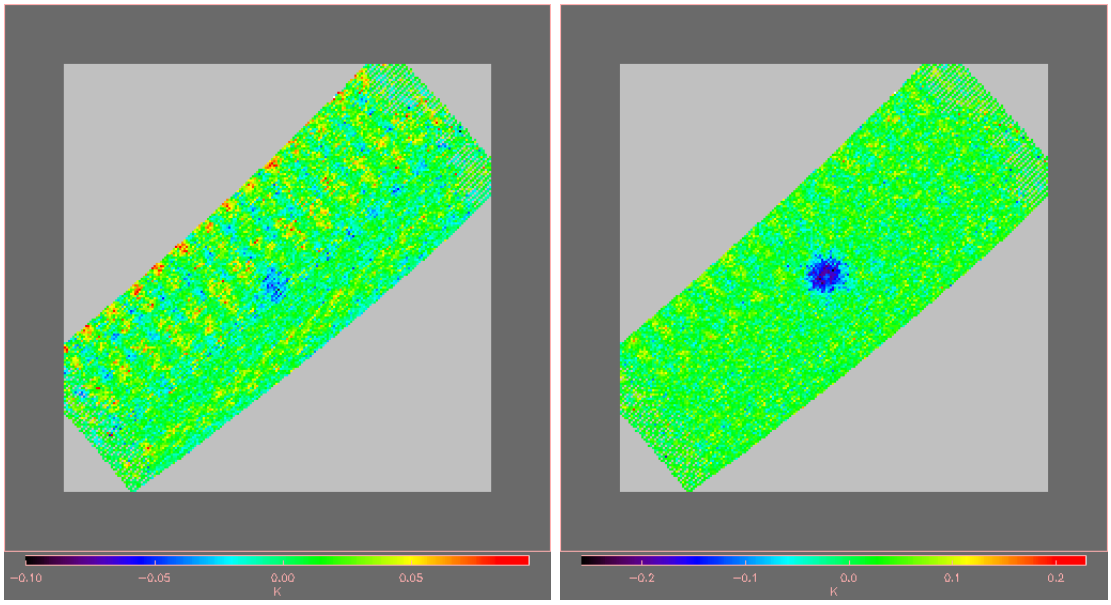

(c) Stokes U (d) Stokes V

Figure 4.14: Maps of Orion at 5 GHz in antenna temperature (K) for intensity I (top-left), Q polarization (top-right), U polarization (bottom-left) and V polarization (bottom-right) binned into 3 arcmin pixels for scan 17. The numerical scale of the colour table is in range [-0.11,1.0] for Stokes I, [-0.05,0.05] for Stokes Q, [-0.10,0.05] for Stokes U and [-0.2,0.2] for Stokes V respectively.

Chapter 5

Data analysis

There are various methods in practice used to measure the brightness of astronomical objects. Section 5.1 will discuss these methods briefly and Section 5.2 will describe the method I used to calculate the flux in Stokes parameters I, Q, U and V. This will also help determine the polarized intensity, degree of polarization, position angle and the polarization leakage of the sources under study. Section 5.3 deals with parallactic angle correction and Section 5.4 is for Tau A and Orion analysis.

5.1 Methods for calculating flux

5.1.1 Aperture photometry

Aperture photometry is a basic technique for measuring the brightness of an astronomical object. In order to calculate the intensity of the source, we need to sum the values of the pixels in a circular area centred on the source (the aperture) and then subtract background contribution. The background contribution can be calculated by adding the pixel values inside a ring-shaped region (annulus), defined around the aperture. (Da Costa, 1992)

The aim of aperture photometry is to measure the brightness of an object without including contributions from contaminating sources. However, estimating the contribution in this background is not always straightforward.

5.1.2 Gaussian fitting

For baseline removed data, the flux can be determined by fitting a Gaussian to the residuals of the baseline fit. Since the telescope beams are approximately Gaussian only between about the beam's half power points, using data outside the half power points will introduce systematic errors to the calculated source fluxes and estimated beam widths. However, during fitting, the data points can be restricted to those between the half power points. An initial guess for the Gaussian half width, centre and height could be set. If the width of the telescope beam is well known then the half-width of the Gaussian can also be held constant.

5.1.3 Template fitting

Gaussian fitting is flawed because the beams are sometimes not symmetric and Gaussian fitting can only be performed over the data collected between the half-power points of the beam. Template fitting is one way to avoid the flaws, for it tries to fit a physical model to the data instead of arbitrary functions. If one has sufficient knowledge of the telescope, or if one has the optics model for the telescope beam, then the beam of the telescope can be determined a priori. An observer can even average a large number of observations to produce a high signal-to-noise representation of the telescope beam (Maddalena, 2002).

If the template fitting is an adequate representation of the data, the results of a template fit will have fewer systematic problems. The results will be more accurate than Gaussian fitting since all of the data will be used in the fit. Fig. 5.1 shows a comparison of Gaussian fitting to template fitting.

5.2 Gaussian fitting on the data

Although this method is not very accurate, I chose this method to measure the flux as systematic error in doing a Gaussian fit should be the same fraction for I, Q, U and V, so will not affect the derived value of fractional polarization or the position

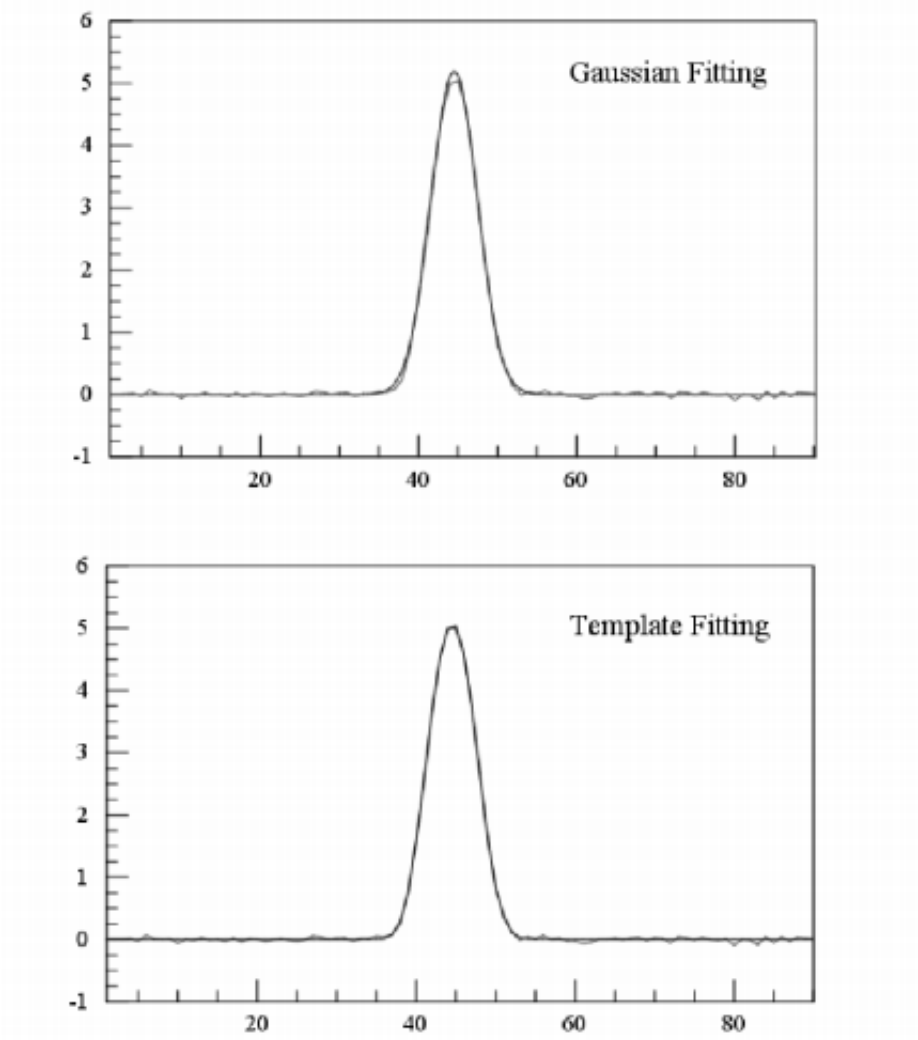

Figure 5.1: Comparison of Gaussian fitting (top) to template fitting (bottom). Gaussian fitting underestimates the intensity of the source and does not fit well the wings to the profile. Template fitting is across all of the data, not just between the half-power points (Image taken from Maddalena (2002)).

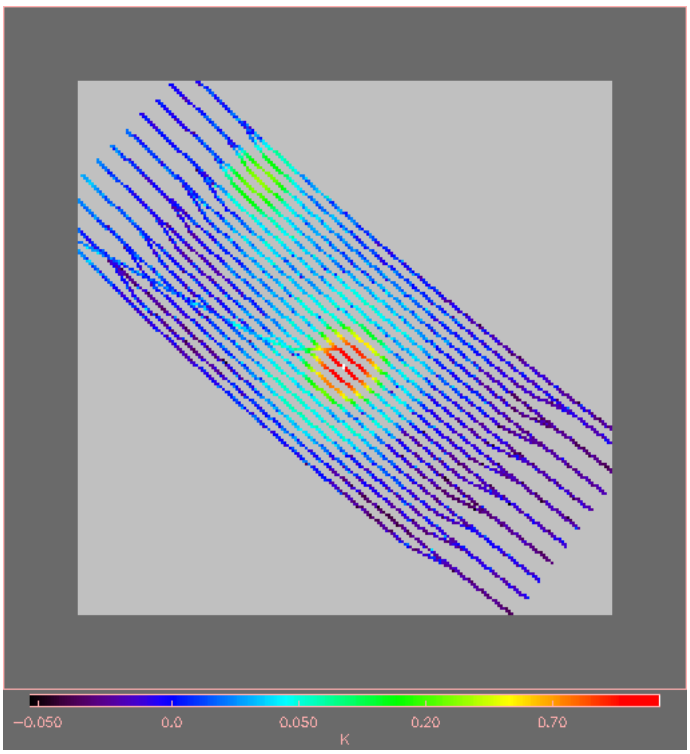

Figure 5.2: A streaky map of Tau A, binned into 3 arcmin pixels in antenna temperature (K), for 13th Nov 2012 data because the observations did a quick zig-zag across the source, rather than a full raster with pointing at every sky pixel. The numerical scale of the colour table is in range [-0.050,0.70].

angle.

When the maps of different raster scans were made, I noticed that the maps can be full of null values. An example of such a map is shown in Fig. 5.2. This map is streaky just because the observations did a quick zig-zag across the source, rather than a full raster with pointing at every sky pixel. Such a map could not be fit since the Gaussian fitting function does not know to omit "missing" sky pixels. Hence, before fitting a Gaussian to the data, I first found the NaNs in the map and set them to zero. I then used the Gaussian fitting method to fit a 2-D Gaussian distribution to the selected data in the baseline removed maps. The volume under the best fit model is approximately equal to the integrated flux density of the source.

In this method I used the IDL function 'GAUSS2DFIT', which fits a two-dimensional, elliptical Gaussian equation to rectilinearly gridded data. Given a set of gridded data, $Z = F(x, y)$, where:

$$F(x,y) = A_0 + A_1 e^{-U/2} \ , \tag{5.1}$$

and the elliptical function is:

$$U = (x'/a^2) + (y'/b)^2 \ , \tag{5.2}$$

the rotated coordinate system is defined as:

$$x' = (x-h)\cos(T) - (y-k)\sin(T) \ , \tag{5.3}$$

$$y' = (x-h)\sin(T) + (y-k)\cos(T) \ . \tag{5.4}$$

The parameters of the ellipse U are: the axis lengths are 2a and 2b, in the unrotated X and Y axes respectively, centre is at (h,k), and rotation of T radians from the X axis, in the clockwise direction. The rotation is optional, and can be forced to 0, making the major and minor axes of the ellipse parallel to the X and Y axes.

The coefficients of the function are returned in a seven element vector A in which:

A[0] = A_0 = constant term

A[1] = A_1 = scale factor

A[2] = a = width of Gaussian in the X direction

A[3] = b = width of Gaussian in the Y direction

A[4] = h = centre X location

A[5] = k = centre Y location.

A[6] = T = the rotation of the ellipse from the X axis in radians, counter-clockwise.

The GAUSS2DFIT function also has a set of keywords like 'MASK', 'TILT' etc and I used the following keywords in my code:

1. MASK: I set the keyword MASK in the GAUSS2DFIT function to a 2-D array

with $[200, 200]$ elements, containing a 1 for each good data point, and a 0 for each missing data point. Bad data points in the map were found using the 'FINITE' function, which identifies whether or not a given argument is finite, and these bad data points were set to 0. Similarly, good data points were found and set to 1.

2. NEGATIVE: This keyword was set to indicate that the Gaussian to be fitted might be a valley. By default, a peak is fit.

3. TILT: This keyword is used to allow the orientation of the major and minor axes of the ellipse to be unrestricted. The default is that the axes of the ellipse must be parallel to the X and Y axes. Therefore, in the default case, A[6] is always returned as 0.

4. FITA: This keyword was set to a vector with the same number of elements as A. The vector contained a zero for each fixed parameter and non-zero values for the elements of A to fit.

I then defined the initial guess for the model to be fitted for each Stokes parameter as follows:

- A[0] : This was set to zero.

- A[1] : This element was used to set the initial guess for I, Q, U, V peak brightness temperature value. Since the map centre is defined as the catalogued position of the source, we expected the peak pixel to be at or near the centre (allowing for noise and residual pointing errors). The centre of the map was calculated from the astrometry structure element crpix[0] and crpix[1], which contains the reference X and Y pixels of the centre of the map. The value at these reference pixels was set as A[1] — the peak brightness temperature value of the Stokes parameters. However, this method did not yield accurate results. Hence, the IDL routine 'MAX' was used, which returns both the maximum value in the map array and its pixel index. From this pixel

index, the corresponding X and Y pixel values were calculated and used as the new map centre pixels. The value at these pixels for the map was then set to A[1].

- A[2] and A[3]: These elements were used to set the widths of the Gaussian in X and Y direction. The FWHM of a Gaussian is calculated by:

$$\mathrm{FWHM} = 2\sqrt{2\ln 2} \times \sigma \ , \tag{5.5}$$

where σ is the standard deviation of the Gaussian. For C-BASS the FWHM is 48 arcminutes, therefore, from Eq. 5.5, $\sigma = 0.339°$.

- A[4] and A[5]: These are the RA and Dec values corresponding to each pixel in the map. To calculate the RA and Dec, first naxis[1] and naxis[2] were retrieved from the astrometry structure, which are the number of pixels in the map, essentially an array of $[200, 200]$ elements. Each element was then subtracted from the centre reference pixel in X value (for RA) and Y value (for Dec). To get the RA and Dec in degrees, it was a simple matter of multiplying the result with astrom.cdelt[0] (for RA) and astrom.cdelt[1] (for Dec), which is nothing but the number of degrees per pixel. This returns a two dimensional array of $[200, 200]$ for RA and Dec each. The RA and Dec values from these arrays that correspond to the maximum pixel value in the map are A[4] and A[5].

- A[6]: This was used to set the rotation of the ellipse to zero.

With the initial model defined, I used the GAUSS2DFIT function to return the coefficients of the fitted function. However, the widths were coming out to be negative because there was very little Q and U in the scans, so the fit would fail to converge. I resolved this by turning off the width fitting and keeping the widths fixed at the value for Stokes I for the other parameters for each scan. Similarly, I turned off the RA and Dec fitting and kept the values fixed at the value for Stokes

I for the other parameters for each scan. Therefore, for each scan of Stokes Q, U and V, the vector FITA contained a zero for second, third, fourth, fifth and sixth elements, which is the width in X direction, width in Y direction, RA, Dec and the tilt respectively. The fitted coefficients returned by GAUSS2DFIT function can be found in Appendix B in Table B.1−Table B.4 for Tau A and in Table B.5−Table B.7 for Orion. The Gaussian fitting code that I wrote can also be found in Appendix A.

5.3 Parallactic angle correction

The Stokes Q and U peak intensity brightness values obtained after Gaussian fitting were not corrected for parallactic angle or leakage, i.e., these are the raw instrumental polarizations. Since the Stokes parameters of linear polarization are orientation dependent, and they are measured in the instrument reference frame, defined by the feed orientation, they need to be converted to a common reference frame, the International Astronomical Union (IAU) coordinate system.

The rotation of the electric field vector from the instrument reference frame to the IAU frame is given by the Jones matrix:

$$\mathrm{R} = \begin{bmatrix} \cos(P) & -\sin(P) \\ \sin(P) & \cos(P) \end{bmatrix}, \tag{5.6}$$

where P is the parallactic angle. The Mueller matrix representation of this rotation, as discussed in Section 1.4.2, is given by Eq. 1.36.

This shows us that rotating the orientation of the feed by 45° will rotate Q into U and U into $-Q$. Stokes I and V are unaffected by rotation of the feed. Hence, the Stokes parameters are rotated everywhere via:

$$\begin{bmatrix} Q' \\ U' \end{bmatrix} = \begin{bmatrix} \cos(2P) & -\sin(2P) \\ \sin(2P) & \cos(2P) \end{bmatrix} \begin{bmatrix} Q \\ U \end{bmatrix}, \tag{5.7}$$

where P, the parallactic angle for an observation of a source at declination δ, at

an hour angle H, from an observatory at latitude Φ, is given by:

$$P = \arctan\left(\frac{\sin H \cos\Phi}{\sin\Phi\cos\delta - \cos\Phi\sin\delta\cos H}\right) . \tag{5.8}$$

To find the parallactic angle for each scan, I first calculated the 'peak time' corresponding to the peak intensity value. I also found the RA and Dec corresponding to the peak intensity. After this, I calculated the julian date (JD), to give the local sidereal time (LST), and hence the hour angle (HA). The JD was simply:

$$\text{JD} = \text{peaktime} + 2400000.5 . \tag{5.9}$$

To calculate the LST, I used the astrolib routine 'CT2LST'. Given, the longitude in degrees (east of Greenwich) of the place for which the local sidereal time is desired and julian date of the time in question, it returns the LST for the date/time specified in hours. I then calculated the hour angle in degrees corresponding to the peak intensity as:

$$\text{hapeak} = \text{lstpeak} \times 15 - \text{RApeak} . \tag{5.10}$$

Once the parameters were set up, the parallactic angle was calculated from Eq. 5.8, for the C-BASS latitude (Φ) = 37.2339°. The new Stokes Q and U were then derived from Eq. 5.7. The corrected Stokes Q and U are given in Table 5.1 for Tau A. After parallactic angle correction, Q should be positive and U should be negative, but as seen from Table 5.1, Q is negative and U is positive. This is because of leakage.

I then plotted the Stokes I, Q, U, V (Stokes Q and Stokes U not corrected for parallactic angle rotation) and polarised intensity (P.I) ($\sqrt{Q^2+U^2}$) as a function of parallactic angle at the mean time of each scan. The plots for Tau A and Orion are as shown in Fig. 5.3 and Fig. 5.4 respectively. For Tau A, the parallactic angle ranges from $\sim -59°$ to $+59°$ and for Orion it ranges from $\sim -40°$ to $+40°$. In the plots, the red pluses are for measured Stokes Q, purple asterisks for measured

Tau A		
Scan No.	Stokes Q Peak Intensity (K)	Stokes U Peak Intensity (K)
0	-0.036	0.103
1	-0.037	0.106
2	-0.037	0.108
3	-0.036	0.105
4	-0.036	0.104
5	-0.038	0.101
6	-0.035	0.094
7	-0.032	0.092
8	-0.025	0.085
9	-0.014	0.088
10	-0.003	0.096
11	-0.011	0.113
12	-0.019	0.121
13	-0.025	0.124
14	-0.025	0.124
15	-0.025	0.124
16	-0.025	0.121
17	-0.027	0.121
18	-0.025	0.120
19	-0.031	0.121
20	-0.031	0.123
21	-0.035	0.109
22	-0.032	0.121

Table 5.1: Stokes Q and U for Tau A (17-Jul-2013 data) after parallactic angle correction from scans $0-22$.

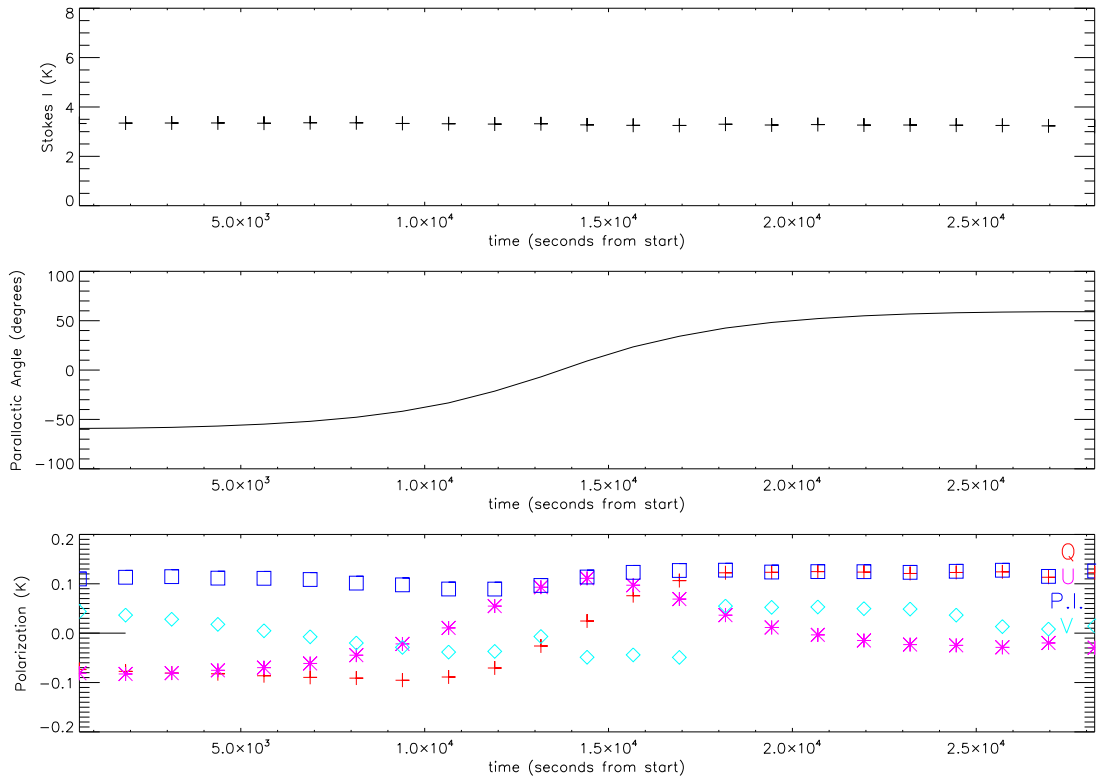

Figure 5.3: Measured Stokes parameters for Tau A as a function of parallactic angle plotted at the mean time for each scan. Stokes I (top), Parallactic Angle (middle) and Stokes Q, U (Stokes Q and U not corrected for parallactic angle rotation), V and polarised intensity (bottom).

Stokes U, cyan diamonds for measured Stokes V and blue squares are for polarised intensity (P.I). In the plot for Tau A (Fig. 5.3), the intensity values look pretty steady but they are varying substantially for Orion (Fig. 5.4). This suggests a drift in the calibrated gain, i.e., the calibration has not worked well. Also, the presence of Stokes Q, U and V in the plot for Orion tells that there is instrumental leakage.

As seen from the plot in Fig. 5.3, Stokes Q and Stokes U both follow nearly sine and cosine waves. It is also seen that the waves are displaced below zero, which reflects coupling of Stokes I into Q and U. The amplitude of the sine/cosine curves gives the linear polarization of the source. Also, the Stokes V values vary significantly; this non-zero value of Stokes V probably results from gain mismatch and this is why observation of several sources is needed to be sure.

After parallactic angle correction, the new Stokes Q and U (from Table 5.1) were

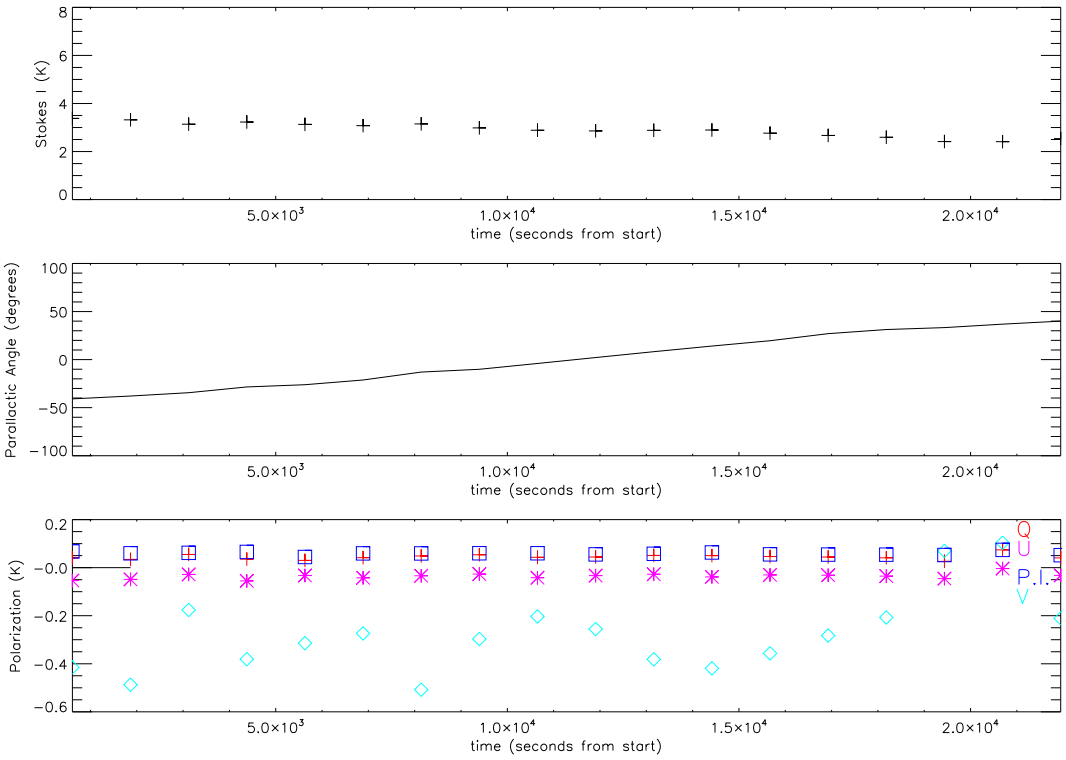

Figure 5.4: Measured Stokes parameters for Orion as a function of parallactic angle plotted at the mean time for each scan. Stokes I (top), Parallactic Angle (middle) and Stokes Q, U, V and polarised intensity (bottom).

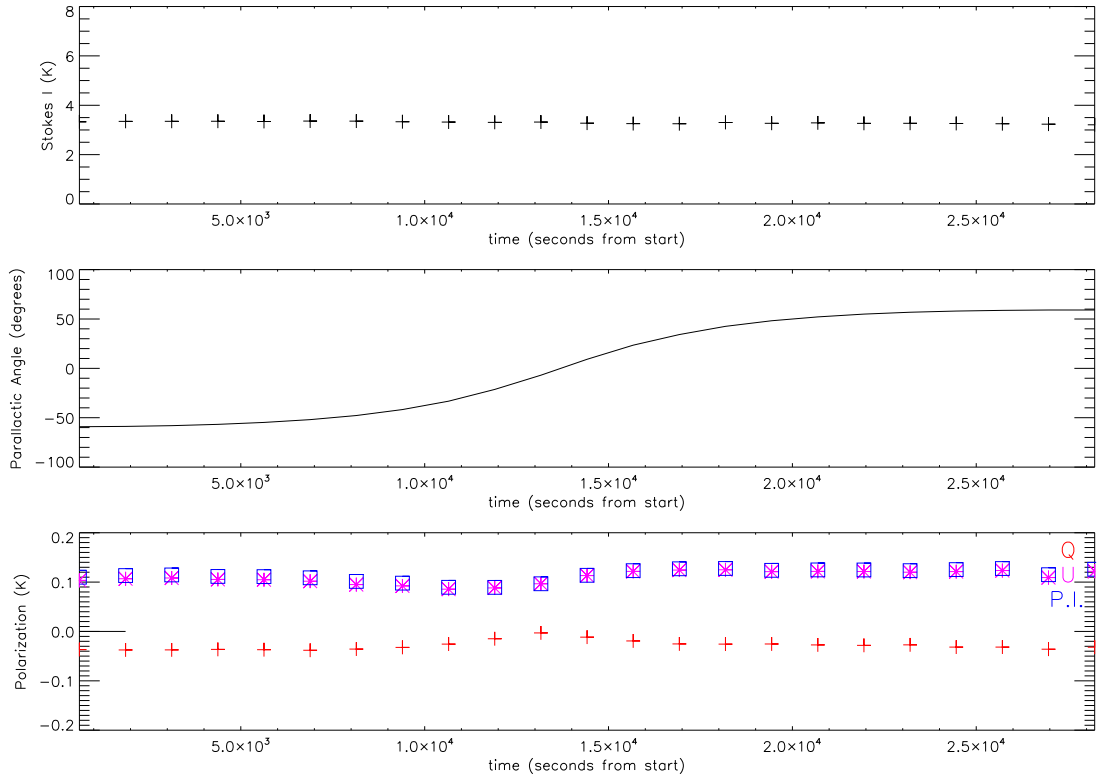

Figure 5.5: Measured Stokes Q and U for Tau A after parallactic angle correction plotted at the mean time for each scan. Stokes I (top), Parallactic Angle (middle) and Stokes Q, U and polarised intensity (bottom).

also plotted at the mean time of each scan and the plot for Tau A is as shown in Fig. 5.5.

5.4 Tau A and Orion analysis

5.4.1 Stacking maps

In Section 4.1 I discussed how the maps of Stokes I, Q, U and V for individual scans were made and Section 5.2 dealt with the Gaussian fitting process on these scans. The next step was to create a map of the whole raster schedule (i.e., all the raster scans combined together). This was necessary because Gaussian fitting on the

stacked map will be most accurate for analyzing the data. To do this, I first created a fits file for each scan using 'MWRFITS' routine. The 'hit_count' and 'header' information was also added to this fits file. Creating the fits file for individual scans was particularly useful in order to share the scans with the collaboration for analysis. Once I had the fits files for all scans, I read in all the fits file one at a time and made a single map for Stokes I, Q, U and V each using:

$$\text{averagemap} = \frac{\sum (\text{map} \times \text{hits})}{\sum \text{hits}} \ . \tag{5.11}$$

5.4.2 Making the maps in beam coordinates

The maps that were made in Section 4.2 were in RA and Dec coordinates. However, in order to determine the leakage, it was necessary to replace the RA and Dec with beam coordinates i.e., long/lat system with the target source at the pole and 0/180 longitude corresponding to the elevation direction. To do this, I used the code 'beamco' written by Dr. Patrick Leahy, which can be found in Appendix A. This code first converts the hour angle and the declination to horizon (alt-az) coordinates using the astrolib routine 'HADEC2ALTAZ'. It then calculates the Az and El offset i.e., the offset from source to pointing. To do this, astrolib routine 'GCIRC' was used, which when given the inputs Az and El of the source and the pointing, calculates the angular distance on the sky between the two. Next, the angle of pointing around the source relative to the direction of zenith is calculated and corrected such that the source is at the pole of the new system. The resulting maps for Orion and Tau A in beam coordinates are as shown in the Fig. 5.6 and Fig. 5.7 respectively. Looking at Tau A maps, the polarization beams are not circular and this could be due to leakage in the optics. Leakage in the receiver should look just like the beam (i.e. a circular Gaussian) in the maps. It is probably the main effect. But we also see a leakage pattern that does not look like the main beam and that has to be due to the optics because the receiver does not know which part of the sky the radiation is coming from. Hence, at least some of the leakage is due to the optics and not the

receiver. Also, in Orion maps, Stokes U is offset i.e., peak is not aligned with I peak and this could also be because of leakage.

When I calculated the polarization angles from scan to scan, they were not the same, this is because Tau A is polarized, so its true polarization rotates with parallactic angle as previously described. So if I stack the maps without correcting for the parallactic angle rotation, the Q and U each have changed sign through the run and largely cancel, therefore, the polarization degree is very low. Hence, I had to correct the maps for parallactic angle rotation (only for Tau A and not Orion), using the method described in Section 5.3 before stacking and the corrected maps are shown in Fig. 5.7.

5.4.3 Leakage correction

Once the maps in beam coordinates were made, I used my Gaussian fitting code on stacked Tau A and Orion maps to determine the leakage. The fitted coefficients are shown in Table 5.2 and Table 5.3 for Orion and Tau A respectively.

Orion				
Stokes	Constant Term	Peak Intensity (K)	X Width (Deg)	Y Width (Deg)
I	0.0184	2.870	0.320	0.326
Q	0.0094	0.0436	0.320	0.326
U	0.0098	-0.0357	0.320	0.326
V	0.0161	-0.2784	0.320	0.326

Table 5.2: Fitted coefficients for Orion (28-Apr-2013 data).

Tau A				
Stokes	Constant Term	Peak Intensity (K)	X Width (Deg)	Y Width (Deg)
I	0.0026	3.0466	0.314	0.344
Q	-0.0014	-0.0206	0.314	0.344
U	0.0015	0.0807	0.314	0.344
V	0.0052	-0.0004	0.314	0.344

Table 5.3: Fitted coefficients for Tau A (17-Jul-2013 data) after parallactic angle correction.

As seen from the Orion maps in Fig. 5.6 and also from Table 5.2, the Q map

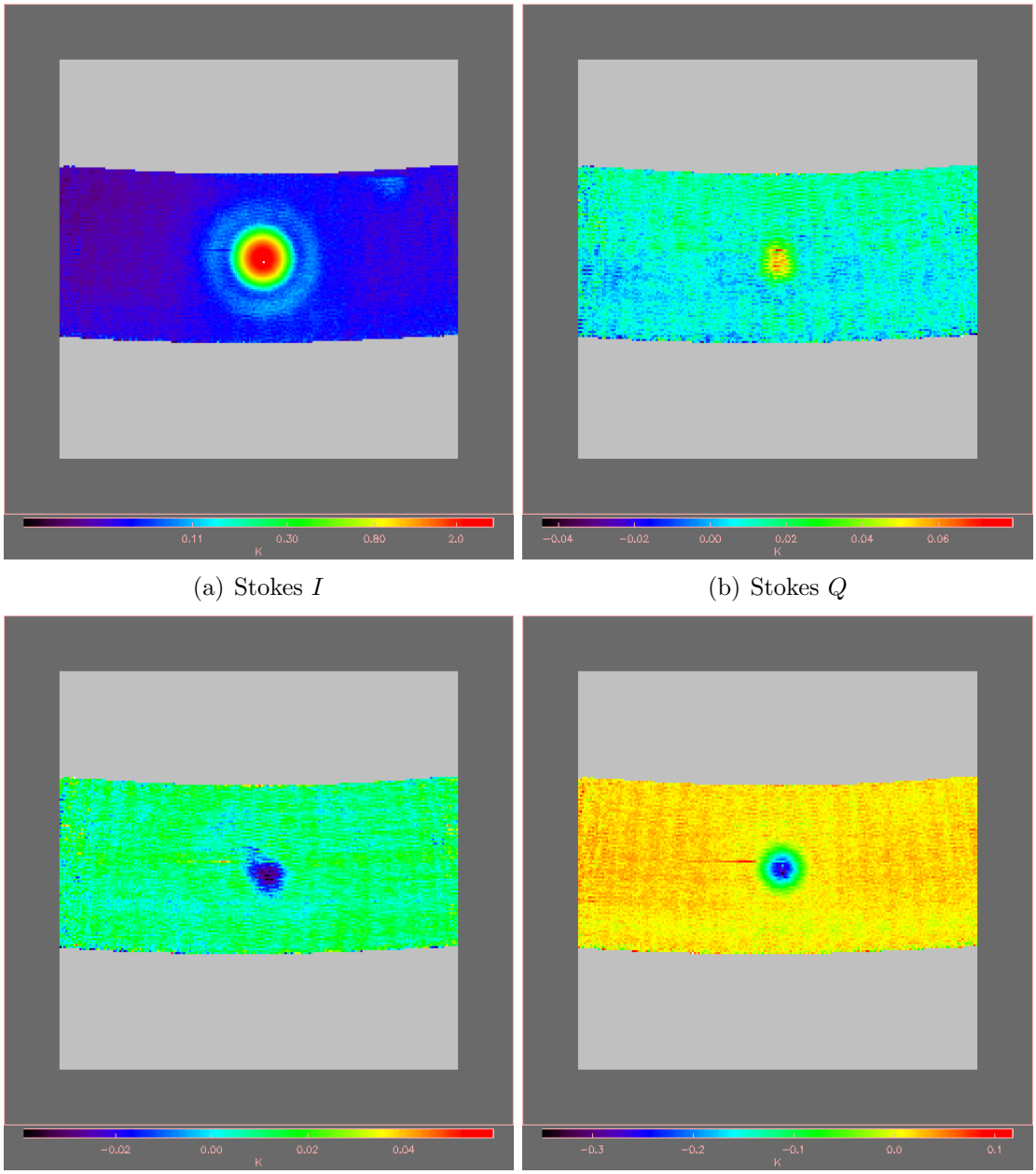

(a) Stokes I (b) Stokes Q

(c) Stokes U (d) Stokes V

Figure 5.6: Maps of Orion at 5 GHz in beam coordinates in antenna temperature (K) binned into 3 arcmin pixels for intensity I (top-left), Q polarization (top-right), U polarization (bottom-left) and V polarization (bottom-right). Stokes U is offset i.e., the peak is not aligned with I peak. The numerical scale of the colour table is in range [0.11,2.0] for Stokes I, [-0.04,0.06] for Stokes Q, [-0.02,0.04] for Stokes U and [-0.3,0.1] for Stokes V respectively.

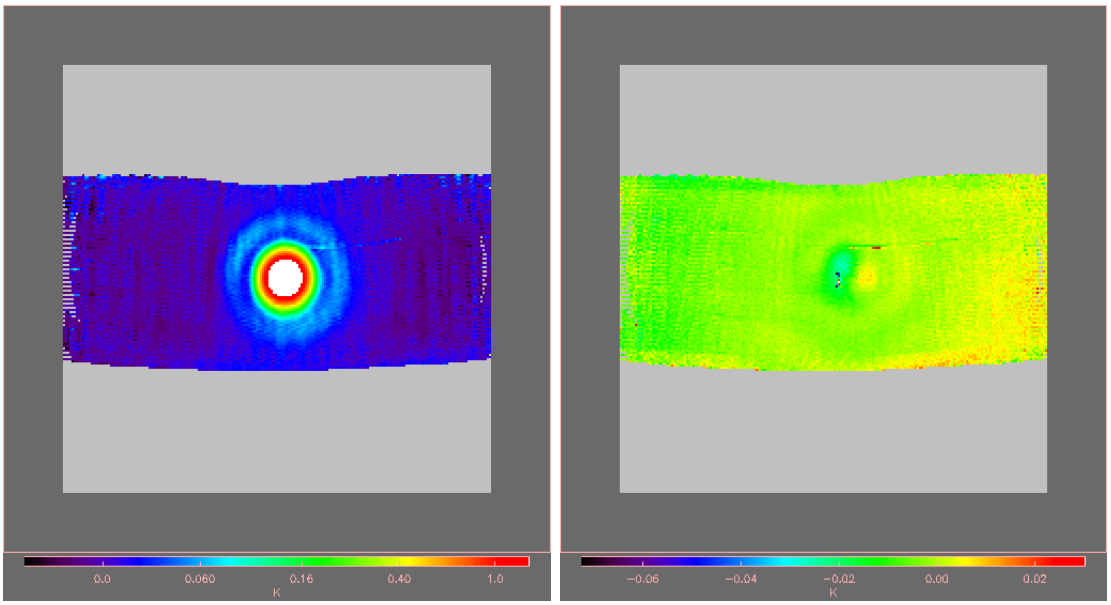

(a) Stokes I (b) Stokes Q

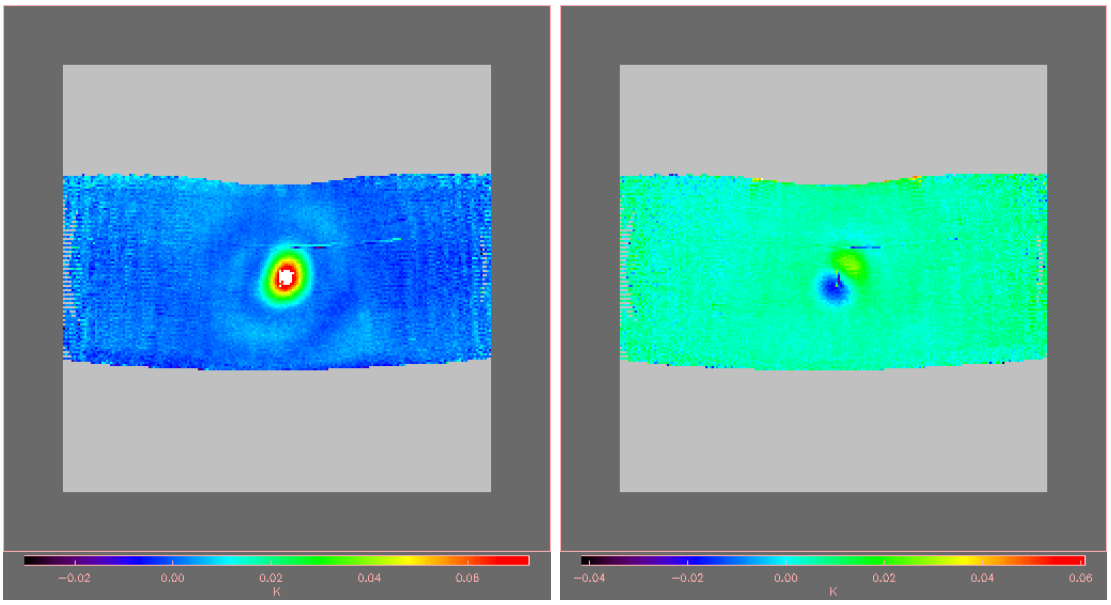

(c) Stokes U (d) Stokes V

Figure 5.7: Maps of Tau A at 5 GHz (corrected for parallactic angle rotation) in beam coordinates in antenna temperature (K) binned into 3 arcmin pixels for intensity I (top-left), Q polarization (top-right), U polarization (bottom-left) and V polarization (bottom-right). The polarization beams are not circular and this could be due to leakage. The numerical scale of the colour table is in range [0.0,1.0] for Stokes I, [-0.06,0.02] for Stokes Q, [-0.02,0.06] for Stokes U and [-0.04,0.06] for Stokes V respectively.

is showing a positive value 0.0436 K (1.49% of I), while U map and is showing a negative value -0.0357 K (-1.22% of I).

Once the polarization leakage was determined, the next step was to implement a correction for this leakage. As seen in Section 1.4.2, the measured Stokes parameters are related to the Stokes parameters S_0 of the incoming signal by Eq. 1.35. The 4×4 Mueller matrix characterizing the total effect of the polarimeter and the parallactic angle can be written as:

$$M = \begin{bmatrix} m_{II} & m_{IQ} & m_{IU} & m_{IV} \\ m_{QI} & m_{QQ} & m_{QU} & m_{QV} \\ m_{UI} & m_{UQ} & m_{UU} & m_{UV} \\ m_{VI} & m_{VQ} & m_{VU} & m_{VV} \end{bmatrix} . \tag{5.12}$$

Eq. 1.35 can then also be represented as,

$$\begin{bmatrix} I_m \\ Q_m \\ U_m \\ V_m \end{bmatrix} = \begin{bmatrix} m_{II} & m_{IQ} & m_{IU} & m_{IV} \\ m_{QI} & \cos(2P) & \sin(2P) & m_{QV} \\ m_{UI} & -\sin(2P) & \cos(2P) & m_{UV} \\ m_{VI} & m_{VQ} & m_{VU} & m_{VV} \end{bmatrix} \begin{bmatrix} I \\ Q \\ U \\ V \end{bmatrix} , \tag{5.13}$$

where the 2×2 matrix containing $\cos(2P)$ and $\sin(2P)$ terms account for the parallactic angle rotation. Each matrix parameter is the coupling of the two Stokes parameters indicated by its subscripts. Considering only Stokes Q and U, the measured Stokes Q and U for an unpolarized source are:

$$Q_m = m_{QI} I \tag{5.14}$$

and,

$$U_m = m_{UI} I \ , \tag{5.15}$$

where $m_{QI} = Q_{leakage}/I_m$ and $m_{UI} = U_{leakage}/I_m$ are the leakage parameters

derived from Orion. $Q_{leakage} = 0.0436$ K, $U_{leakage} = -0.0357$ K and $I_m = 2.870$ as seen from Table 5.2.

Therefore, the correction for Stokes Q and U can now be applied as:

$$\begin{bmatrix} Q'' \\ U'' \end{bmatrix} = \begin{bmatrix} Q_m \\ U_m \end{bmatrix} - I \begin{bmatrix} m_{QI} \\ m_{UI} \end{bmatrix} \tag{5.16}$$

After applying the correction, I corrected the maps in beam coordinates for parallactic angle rotation (only for Tau A and not Orion), using the method described in Section 5.3. I then made a stacked map of all the raster scans combined (i.e., the whole raster schedule) and used my Gaussian fitting code on the Tau A map to return the fitted coefficients as shown in Table 5.4.

Tau A				
Stokes	Constant Term	Peak Intensity (K)	X Width (Deg)	Y Width (Deg)
I	0.003	3.047	0.314	0.344
Q	-0.001	0.013	0.314	0.344
U	0.002	0.106	0.314	0.344
V	0.005	-0.004	0.314	0.344

Table 5.4: Fitted coefficients for Tau A (17-Jul-2013) after leakage correction.

The total flux density in Jy for Gaussian source and beam shapes is given by (Rohlfs & Wilson, 2009):

$$S = 2.65 \frac{T_{MB}\theta^2}{\lambda^2} \ , \tag{5.17}$$

where S is the total flux density in Jy, λ is the wavelength in centimeters, θ is the beam size (FWHM) (calculated using Eq. 5.5) in arcminutes and T_{MB} is the brightness temperature in Kelvin.

The average peak brightness temperature for Orion as seen from Table 5.2 is 2.870 K and average width was 0.323°. The wavelength for C-BASS is 6 cm (5 GHz). The FWHM from Eq. 5.5 comes out to be 45.60 arcmin. Substituting the numbers in Eq. 5.17, the flux density $S = 439.29$ Jy. The flux density of Orion at 5 GHz is 470 Jy (Goss & Shaver, 1970). Currently, C-BASS calibration is off

by 10% (private discussion with PhD student Melis Irfan). We get the noise diode temperature by measuring the peak of a noise diode event and comparing that to known astronomical calibrators within a few hours of said event. In order to measure the peak temperature of an astronomical calibrator we have to fit a Gaussian to it, previously we had not been fitting particularly robust Gaussians – explicitly their baselines were not taking into account the diffuse Galactic emission in front of the source. This diffuse emission is asymmetrically distributed around/over the source, so if source magnitude = peak − background, one cannot get a good measure of the background because it is changing around the source due to diffuse emission and so the magnitudes would not be very good. The errors because of this diffuse emission interference will range but we chose to put an upper limit of 10% to be conservative – one can see the source magnitude vary over parallactic angle because of this effect (different regions of the Galaxy have different amounts of diffuse emission) and we saw that it was varying by around 5%, so 10% is very conservative just in case. This means that we should be seeing the flux density of Orion equal to 483.21 Jy, which is higher than that quoted by (Goss & Shaver, 1970) by $\sim 3\%$. However, it should be noted from the plot in Fig. 5.4 that the intensity values were indeed unsteady for Orion, which suggested a drift in the calibrated gain.

Next, I calculated the polarized intensity from:

$$I_{pol} = (Q^2 + U^2)^{1/2} \ , \tag{5.18}$$

and the degree of polarization Π from Eq. 1.26. For Orion, the polarized intensity was $I_{pol} = 8.62$ Jy and the degree of polarization was $\Pi = 1.96\%$. Since Orion is an unpolarized source, the degree of polarization should be equal to zero, hence the observed value is instrumental leakage.

Similarly, the average peak brightness temperature for Tau A as seen from Table 5.4 is 3.046 K and average width was 0.329°. The wavelength for C-BASS is 6 cm (5 GHz). The FWHM from Eq. 5.5 comes out to be 46.44 arcmin. Substituting

the numbers in Eq. 5.17, the flux density $S = 483.56$ Jy. The polarized intensity calculated from Eq. 5.18 was found to be $I_{pol} = 16.98$ Jy and the degree of polarization from Eq. 1.26 was $\Pi = 3.51\%$. From Table 5.4 it is seen that Stokes Q and U both are positive. However, it should be noted that the polarization conventions defined by radio astronomers and cosmologists are different. The consequence of this definition discrepancy is a change of sign of U. C-BASS uses cosmologists' definition; so the astronomical position angle given by Eq. 1.27 for Tau A will be $\chi = 138.44°$, allowing for the changed sign of U.

I then used a script 'CalibFluxDen.m', developed by PhD student Melis Irfan, from the pipeline to compute and compare the current flux density of Tau A with the value I calculated. Given the input ν, the central frequency, and the year you want the fluxes for, this script outputs the current flux density in Jy as well as the errors. The references she used for this script are Hafez et al. (2008), Vinyaikin (2007), Aller & Reynolds (1985) and Weiland et al. (2011). This script takes into account the secular decline in the flux of Tau A. The script outputs the flux for Tau A at 5 GHz and for year 2013 as 577.65 ± 0.261 Jy. This script can be found in Appendix A. Once again, considering that the C-BASS calibration is off by 10%, the flux density of Tau A should be equal to 531.91 Jy, this is still off from the value calculated with the script by $\sim 8\%$.

The degree of polarization of the radio radiation of Tau A at a wavelength of 3 GHz (9.6 cm) has been quoted as 3±0.5% by Kuz'min & Udal'Tsov (1959). Aumont et al. (2009) give a mean polarization fraction value of 7.4±0.7% at 90 GHz. Also, Gardner & Davies (1966) report a value of 3.8±0.5% polarization at 11.3 cm, 1.6±0.1% at 21.5 cm and 0.9±0.2% at 31.3 cm. The general tendency for the degree of polarization appears to decrease with increasing wavelengths shown in Fig. 5.8. Since C-BASS is observing at a frequency of 5 GHz, our derived value of degree of polarization $\Pi = 3.51 \pm 0.13\%$ is consistent with this.

The position angle of Tau A was compared with the results of Dr. Patrick Leahy's undergrad student, Joe Heffer, who was mapping the D-config 5-GHz VLA

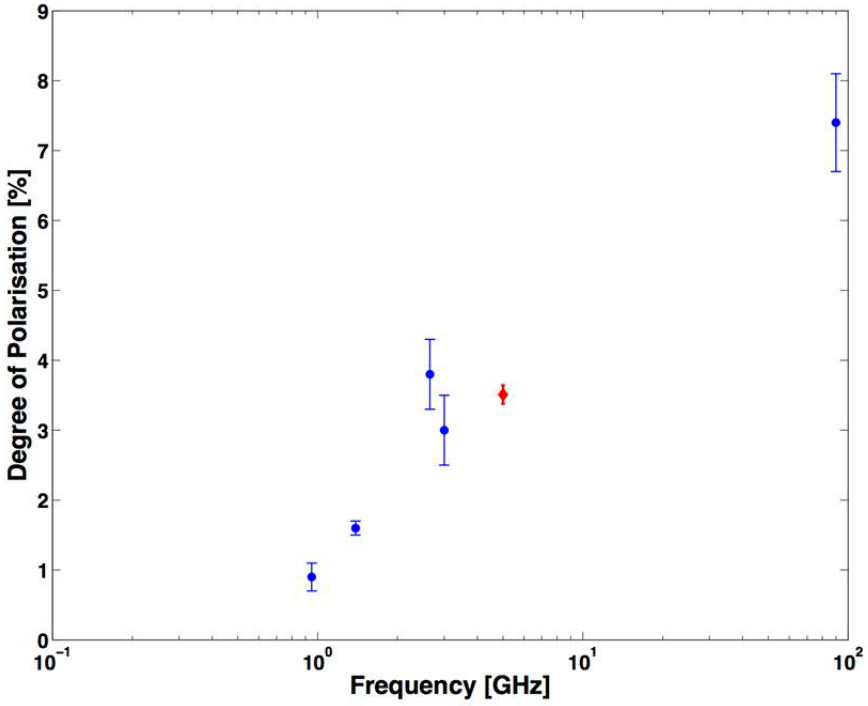

Figure 5.8: A comparison of our derived degree of polarisation of Tau A at 5 GHz with that observed at other frequencies. The general tendency for the degree of polarization appears to decrease with increasing wavelengths. The 0.95 GHz, 1.39 GHz and 2.65 GHz points are from Gardner & Davies (1966). The 3 GHz points are from (Kuz'min & Udal'Tsov, 1959), 5 GHz points are from C-BASS (shown with red diamond) and 90 GHz points are from (Aumont et al., 2009).

data on Tau A. He gets angles of 141.2° at 4885 MHz and 141.1° at 4625 MHz, with an overall systematic error in the calibration of about 0.8°. Kuz'min & Udal'Tsov (1959) quote a position angle of $142° \pm 5°$ at 3 GHz and Gardner (1965) report a position angle of $141° \pm 3°$ at 5 GHz. Our results are consistent with this.

Without going into the detailed analysis, I will present the results of calculations done on raster scans from Table 3.1 and Table 3.2. I also calculated the uncertainty in the data for all the raster scans, with the standard uncertainties and error propagation formulae, and the results are shown in Table 5.5 and 5.6 for Orion and Tau A respectively.

I have previously discussed the calculations and detailed analysis for Orion scan no. 3 from Table 5.5. For scan no. 1, 2, 4 and 5, the data reduction was successful but the calibration was not, resulting in lower flux density values than what is expected at 5 GHz. Also, Orion looks $\approx 2\%$ polarized, which is incorrect.

For Tau A, looking at the results from Table 5.6, detailed analysis and calculations for scan no. 1 were previously discussed. For scan no. 2, 3, 4, 6 and 7, the data plots showed RFI spikes and drifts in intensity values, resulting in higher flux density values. The degree of polarization is very low for what is expected at 5 GHz but the position angles are as expected. The calibration and data reduction for scan no. 5 was successful, producing good quality data, and hence the calculated flux density values and degree of polarization are better compared to the other scans.

Orion				
Scan No.	Scan Date	Flux (Jy)	Polarised Intensity(Jy)	Degree of Polarization (%)
1	16-Jul-2013	366±0.3	7	2±0.2
2	11-Jun-2013	361	7	2±0.2
3	28-Apr-2013	439	9	2±0.2
4	20-Nov-2012	376	8	2±0.3
5	13-Nov-2012	321	9	3±0.2

Table 5.5: Orion raster scans analysis results. For scan no. 1, 2, 4 and 5, the data reduction was successful but the calibration was not, resulting in lower flux density values than what is expected at 5 GHz

Tau A					
Scan No.	Scan Date	Flux (Jy)	Polarised Intensity(Jy)	Degree of Polarization (%)	Position Angle (deg)
1	17-Jul-2013	484	17±0.1	3	138
2	15-Jul-2013	1029	24	2	144±0.7
3	29-Jun-2013	1143	26	2	146±0.5
4	25-Mar-2013	814	20±0.2	2	145±0.5
5	13-Dec-2012	459	17	4±0.1	139±0.6
6	12-Dec-2012	926	20±0.2	2	143±0.6
7	07-Nov-2012	940	16±0.1	2±0.2	146±0.7

Table 5.6: Tau A raster scans analysis results. For scan no. 2, 3, 4, 6 and 7, the data plots showed RFI spikes and drifts in intensity values, resulting in large variation in measured flux density and polarised intensity values.

Chapter 6

Conclusions and future work

6.1 Summary and conclusions

This thesis presents my work done in the polarization calibration of C-BASS. A code has been developed to analyse any raster scan data and is in a state to be used by the collaboration for subsequent analysis.

The principal aim of C-BASS is to allow the subtraction of polarized Galactic synchrotron emission from the data produced by CMB polarization experiments such as *Planck*, *WMAP* and future B-mode polarization experiments, hence it is important that the polarization be measured with utmost accuracy.

It is difficult to measure the Stokes parameters correctly because the degree of polarization in astronomical sources is typically very small and the radioastronomical receiving system modifies the incoming polarization with instrumental effects. Feeds are almost never perfect, so their polarizations are only approximately linear or circular. Also, typically, no feed has two outputs that are perfectly orthogonal. Thus, careful calibration of the polarimeter was a critical step in the development of C-BASS pipeline.

The calibration of a polarimeter is achieved by observations of standard targets such as planets, Tau A, Orion etc, over a range of parallactic angles over a period of some hours with a telescope. A number of Tau A and Orion nebula raster scans

were selected for this purpose. The data were first reduced using the 'reduceData' module from the pipeline. A baseline fit was performed on the reduced data, which removes the baseline from each Stokes parameter, resulting in a data-set that sits on an approximate zero level.

The baseline-removed Stokes parameters were binned into 3 arcmin pixels using a binning code and maps in RA/Dec were made. The FITS files for individual raster scans were also made so the scans could be shared with the collaboration for analysis. A 2-D Gaussian was fitted to each individual I, Q, U and V raster scan and these fit parameters were automatically plotted as part of the analysis, which allowed us to check e.g. the drifts in the calibrated gain.

The Stokes Q and U peak intensity brightness values obtained after Gaussian fitting were also corrected for parallactic angle rotation and plots of Stokes I, Q, U, V and polarised intensity, as a function of parallactic angle, were plotted. The plots for Tau A showed a negative value for Q and a positive value for U, and this was because of the presence of instrumental leakage.

The binned maps of complete raster schedules were made in beam coordinates in order to determine the leakage. For Tau A, the maps were made after correcting for parallactic angle rotation, however, for Orion, they were made without correction as these will likely give the best indication of leakage in the optics. The polarization beams in the maps were not circular and an offset in Stokes Q and U was also observed (i.e., the peaks did not align with Stokes I peak). This was because of leakage in the optics. A 2-D Gaussian was then fitted to Orion maps to determine the leakage parameters.

A leakage correction, using the leakage parameters recovered from Orion, was applied to the Tau A maps and a 2-D Gaussian was again fitted to the maps, which allowed us to calculate the flux density, polarized intensity, degree of polarization, and position angle of the sources under study.

For Orion, the flux density values were generally found to be lower than what is expected at 5 GHz. The degree of polarization was found to be $\approx 2\%$ for all the

raster scans. Orion being an unpolarized source, the degree of polarization should be zero so the observed value is instrumental leakage.

For Tau A, the flux density values were found to be higher or lower than what is expected at 5 GHz, which suggests that more work has to be done on calibration. The raster scan for which this thesis presents a detailed analysis, shows a degree of polarization of $\Pi = 3.51 \pm 0.13\%$. The degree of polarization of Tau A at a wavelength of 3 GHz (9.6 cm) has been quoted as 3±0.5% by Kuz'min & Udal'Tsov (1959). Gardner & Davies (1966) report a value of 3.8±0.5% polarization at 11.3 cm, 1.6±0.1% at 21.5 cm and 0.9±0.2% at 31.3 cm. For C-BASS observing at 5 GHz, our derived value of degree of polarization $\Pi = 3.51 \pm 0.13\%$ is consistent with this. The position angle was found to be $\chi = 138.44^\circ \pm 0.39^\circ$ and this is consistent with the values quoted by Kuz'min & Udal'Tsov (1959) ($142^\circ \pm 5^\circ$) at 3 GHz and Gardner (1965) ($141^\circ \pm 3^\circ$) at 5 GHz.

6.2 Future work

This thesis dealt with single correction i.e, the leakage parameters derived were from a single raster scan of Orion. The next step would be to model leakage over the beam by stacking all the Orion observations. We cannot yet comment on how the derived level of sensitivity achieved with these preliminary polarization measurements will impinge upon the potential limits/measurements of the polarization foregrounds that will be measurable in full C-BASS observations. The data I had was not suitable to answer this because the raster maps were dominated by the 1.2 Hz oscillations for which the collaboration is still trying to find a way to correct.

Future work also involves observing more Orion raster scans as we need to look for variation with time. With an extensive study of Orion observations we can recover the parameters needed to correct for the leakage in optics with improved precision.

Appendix A

Scripts

Baseline Removal

```
;-------------------------------------------------------------------------------------------------------------

; Program Name: baselineRemoval
;
; Version       Date            Author          Description
;=============================================================================================================

;  1.0          12/04/13        Rachana Bhatawdekar             Initial version
;  2.0          02/05/13        Rachana Bhatawdekar             Added map making functionality
;  3.0          23/05/13        Rachana Bhatawdekar             Gaussian fitting
;  4.0          17/06/13        Rachana Bhatawdekar             Parallactic Angle Correction
;  5.0          22/07/13        Rachana Bhatawdekar             Added beam coordinates
    functionality
;  6.0          19/08/13        Rachana Bhatawdekar             Stacked maps and gaussian
    fitting
;  7.0          13/09/13        Rachana Bhatawdekar             Leakage correction
;-------------------------------------------------------------------------------------------------------------

;+
; NAME:
;      baselineRemoval
;
; PURPOSE:
;      Baseline Removal and Gaussian fitting of time ordered data. It also generates maps of
    Stokes parameters, identifies leakage and applies leakage correction to    the data.
;
; CATEGORY:
;
;
; CALLING SEQUENCE:
;
;      baselineRemoval, filename, lon0, lat0
;
;
; INPUTS:
;      filename: absolute path of the filename
;
```

```
;      lon0:      Source position in RA or longitude (degrees)
;      lat0:      Source position in Dec or latitude (degrees)
;
;
; OPTIONAL INPUTS:
;
;
; OPTIONAL KEYWORD PARAMETERS:
;  instrument = if set to 1, makes the maps in beam coordinates.
;
;
; OUTPUTS:
;  Generates maps of Stokes parameters and makes plots of fitted parameters for Stokes I, Q, U
    and V as returned by 2-D Gaussian fitting.
;
; OPTIONAL OUTPUTS:
;      None
;
; COMMON BLOCKS:
;      None
;
; SIDE EFFECTS:
;      None
;
; RESTRICTIONS:
;      None
;
; PROCEDURE:
;      Uses GAUSSIANFIT for gaussian fitting of the data
;      Uses BINMAP for quick binning of time-ordered data
;      Uses BEAMCO for making maps in beam coordinates

FUNCTION BASELINEFIT, data, gap_number, time, scan_number, flag, DOPLOT = doplot


 ; Process the data iteratively to work on every scan of data
  doplot = KEYWORD_SET(doplot)
  junk = ''

  scan = WHERE((scan_number EQ gap_number) AND flag, npts)

  ;creates data structure  of baseline removed data
  scan_data = {time: time[scan], ra: data.ra[scan], dec: data.dec[scan], $
               intensity: fltarr(npts,/NOZERO), Q: FLTARR(npts,/NOZERO), $
               U: FLTARR(npts,/NOZERO), v: FLTARR(npts,/NOZERO), timeMJD:data.mjd[scan]}



  intag = [1,2,3,8,13,14,15]     ; corresponding positions in input dataset

  FOR itag = 3,6 DO BEGIN
     scanned_data = data.(intag[itag])[scan]
     reltime = scan_data.time - MEAN(scan_data.time)  ;get the median value
     medianValue=median(scanned_data)


     low = where(scanned_data lt medianValue) ;get data below median
     clipped = scanned_data[low]
     tclip = reltime[low]
```

```
   coeff = 0
   coeff = poly_fit(tclip,clipped,1,yfit=datafit)  ;Perform polynomial fit
   diff = clipped - datafit

   sd  = stddev(diff)  ;find the standard deviation
   diff = scanned_data - poly(reltime,coeff)
   chi = abs(diff)/sd
   low = where(chi lt 3, nlow)


IF doplot THEN BEGIN
 simple_colour, PS='test.eps'
 PLOT, reltime, scanned_data, $
          yrange = (5*sd*[-1,1])+medianValue, xtitle = 'Time (Seconds)', ytitle = ' Antenna
               Temperature (K)', psym=3
           xyouts, 475, -2.5, '1st deg poly fit', col=1
  OPLOT, tclip, datafit, col=1, thick=8
 device,/close
 set_plot, 'x'
ENDIF


   sdmax = 10.0
   while sdmax ge 5 do begin
      clipped = scanned_data[low]
      tclip = reltime[low]
      errors = replicate(sd,nlow)
      coeff = poly_fit(tclip, clipped, 4, CHISQ=chisq, covar=covar, $
                       measure_errors=errors, yfit=datafit, status=stat)
     IF doplot THEN $
       PRINT, 'sd, chisq, npts, rchisq, status:', $
                sd, chisq, nlow, chisq/(nlow-5), stat
      diff  = clipped - datafit
      sd    = stddev(diff)
      chi   = abs(diff)/sd
      sdmax = max(chi)
    simple_colour, PS='polyfitresults.eps'
      IF DOPLOT THEN OPLOT, tclip, datafit, col=3
     device, /close
    set_plot, 'x'
      low = low[where(chi lt 3, nlow)]

   endwhile

   poly_results=poly(reltime,coeff)

   scan_data.(itag) = scanned_data - poly_results

   IF doplot THEN BEGIN
   simple_colour, PS='test.eps'
PLOT, reltime, scanned_data, $
        yrange = (5*sd*[-1,1])+medianValue, xtitle = 'Time (Seconds)', ytitle = 'Antenna
             Temperature (K)', psym=3
   xyouts, 475, -2.5, '4th deg poly fit', col=1
    OPLOT, reltime, poly_results, col = 1, thick=8
  device,/close
  set_plot, 'x'
    READ, 'Press return for next channel', junk
ENDIF
```

```
  ENDFOR

  RETURN, scan_data

END

FUNCTION GET_PA, time,ra, dec

        cbass_longitude = -118.2822d0
        cbass_latitude  =   37.2339d0


        tel_long = cbass_longitude
        tel_lat  = cbass_latitude

        jd = time + 2400000.5d0 ; data[*,0] is MJD

        lon = ra * 180./!pi
        lat = dec * 180./!pi

        CT2LST, lst, tel_long, dummy, jd ; Astrolib routine
        ha = lst*15d0 - lon ; NB units of HA here are degrees, not hours


    p =  atan(sin(ha*!pi/180)*cos(cbass_latitude*!pi/180)/(cos(lat*!pi/180)*sin(cbass_latitude*!
         pi/180) - cos(cbass_latitude*!pi/180)*sin(lat*!pi/180)*cos(ha*!pi/180)))

RETURN, p


END

PRO baselineRemoval, INSTRUMENT = instrument, map, AVERAGE = average, infile, lat0, lon0

instrument= KEYWORD_SET(instrument)
average = KEYWORD_SET(average)

lq =  0.0151 ; average leakage coefficient for q
lu = -0.0124 ; average leakage coefficient for u


   test = strsplit(infile,'.',/EXTRACT)
  ;Reads fits file and stores output in data variable

IF ~average THEN BEGIN
    read_fits_s,dir+infile,primary_header,data
    read_fits_map, dir+infile, data1, primary_header1, ext1

     data.mjd = data1[*,0]


  ;Reads first column of data and stores in time
   time = (data.mjd - data.mjd[0])*24L*3600L
   scan_number = intarr(N_ELEMENTS(time),/nozero)

  ;To identify individual gaps greater than 1 sec

   gap = where(time[1:*]-time gt 1)
   gaps = n_elements(gap)
```

```
    scan_number[0:gap[0]] = 0

    FOR i = 1, gaps-1 DO scan_number[gap[i-1]+1:gap[i]] = i
    scan_number[gap[gaps-1]+1:*] = gaps

    flag = data.flag gt -1d0

    iValues = fltarr(gaps+1) ; array for plotting I values after gaussian fit
    iXWidth = fltarr(gaps+1) ; array for  average of widths
    iYWidth = fltarr(gaps+1) ; array for average of widths
    paPeakValues = fltarr(gaps+1)
    newQValues = fltarr(gaps+1)
    newUValues = fltarr(gaps+1)

    qValues = iValues & uValues = iValues & vValues = iValues

   timeValues = fltarr(gaps+1) ; time for I, Q, U, V after gaussian fit


   ; Set up parameters for map size & projection

    dlon = 10.0d
    dlat = 10.0d
    dpix = 0.05d

   cbass_longitude = -118.2822d0  ; should get from header.
   cbass_latitude  =   37.2339d0  ; should get from header.

   coord_type = 'C'               ; Equatorial coords (RA/Dec)

    IF instrument THEN BEGIN   ; plot map in beam-centred coordinates
       beamco, cbass_longitude, cbass_latitude,  lon0, lat0, slon0, slat0, data
       coord_type = 'B'           ; non-standard code for beam coords
    ENDIF

ENDIF

    choice = 'y'
    doplot = 0
    READ, PROMPT='Do all [Y/N]: ', choice
    choice = STRMID(STRTRIM(STRUPCASE(choice),1),0,1)
    doall = choice EQ 'Y'
    IF ~doall THEN BEGIN
        choice = 'Y'
        doplot = 1
        prompt = STRING(gaps, FORMAT = $
                        "('Enter a scan number between 0 and ',I3,': ')")

    ENDIF


    spacer = "------------------------------------------------------------"
    beam_sigma = (48./60.)/SQRT(8*ALOG(2.0)) ; C-BASS beam FWHM is 48 arcmin
    tmap = dblarr(200,200,4)
    thits = dblarr(200,200)


    openw, outfile,'output.dat', /get_lun
    openw, outfilepar,'outputpar.dat', /get_lun
    openw, outfileallscan, 'outputallscan.dat', /get_lun
```

```
openw, outfileallscanpar, 'outputallscanpar.dat', /get_lun
printf, outfile, '    a0        a1        a2        a3        a4      a5      a6'
printf, outfilepar, '    a0        a1        a2        a3        a4      a5      a6'
printf, outfileallscan, '    a0        a1        a2        a3        a4      a5      a6'
 printf, outfileallscanpar, '    a0        a1        a2        a3        a4      a5      a6'



i = 0
while (choice EQ 'Y') do begin

    IF ~doall THEN BEGIN
        i = -1
        WHILE (0 gt i OR i gt gaps) DO read, i, PROMPT=prompt

     ENDIF
    aI = [0.0, 1.2, beam_sigma, beam_sigma, 0., 0., 0.0]
    aQ = aI & aU = aI & aV = aI

    numtostring = STRTRIM(i,2)
    outfilename = test[0]+'_'+numtostring+'_map.fits'

IF ~average THEN BEGIN
   ; function call to 'baselinefit' which returns data structure elements
    str_Data = BASELINEFIT(data, i, time, scan_number, flag, DOPLOT = doplot)


    ; calculate PA of centre (max intesnity)
    bingo = where(str_Data.intensity EQ max(str_Data.intensity))
    peakTime = str_Data.timeMJD[bingo]

     RA_peak = str_Data.RA[bingo]
     Dec_peak = str_Data.DEC[bingo]

    cbass_longitude = -118.2822d0 ; should get from header.
    cbass_latitude  =   37.2339d0 ; should get from header.

    pa =  GET_PA(peakTime,RA_peak, Dec_peak)

    jdPeak_hdr = 1D

    jdPeak = peakTime + 2400000.5d0 ; data[*,0] is MJD

    jdPeak_hdr = peakTime[0]


    paPeak = pa*180./!pi

   paPeakValues[i] = paPeak


      binmap, str_Data, coord_type, lon0, lat0, dlon, dlat, dpix, map, $
      channels = ['intensity', 'Q', 'u', 'v']

      hdr = map.hdr
      mapz = [[[map.intensity]], [[map.Q]], [[map.U]], [[map.V]]]

      sxaddpar, hdr, 'CTYPE3', 'STOKES'
      sxaddpar, hdr, 'CDELT3', 1
      sxaddpar, hdr, 'CRVAL3', 1
```

```
          sxaddpar, hdr, 'CRPIX3', 1
          sxaddpar, hdr, 'BUNIT', 'K'
          mwrfits, mapz , outfilename, hdr, /create


         hdr = map.hdr
          sxaddpar, hdr, 'BUNIT', 'count'
          sxaddpar, hdr, 'MJD-AVG', jdPeak_hdr
          sxdelpar, hdr, 'NAXIS3'
          mwrfits, map.hit_count, outfilename, hdr


        extast, map.hdr, astrom, noparams
        IF noparams LT 0 THEN BEGIN
            PRINT, map.hdr
            MESSAGE, 'Bad map header'
        ENDIF

        x0 = ROUND(astrom.crpix[0] - 1)
        y0 = ROUND(astrom.crpix[1] - 1)
        ra  = astrom.cdelt[0]*(findgen(astrom.naxis[0]) - x0)
        dec = astrom.cdelt[1]*(findgen(astrom.naxis[1]) - y0)

    ;gaussian fitting on individual scans
     gaussianfit, mapz, astrom, aI, aQ, aU, aV, ra, dec, outfile

     timeValues[i] = mean(str_Data.time)
     ivalues[i] = aI[1]
     qValues[i] = aQ[1]
     uValues[i] = aU[1]
     vValues[i] = aV[1]

     iXWidth[i] = aI[2]
     iYWidth[i] = aI[3]


      deg2rad = !pi/180.

      newQ = aQ[1]*(cos(2.*paPeak*deg2rad))+ aU[1]*(-sin(2.*paPeak*deg2rad))
      newU = aQ[1]*(sin(2.*paPeak*deg2rad))+aU[1]*(cos(2.*paPeak*deg2rad))


      newQValues[i] = newQ
      newUValues[i] = newU

       printf, outfilepar, spacer
       printf, outfilepar, "Coefficients for newQ is: "
       printf, outfilepar, newQ, FORMAT=format

       printf, outfilepar, spacer
       printf, outfilepar, "Coefficients for newU is: "
       printf, outfilepar, newU, FORMAT=format

       IF doall THEN BEGIN
            IF i EQ 0 THEN BEGIN
               smap = SIZE(map.(2))
               movie = REPLICATE(map,gaps+1)
            ENDIF ELSE movie[i] = map
       ENDIF
ENDIF
```

```
    IF doall Then BEGIN
       newmap = readfits(outfilename)
       IF newmap[0] EQ -1 THEN BREAK
       newhits = readfits(outfilename,head, ex=1)

       time_all = SXPAR(head,'MJD-AVG')
       ra_all = SXPAR(head,'CRVAL1')
       dec_all = SXPAR(head,'CRVAL2')
       ra_all_rad = ra_all * !pi/180.
       dec_all_rad = dec_all * !pi/180.

       good = where(finite(newmap[*,*,0]),complement = bad)
       ;qmap = newmap[*,*,1]
       ;umap = newmap[*,*,2]

      qmap = newmap[*,*,1] - lq*newmap[*,*,0]
      umap = newmap[*,*,2] - lu*newmap[*,*,0]

       par = GET_PA(time_all,ra_all_rad, dec_all_rad)

       FOR ii = 0,3 DO BEGIN
          IF ii EQ 1 THEN temp = qmap*(cos(2.*par)) + umap*(-sin(2.*par)) $
          ELSE IF ii EQ 2 THEN temp = qmap*(sin(2.*par)) + umap*(cos(2.*par)) $
          ELSE temp = newmap[*,*,ii]
          temp[good] *= newhits[good]
          temp[bad] = 0.0
          tmap[*,*,ii] += temp
       ENDFOR
       thits[good] += newhits[good]
    ENDIF

    IF doall THEN BEGIN
       i += 1
       IF N_ELEMENTS(gaps) EQ 1 && i GT gaps THEN choice = 'N'
    ENDIF ELSE BEGIN
        ximview, mapz
        ximview, model, name='model'
       ximview, map.hit_count
       read,choice, PROMPT='Do you want to go for the next scan (y/n):'
       choice = STRMID(STRTRIM(STRUPCASE(choice),1),0,1)
    ENDELSE
 endwhile

FOR ii = 0,3 DO tmap[*,*,ii] /= thits


       mkhdr, head, tmap
        sxaddpar, head, 'CTYPE3', 'STOKES'
        sxaddpar, head, 'CDELT3', 1
        sxaddpar, head, 'CRVAL3', 1
        sxaddpar, head, 'CRPIX3', 1
        sxaddpar, head, 'BUNIT', 'K'


       mwrfits, tmap, 'allscans.fits', head, /create

       nlonall = CEIL(dlon/dpix)
       nlatall = CEIL(dlat/dpix)
```

```
        xrefall = LONG(nlonall/2d0)
        yrefall = LONG(nlatall/2d0)

         crpix = [xrefall, yrefall] + 1
         crval = [lon0, lat0]
         cd = [[-dpix, 0d0], [0d0, dpix]]

       map_str = '-TAN'

      IF instrument THEN BEGIN
      ctype = ['BLON','BLAT']
     ENDIF ELSE BEGIN
     ctype = ['RA--','DEC-']
     ENDELSE

       PUTAST, head, cd, crpix,crval,ctype+map_str,EQUINOX = 2000.0, NAXIS = [nlatall, nlonall],
            CD_TYPE = 1

        extast, head, astro

        x0_all = ROUND(astro.crpix[0] - 1)
        y0_all = ROUND(astro.crpix[1] - 1)
        ra_all  = astro.cdelt[0]*(findgen(astro.naxis[0]) - x0_all)
        dec_all = astro.cdelt[1]*(findgen(astro.naxis[1]) - y0_all)


     ;gaussian fitting on all scans
     iguess = [0.0, 1.2, beam_sigma, beam_sigma, 0., 0., 0.0]
     qguess = iguess &  uguess = iguess &  vguess = iguess



    gaussianfit, tmap, astro, iguess, qguess, uguess, vguess, ra_all, dec_all, outfileallscan

     close, outfile
     close, outfilepar
     close, outfileallscan
     close, outfileallscanpar



  simple_colour, PS='results.eps'
  plot,  timeValues, iValues, /nodata,yrange = [-2, +6], XTITLE='Time (sec)', YTITLE='Peak
       Brightness Temperature (K)' ; for TauA
  oplot, timeValues, iValues, col=1, psym=1
  xyouts, 2.8*10^4 ,5.5, 'I', col=1
  oplot, timeValues, qValues, col=2, psym=2
  xyouts, 2.8*10^4, 5, 'Q', col=2
  oplot, timeValues, uValues, col=3, psym=4
  xyouts, 2.8*10^4, 4.5, 'U', col=3
  oplot, timeValues, vValues, col=4, psym=6
  xyouts, 2.8*10^4 ,4 , 'V', col=4
 device,/close
 set_plot,'x'


;; setting up plotting enviroment ;;
!P.Multi = [0,1,3]
!X.Charsize =1.3
!Y.Charsize=1.3
```

```
simple_colour, PS='stokes.eps'
plot,timevalues, iValues, ytitle = 'Stokes I (K)',yrange=[0,7], xstyle=1,xtitle = 'time (seconds
     from start)'
plot, timevalues, paPeakValues, xstyle=1, yrange=[-90, 90], ytitle='Parallactic Angle (degrees)
    ',xtitle = 'time (seconds from start)'
plot, timevalues, [0,0], xstyle=1, yrange=[-0.6,0.2],ytitle = 'Polarization (K)',xtitle = 'time
    (seconds from start)'
oplot, timevalues, qValues, col =1
xyouts, timevalues[gaps-2], 0.13, 'Q', col = 1
oplot, timevalues, uValues, col = 2
xyouts, timevalues[gaps-2], 0.05, 'U', col = 2
oplot, timevalues,vValues, col = 4
xyouts, timevalues[gaps-2], -0.15, 'V', col = 4
oplot, timevalues, SQRT(qvalues^2 + uvalues^2), col = 3
xyouts, timevalues[gaps-2], -0.07, 'P.I.', col = 3
device, /close
set_plot, 'x'

!P.Multi = [0,1,3]
simple_colour, PS='corrstokes.eps'
plot,timevalues, iValues, ytitle = 'Stokes I (K)',yrange=[0,7], xstyle=1,xtitle = 'time (seconds
     from start)'
plot, timevalues, paPeakValues, xstyle=1, yrange=[-90, 90], ytitle='Parallactic Angle (degrees)
    ',xtitle = 'time (seconds from start)
plot, timevalues, [0,0], xstyle=1, yrange=[-0.2,0.2],ytitle = 'Polarization (K)',xtitle = 'time
    (seconds from start)'
oplot, timevalues, newQValues, col =1
xyouts, timevalues[gaps-2], 0.15, 'Q', col = 1
oplot, timevalues, newUValues, col = 2
xyouts, timevalues[gaps-2], 0.10, 'U', col = 2
oplot, timevalues, SQRT(newQValues^2 + newUValues^2), col = 3
xyouts, timevalues[gaps-2], 0.05, 'P.I.', col = 3
device, /close
set_plot, 'x'



   IF doall THEN map = movie
   print,'Terminating program! Goodbye!!'

end
```

Binning Map

```
PRO binmap, data, coordsys, lon0, lat0, dlon, dlat, dpix, map_struct, $
  CHANNELS=channels

radeg = 180d0 / !dpi
;
; Get details of data structure:
names = TAG_NAMES(data)
nchan_in = N_ELEMENTS(channels)
IF nchan_in EQ 0 THEN BEGIN
  channels = ['intensity','i','temperature'] ; default
  nchan_in = 1
ENDIF

MATCH, names, STRUPCASE(channels), tags, COUNT = nchan
```

```
IF nchan EQ 0 THEN MESSAGE, 'Requested channel(s) not found'
IF nchan LT nchan_in THEN MESSAGE, /INFORMATIONAL, $
  'Some requested channels not found in data'
PRINT, 'BINMAP: binning the following channels: '+names[tags]

; Get exact dimensions of map (don't assume the sizes are exact
; multiples of the pixel size).
nlon = CEIL(dlon/dpix)
nlat = CEIL(dlat/dpix)
; Set chosen map centre on a pixel, not a pixel border:
xref = LONG(nlon/2d0)
yref = LONG(nlat/2d0)
x_max = (xref+0.5d0)*dpix
y_max = (yref+0.5d0)*dpix
x_min = x_max - nlon*dpix
y_min = y_max - nlat*dpix
map_type = 2 ; TAN = Gnomic projection
map_str = '-TAN'
CASE STRUPCASE(STRTRIM(coordsys,2)) OF
   'C': BEGIN
      ctype = ['RA--','DEC-']
      longs = data.ra
      lats  = data.dec
   END
   'G': BEGIN
      ctype = ['GLON','GLAT']
      IF tag_exist(data,'glon',/QUIET) THEN BEGIN
         longs = data.glon
         lats  = data.glat
      ENDIF ELSE BEGIN
         MESSAGE, /INFORMATIONAL, 'Assuming LON/LAT are Galactic coords'
         longs = data.lon
         lats  = data.lat
      ENDELSE
   END
   'E': BEGIN
       ctype = ['ELON','ELAT']
       IF tag_exist(data,'elon',/QUIET) THEN BEGIN
          longs = data.elon
          lats  = data.elat
       ENDIF ELSE BEGIN
          MESSAGE, /INFORMATIONAL, 'Assuming LON/LAT are Ecliptic coords'
           longs = data.lon
           lats  = data.lat
      ENDELSE
   END
   'B': BEGIN
       ctype = ['BLON','BLAT']
       MESSAGE, /INFORMATIONAL, 'Nominal beam centre is coordinate pole'
       longs = data.ra
       lats  = data.dec
   END
   ELSE: MESSAGE, 'Unknown coordinate system: '+coordsys
ENDCASE

PRINT,  xref, yref, nlon, nlat, FORMAT = $
  "('BINMAP: map centre pixel is',2F7.2,' of ',2I4,   ' pixels')"
PRINT, lon0, lat0, coordsys, FORMAT = $
  "(8X,'at coordinates',2F8.3,', deg. Coord type:',A2)"
```

```
; Make FITS header for the map
MKHDR, hdr, 4, [nlon, nlat, nchan]
crpix = [xref, yref] + 1
crval = [lon0, lat0]
cd = [[-dpix, 0d0], [0d0, dpix]]
PUTAST, hdr, cd, crpix, crval, ctype + map_str, $
  EQUINOX = 2000.0, NAXIS = [nlat, nlon], CD_TYPE = 1
longs *= radeg
lats  *= radeg
ADXY, hdr, longs, lats, pixlon, pixlat

good = WHERE( FINITE(pixlon) AND FINITE(pixlat) AND $
              pixlon GE 0 AND pixlon LT nlon AND $
              pixlat GE 0 AND pixlat LT nlat, ngood)

IF ngood EQ 0 THEN MESSAGE, 'No data points in region covered by map'

pixlon = LONG(pixlon[good])
pixlat = LONG(pixlat[good])
ipx = nlon*pixlat + pixlon

npix = nlon*nlat
map  = FLTARR(npix,nchan)
hits = LONARR(npix)
values = FLTARR(ngood, nchan)
FOR ichan = 0,nchan-1 DO values[*,ichan] = data.(tags[ichan])[good]

BIN_DATA, npix, ipx, values, map, hits
FOR ichan = 0,nchan-1 DO map[*,ichan] /= hits
map  = REFORM(map,nlon,nlat, nchan)
hits = REFORM(hits,nlon,nlat)

com = "map_struct = {HDR: hdr, "
FOR ichan = 0, nchan-1 DO $
  com += STRING(names(tags[ichan]),ichan, FORMAT="(A,': map[*,*,',I3,']',')")
com += "hit_count: hits}"

void = EXECUTE(com)

END
```

Binning Data

```
PRO bin_data, npix, ipx, data, map, hmap

; Fast binning of data

sd = SIZE(data)
sm = SIZE(map)

IF sd[0] NE sm[0] THEN MESSAGE, 'Incompatible dimensions for data and map'
nstream = 1
FOR i=2,sd[0] DO nstream *= sd[i]
hits = HISTOGRAM(ipx, BINSIZE=1L, MIN=-1L, MAX=npix, REVERSE_INDICES=ri)
hmap += hits[1:npix]
hits = 0

offset = npix + 3L
idx = ri[ri[0]:ri[npix+2]-1L]
```

```
id2 = ri[2:npix+1] - offset
id1 = ri[1:npix] - offset
ri = 0

FOR istr=0,nstream-1 DO BEGIN
    wtsum = TOTAL( [0.0, data[idx,istr]], /CUMULATIVE, /DOUBLE)
    map[*,istr] += (wtsum[id2] - wtsum[id1])
END
END
```

Gaussian Fitting

```
PRO gaussianfit, mapz, astrom, aI, aQ, aU, aV, ra, dec, outfile


  fit_par = REPLICATE(1,7)
  fit_par[6] = 0 ; turn off fitting tilt

   format = "(4F9.4,3F7.2)"


      naxis = astrom.naxis

      mask = INTARR(naxis[0:1])
      bad = where(~finite(mapz),complement=good)
      mask[bad[*,*,0]] = 0
      mask[good[*,*,0]] = 1

      mapz[bad] =0.0 ; setting NaNs to zeros

      maxpixI = MAX(mapz[*,*,0],subs,/NAN)
      max_x_I = subs mod astrom.naxis[0]
      max_y_I = subs / astrom.naxis[0]
      PRINT, 'Maximum pixel value:', maxpixI, ' should equal', mapz[max_x_I,max_y_I,0]

      aI[1] = mapz[max_x_I,max_y_I,0]
      aI[4] = ra[max_x_I]
      aI[5] = dec[max_y_I]
      fit_par[2:5] = 1

      resultI = gauss2dfit(mapz[*,*,0],aI,ra,dec,fita=fit_par,MASK = mask, $
                           /NEGATIVE,/tilt)

      model = mapz
      ramap = rebin(ra,naxis[0],naxis[1])
      decmap = rebin(REFORM(dec,1,naxis[1]),naxis[0],naxis[1])
      xdash = ramap - aI[4]
      ydash = decmap - aI[5]
      u = (TEMPORARY(xdash)/aI[2])^2 + (TEMPORARY(ydash)/aI[3])^2
      expu  = EXP(-TEMPORARY(u)/2)
      model[*,*,0] = aI[0] + aI[1]*expu
      printf, outfile, spacer
      printf, outfile, "Coefficients for I is: "
      printf, outfile, aI, FORMAT=format


      fit_par[2:5] = 0
      maxpixQ = MAX(mapz[*,*,1], subs, /NAN)
      max_x_q = subs mod astrom.naxis[0]
```

```
 max_y_q = subs / astrom.naxis[0]
print, 'Maximum pixel value:', maxpixQ, 'should equal', mapz[max_x_q, max_y_q,1]

 aQ[1] = mapz[max_x_I,max_y_I,0]
 aQ[2] = aI[2]
 aQ[3] = aI[3]
 aQ[4] = aI[4]
 aQ[5] = aI[5]

 resultQ = gauss2dfit(mapz[*,*,1],aQ,ra,dec,fita=fit_par, $
                      MASK = mask, /NEGATIVE,/tilt)
 model[*,*,1] = aQ[0] + aQ[1]*expu
 printf, outfile, spacer
  printf, outfile, "Coefficients for Q is: "
  printf, outfile, aQ, FORMAT=format


maxpixU = MAX(mapz[*,*,2], subs, /NAN)
max_x_u = subs mod astrom.naxis[0]
max_y_u = subs / astrom.naxis[0]
print, 'Maximum pixel value:', maxpixU, 'should equal', mapz[max_x_u,max_y_u,2]
 aU[1] = mapz[max_x_I,max_y_I,0]
 aU[2] = aI[2]
 aU[3] = aI[3]
 aU[4] = aI[4]
 aU[5] = aI[5]

 resultU = gauss2dfit(mapz[*,*,2],aU,ra,dec,fita=fit_par, $
                      MASK = mask, /NEGATIVE,/tilt)
 model[*,*,2] = aU[0] + aU[1]*expu
 printf, outfile, spacer
 printf, outfile, "Coefficients for U is: "
 printf, outfile, aU, FORMAT=format


 maxpixV = MAX(mapz[*,*,3], subs, /NAN)
 max_x_v = subs mod astrom.naxis[0]
 max_y_v = subs / astrom.naxis[0]
print, 'Maximum pixel value:', maxpixV, 'should equal to', mapz[max_x_v,max_y_v,3]

 aV[1] = mapz[max_x_I,max_y_I,0]
 aV[2] = aI[2]
 aV[3] = aI[3]
 aV[4] = aI[4]
 aV[5] = aI[5]


 resultV = gauss2dfit(mapz[*,*,3],aV,ra,dec,fita=fit_par, $
                      MASK = mask, /NEGATIVE,/tilt)
  model[*,*,3] = aV[0] + aV[1]*expu
  printf, outfile, spacer
  printf, outfile, "Coefficients for V is: "
  printf, outfile, aV, FORMAT=format

END
```

Beam Coordinates

```
PRO beamco, tel_long, tel_lat, lon0, lat0, slon0, slat0, data
```

```
;
; Replace RA & Dec with beam coordinates: long/lat system with the
; target source at the pole, and 0/180 longitude corresponding to the
; elevation direction.
;
  d2r = !dpi /180d0
  halfpi = !dpi / 2d0

; First find the jd, hence LST, hence hour angle
  jd = data.mjd + 2400000.5d0           ; data[*,0] is MJD
  CT2LST, lst, tel_long, dummy, jd      ; Astrolib routine
  ha = lst*15d0 - lon0          ; NB units of HA here are degrees, not hours
  PRINT, 'HA range:', MINMAX(HA)

; Now get Az & El of source:
  HADEC2ALTAZ, ha, lat0, tel_lat, source_el, source_az ; Astrolib routine

; Az & El offset:
; Calculate offset from source to pointing:
  GCIRC, 2, source_az, source_el, data.az, data.el, rtheta
  rtheta *= d2r / 3600d0        ; returned value is in arcsec

; Calculate angle of pointing around source relative to direction of
; zenith:
;
; z
; |\         sin(delta_az)/sin(rtheta) = sin(angle)/sin(90-data.el)
; s \        sin(angle) = sin(source_az - data.az)*cos(data.el)/sin(rtheta)
;    \       cos(angle) = (cos(90-data.el)
;     \                  - sin(source_el)cos(rtheta))/cos(data.el)sin(rtheta)
;      p
;
  daz = (source_az - data.az)*d2r
  source_el *= d2r
  data_el = data.el*d2r
  cde = cos(data_el)
  phi = atan(sin(daz)*cde,(sin(data_el)-sin(source_el)*cos(rtheta))/cde)
  data.ra = phi
  data.dec = halfpi - rtheta

  slon0 = lon0                  ; Remember actual source coords
  slat0 = lat0
  lon0 =  0.0                   ; Source is at the pole of new system
  lat0 = 90.0

END
```

Calibrator Flux Density Calculation

```
function [CasSNow, TotCasErr, CygSNow, TotCygErr, TauSNow, TotTauErr] = CalibFluxDen(v, year)


%%%%%%%%%%%%%%%%%%%%%%%%%%%% Cas A %%%%%%%%%%%%%%%%%%%%%%%%%%%%%%%%%%%%%%%%%%%%

% the spectral form from WMAP table 17 for epoch 2000

CaslogS = 2.204 - 0.682*log10(v/40) + 0.038*(log10(v/40)).^2;

CasFluxDen = 10.^(CaslogS);
```

```
CasErr = 0.002;

% secular decrease from Hafez as this decrease can be calculated for 5 GHz (eq 8)

CasSecDecPercent_perY = 0.68 - 0.15*log10(v);
CasSecDec_perY = CasSecDecPercent_perY/100;
CasYearsPast = year - 2000;

CasSecDecErr = 0.04/100;

CasSNow = CasFluxDen.*(1- CasSecDec_perY).^CasYearsPast;
TotCasErr = sqrt((CasErr./CasFluxDen).^2 + (CasYearsPast.*CasSecDecErr./(1 - CasSecDec_perY)).^2
    .* CasFluxDen.^2);


%%%%%%%%%%%%%%%%%%%%%%%%%%%% Cyg A %%%%%%%%%%%%%%%%%%%%%%%%%%%%%%%%%%%%%%%%%%%%%%%

% the spectral form from WMAP table 17

CyglogS = 1.482 - 1.200*log10(v/40);

CygFluxDen = 10.^(CyglogS);

CygErr = 0.003;

% WMAP p35 'Significant yearly flux variation is not seen for Cyg A'

CygSNow = CygFluxDen;
TotCygErr = CygErr./CasFluxDen;


%%%%%%%%%%%%%%%%%%%%%%%%%%%% Tau A %%%%%%%%%%%%%%%%%%%%%%%%%%%%%%%%%%%%%%%%%%%%%%%

% the spectral form from Vinyaikin eq 11 for epoch 2010

TaulogS = 3.659 - 0.242*log10(v*1000);

TauFluxDen = 10.^(TaulogS);

TauErr = 0.068;

% secular decrease taken from Aller: BEWARE this decrease is for 8 GHz !!!!

TauSecDecPercent_perY = 0.167;
TauSecDec_perY = TauSecDecPercent_perY/100;
TauYearsPast = year - 2010;

TauSecDecErr = 0.015/100;

TauSNow = TauFluxDen.*(1- TauSecDec_perY).^TauYearsPast;
TotTauErr = sqrt((TauErr./TauFluxDen).^2 + (TauYearsPast.*TauSecDecErr./(1 - TauSecDec_perY)).^2
    .* TauFluxDen.^2);


end
```

Appendix B

Tables

Tau A								
Scan No.	Stokes	Constant Term	Peak Intensity (K)	X Width (Deg)	Y Width (Deg)	RA offset (Deg)	Dec offset (Deg)	Tilt
0	I	0.0117	3.330	0.317	0.316	0.25	-0.02	0.00
0	Q	0.0030	-0.073	0.317	0.316	0.25	-0.02	0.00
0	U	0.0029	-0.081	0.317	0.316	0.25	-0.02	0.00
0	V	0.0053	0.043	0.317	0.316	0.25	-0.02	0.00
1	I	0.0084	3.346	0.318	0.316	0.27	-0.03	0.00
1	Q	0.0028	-0.077	0.318	0.316	0.27	-0.03	0.00
1	U	0.0025	-0.082	0.318	0.316	0.27	-0.03	0.00
1	V	0.0053	0.036	0.318	0.316	0.27	-0.03	0.00
2	I	0.0126	3.349	0.318	0.315	0.27	-0.03	0.00
2	Q	0.0024	-0.080	0.318	0.315	0.27	-0.03	0.00
2	U	0.0024	-0.081	0.318	0.315	0.27	-0.03	0.00
2	V	0.0053	0.028	0.318	0.315	0.27	-0.03	0.00
3	I	0.0126	3.351	0.320	0.315	0.27	-0.02	0.00
3	Q	0.0025	-0.082	0.320	0.315	0.27	-0.02	0.00
3	U	0.0025	-0.075	0.320	0.315	0.27	-0.02	0.00
3	V	0.0053	0.017	0.320	0.315	0.27	-0.02	0.00
4	I	0.0126	3.342	0.320	0.315	0.27	-0.01	0.00
4	Q	0.0023	-0.086	0.320	0.315	0.27	-0.01	0.00
4	U	0.0026	-0.069	0.320	0.315	0.27	-0.01	0.00
4	V	0.0055	0.004	0.320	0.315	0.27	-0.01	0.00
5	I	0.0112	3.358	0.319	0.315	0.27	-0.00	0.00
5	Q	0.0022	-0.089	0.319	0.315	0.27	-0.00	0.00
5	U	0.0030	-0.061	0.319	0.315	0.27	-0.00	0.00
5	V	0.0057	-0.007	0.319	0.315	0.27	-0.00	0.00

Table B.1: Fitted coefficients for Tau A (17-Jul-2013) data from scans 0−5.

Tau A								
Scan No.	Stokes	Constant Term	Peak Intensity (K)	X Width (Deg)	Y Width (Deg)	RA offset (Deg)	Dec offset (Deg)	Tilt
6	I	0.0122	3.358	0.316	0.316	0.26	0.01	0.00
6	Q	0.0019	-0.091	0.316	0.316	0.26	0.01	0.00
6	U	0.0034	-0.044	0.316	0.316	0.26	0.01	0.00
6	V	0.0055	-0.019	0.316	0.316	0.26	0.01	0.00
7	I	0.0107	3.331	0.318	0.313	0.25	0.02	0.00
7	Q	0.0015	-0.095	0.318	0.313	0.25	0.02	0.00
7	U	0.0042	-0.021	0.318	0.313	0.25	0.02	0.00
7	V	0.0056	-0.028	0.318	0.313	0.25	0.02	0.00
8	I	0.0088	3.319	0.314	0.313	0.24	0.04	0.00
8	Q	0.0019	-0.088	0.314	0.313	0.24	0.04	0.00
8	U	0.0038	0.010	0.314	0.313	0.24	0.04	0.00
8	V	0.0054	-0.038	0.314	0.313	0.24	0.04	0.00
9	I	0.0064	3.306	0.313	0.314	0.24	0.05	0.00
9	Q	0.0028	-0.070	0.313	0.314	0.24	0.05	0.00
9	U	0.0033	0.054	0.313	0.314	0.24	0.05	0.00
9	V	0.0057	-0.037	0.313	0.314	0.24	0.05	0.00
10	I	0.0037	3.319	0.310	0.313	0.25	0.06	0.00
10	Q	0.0043	-0.026	0.310	0.313	0.25	0.06	0.00
10	U	0.0027	0.093	0.310	0.313	0.25	0.06	0.00
10	V	0.0056	-0.006	0.310	0.313	0.25	0.06	0.00
11	I	0.0034	3.272	0.310	0.311	0.26	0.04	0.00
11	Q	0.0035	0.024	0.310	0.311	0.26	0.04	0.00
11	U	0.0025	0.111	0.310	0.311	0.26	0.04	0.00
11	V	0.0052	-0.048	0.310	0.311	0.26	0.04	0.00

Table B.2: Fitted coefficients for Tau A (17-Jul-2013 data) from scans 6−11.

Tau A								
Scan No.	Stokes	Constant Term	Peak Intensity (K)	X Width (Deg)	Y Width (Deg)	RA offset (Deg)	Dec offset (Deg)	Tilt
12	I	0.0044	3.256	0.311	0.312	0.27	0.02	0.00
12	Q	0.0028	0.075	0.311	0.312	0.27	0.02	0.00
12	U	0.0027	0.097	0.311	0.312	0.27	0.02	0.00
12	V	0.0052	-0.044	0.311	0.312	0.27	0.02	0.00
13	I	0.0021	3.251	0.310	0.311	0.27	-0.01	0.00
13	Q	0.0027	0.106	0.310	0.311	0.27	-0.01	0.00
13	U	0.0021	0.069	0.310	0.311	0.27	-0.01	0.00
13	V	0.0087	-0.049	0.310	0.311	0.27	-0.01	0.00
14	I	0.0081	3.302	0.313	0.314	0.26	-0.04	0.00
14	Q	0.0029	0.122	0.313	0.314	0.26	-0.04	0.00
14	U	0.0035	0.036	0.313	0.314	0.26	-0.04	0.00
14	V	0.0046	0.054	0.313	0.314	0.26	-0.04	0.00
15	I	0.0090	3.268	0.317	0.315	0.24	-0.06	0.00
15	Q	0.0009	0.123	0.317	0.315	0.24	-0.06	0.00
15	U	0.0001	0.011	0.317	0.315	0.24	-0.06	0.00
15	V	0.0009	0.052	0.317	0.315	0.24	-0.06	0.00
16	I	0.0113	3.286	0.314	0.315	0.23	-0.08	0.00
16	Q	0.0034	0.124	0.314	0.315	0.23	-0.08	0.00
16	U	0.0041	-0.003	0.314	0.315	0.23	-0.08	0.00
16	V	0.0049	0.053	0.314	0.315	0.23	-0.08	0.00
17	I	0.0068	3.267	0.316	0.316	0.21	-0.09	0.00
17	Q	0.0035	0.123	0.316	0.316	0.21	-0.09	0.00
17	U	0.0043	-0.014	0.316	0.316	0.21	-0.09	0.00
17	V	0.0049	0.049	0.316	0.316	0.21	-0.09	0.00

Table B.3: Fitted coefficients for Tau A (17-Jul-2013 data) from scans 12−17.

Tau A								
Scan No.	Stokes	Constant Term	Peak Intensity (K)	X Width (Deg)	Y Width (Deg)	RA offset (Deg)	Dec offset (Deg)	Tilt
18	I	0.0082	3.269	0.315	0.315	0.21	-0.10	0.00
18	Q	0.0036	0.120	0.315	0.315	0.21	-0.10	0.00
18	U	0.0046	-0.023	0.315	0.315	0.21	-0.10	0.00
18	V	0.0055	0.048	0.315	0.315	0.21	-0.10	0.00
19	I	0.0136	3.262	0.312	0.314	0.20	-0.11	0.00
19	Q	0.0041	0.122	0.312	0.314	0.20	-0.11	0.00
19	U	0.0055	-0.024	0.312	0.314	0.20	-0.11	0.00
19	V	0.0052	0.036	0.312	0.314	0.20	-0.11	0.00
20	I	0.0097	3.250	0.317	0.317	0.21	-0.10	0.00
20	Q	0.0036	0.124	0.317	0.317	0.21	-0.10	0.00
20	U	0.0052	-0.028	0.317	0.317	0.21	-0.10	0.00
20	V	0.0047	0.013	0.317	0.317	0.21	-0.10	0.00
21	I	0.0129	3.232	0.315	0.316	0.22	-0.10	0.00
21	Q	0.0034	0.113	0.315	0.316	0.22	-0.10	0.00
21	U	0.0053	-0.019	0.315	0.316	0.22	-0.10	0.00
21	V	0.0052	0.008	0.315	0.316	0.22	-0.10	0.00
22	I	0.0081	3.207	0.316	0.317	0.23	-0.10	0.00
22	Q	0.0033	0.122	0.316	0.317	0.23	-0.10	0.00
22	U	0.0048	-0.029	0.316	0.317	0.23	-0.10	0.00
22	V	0.0054	0.014	0.316	0.317	0.23	-0.10	0.00

Table B.4: Fitted coefficients for Tau A (17-Jul-2013 data) from scans 18−22.

Orion								
Scan No.	Stokes	Constant Term	Peak Intensity (K)	X Width (Deg)	Y Width (Deg)	RA offset (Deg)	Dec offset (Deg)	Tilt
0	I	0.025	3.379	0.322	0.316	0.08	-0.03	0.00
0	Q	0.012	0.041	0.322	0.316	0.08	-0.03	0.00
0	U	0.009	-0.053	0.322	0.316	0.08	-0.03	0.00
0	V	0.019	-0.415	0.322	0.316	0.08	-0.03	0.00
1	I	0.024	3.318	0.323	0.317	0.10	-0.04	0.00
1	Q	0.011	0.034	0.323	0.317	0.10	-0.04	0.00
1	U	0.011	-0.048	0.323	0.317	0.10	-0.04	0.00
1	V	0.013	-0.487	0.323	0.317	0.10	-0.04	0.00
2	I	0.026	3.316	0.321	0.314	0.11	-0.03	0.00
2	Q	0.009	0.054	0.321	0.314	0.11	-0.03	0.00
2	U	0.008	-0.028	0.321	0.314	0.11	-0.03	0.00
2	V	0.012	-0.175	0.321	0.314	0.11	-0.03	0.00
3	I	0.023	3.228	0.323	0.315	0.12	-0.03	0.00
3	Q	0.012	0.035	0.323	0.315	0.12	-0.03	0.00
3	U	0.010	-0.055	0.323	0.315	0.12	-0.03	0.00
3	V	0.019	-0.381	0.323	0.315	0.12	-0.03	0.00
4	I	0.020	3.129	0.320	0.320	0.12	-0.02	0.00
4	Q	0.013	0.030	0.320	0.320	0.12	-0.02	0.00
4	U	0.009	-0.032	0.320	0.320	0.12	-0.02	0.00
4	V	0.016	-0.314	0.320	0.320	0.12	-0.02	0.00
5	I 0.023	3.076	0.325	0.319	0.13	-0.01	0.00	
5	Q	0.011	0.041	0.325	0.319	0.13	-0.01	0.00
5	U	0.010	-0.042	0.325	0.319	0.13	-0.01	0.00
5	V	0.019	-0.273	0.325	0.319	0.13	-0.01	0.00

Table B.5: Fitted coefficients for Orion (28-Apr-2013 data) from scans 0−5.

Orion								
Scan No.	Stokes	Constant Term	Peak Intensity (K)	X Width (Deg)	Y Width (Deg)	RA offset (Deg)	Dec offset (Deg)	Tilt
6	I	0.013	3.151	0.322	0.322	0.13	-0.02	0.00
6	Q	0.009	0.048	0.322	0.322	0.13	-0.02	0.00
6	U	0.008	-0.033	0.322	0.322	0.13	-0.02	0.00
6	V	0.017	-0.507	0.322	0.322	0.13	-0.02	0.00
7	I	0.020	2.985	0.319	0.320	0.14	-0.01	0.00
7	Q	0.006	0.053	0.319	0.320	0.14	-0.01	0.00
7	U	0.010	-0.026	0.319	0.320	0.14	-0.01	0.00
7	V	0.017	-0.296	0.319	0.320	0.14	-0.01	0.00
8	I	0.019	2.885	0.322	0.320	0.14	0.00	0.00
8	Q	0.007	0.043	0.322	0.320	0.14	0.00	0.00
8	U	0.008	-0.041	0.322	0.320	0.14	0.00	0.00
8	V	0.019	-0.203	0.322	0.320	0.14	0.00	0.00
9	I	0.019	2.858	0.319	0.319	0.14	-0.01	0.00
9	Q	0.008	0.044	0.319	0.319	0.14	-0.01	0.00
9	U	0.008	-0.033	0.319	0.319	0.14	-0.01	0.00
9	V	0.018	-0.255	0.319	0.319	0.14	-0.01	0.00
10	I	0.019	2.883	0.319	0.322	0.14	-0.01	0.00
10	Q	0.007	0.050	0.319	0.322	0.14	-0.01	0.00
10	U	0.008	-0.027	0.319	0.322	0.14	-0.01	0.00
10	V	0.012	-0.381	0.319	0.322	0.14	-0.01	0.00
11	I	0.019	2.895	0.320	0.322	0.15	-0.01	0.00
11	Q	0.005	0.050	0.320	0.322	0.15	-0.01	0.00
11	U	0.009	-0.038	0.320	0.322	0.15	-0.01	0.00
11	V	0.011	-0.418	0.320	0.322	0.15	-0.01	0.00

Table B.6: Fitted coefficients for Orion (28-Apr-2013 data) from scans 6−11.

Orion								
Scan No.	Stokes	Constant Term	Peak Intensity (K)	X Width (Deg)	Y Width (Deg)	RA offset (Deg)	Dec offset (Deg)	Tilt
12	I	0.015	2.764	0.321	0.323	0.15	-0.01	0.00
12	Q	0.007	0.046	0.321	0.323	0.15	-0.01	0.00
12	U	0.007	-0.030	0.321	0.323	0.15	-0.01	0.00
12	V	0.011	-0.356	0.321	0.323	0.15	-0.01	0.00
13	I	0.018	2.670	0.317	0.323	0.15	-0.01	0.00
13	Q	0.009	0.044	0.317	0.323	0.15	-0.01	0.00
13	U	0.008	-0.031	0.317	0.323	0.15	-0.01	0.00
13	V	0.016	-0.282	0.317	0.323	0.15	-0.01	0.00
14	I	0.012	2.593	0.318	0.322	0.16	-0.00	0.00
14	Q	0.008	0.041	0.318	0.322	0.16	-0.00	0.00
14	U	0.010	-0.035	0.318	0.322	0.16	-0.00	0.00
14	V	0.016	-0.207	0.318	0.322	0.16	-0.00	0.00
15	I	0.017	2.416	0.319	0.326	0.17	0.00	0.00
15	Q	0.011	0.026	0.319	0.326	0.17	0.00	0.00
15	U	0.014	-0.045	0.319	0.326	0.17	0.00	0.00
15	V	0.015	0.069	0.319	0.326	0.17	0.00	0.00
16	I	0.013	2.410	0.318	0.324	0.17	0.01	0.00
16	Q	0.009	0.073	0.318	0.324	0.17	0.01	0.00
16	U	0.008	-0.003	0.318	0.324	0.17	0.01	0.00
16	V	0.020	0.103	0.318	0.324	0.17	0.01	0.00
17	I	0.017	2.538	0.321	0.324	0.18	0.02	0.00
17	Q	0.007	0.040	0.321	0.324	0.18	0.02	0.00
17	U	0.010	-0.032	0.321	0.324	0.18	0.02	0.00
17	V	0.0184	-0.211	0.321	0.324	0.18	0.02	0.00

Table B.7: Fitted coefficients for Orion (28-Apr-2013 data) from scans 12−17.

Bibliography

A. Benoît, P. Ade, A. Amblard, et al., 2004, A&A, 424, 2, 571

Ali-Haïmoud Y., Hirata C. M., Dickinson C., 2009, MNRAS, 395, 1055

Aller H. D., Reynolds S. P., 1985, ApJ, 293, L73

Aumont J., Conversi L., Thum C., et al., 2009, ApJ, 5–6

Banday A. J., Dickinson C., Davies R. D., Davis R. J., Górski K. M., 2003, MNRAS, 345, 897

Battistelli E. S., Rebolo R., Rubiño-Martín J. A., et al., 2006, ApJ, 645, L141

Baumann D., Jackson M. G., Adshead P., et al., 2009, in American Institute of Physics Conference Series, edited by S. Dodelson, D. Baumann, A. Cooray, J. Dunkley, A. Fraisse, M. G. Jackson, A. Kogut, L. Krauss, M. Zaldarriaga, K. Smith, vol. 1141 of American Institute of Physics Conference Series, 10–120

Bennett C. L., Halpern M., Hinshaw G., et al., 1997, in American Astronomical Society Meeting Abstracts, vol. 29 of Bulletin of the American Astronomical Society, 1353

Bennett C. L., Halpern M., Hinshaw G., et al., 2003a, ApJS, 148, 1

Bennett C. L., Hill R. S., Hinshaw G., et al., 2003b, ApJS, 148, 97

Bennett C. L., Larson D., Weiland J. L., et al., 2012, ApJS, 208, 1

Benoît A., Ade P., Amblard A., et al., 2004, A&A, 424, 571

Bernardi G., Carretti E., Cortiglioni S., Sault R. J., Kesteven M. J., Poppi S., 2003, ApJ, 594, L5

Bernardi G., Carretti E., Sault R. J., Cortiglioni S., Poppi S., 2006, MNRAS, 370, 2064

Bicay M. D., Helou G., Condon J. J., 1989, ApJ, 338, L53

Biermann P. L., Becker J. K., Caceres G., Meli A., Seo E.-S., Stanev T., 2010, ApJ, 710, L53

Bischoff C., Hyatt L., McMahon J. J., et al., 2008, ApJ, 684, 771

Bock J., Church S., Devlin M., et al., 2006, ApJ, 1–87

Born M., Wolf E., 1965, Principles of Optics, Peramon Press, New York

Brown M. L., Ade P., Bock J., et al., 2009, ApJ, 705, 978

Burke, Smith, 2002, An Introduction to Radio Astronomy, Cambridge University Press

Carretti E., Bernardi G., Sault R. J., Cortiglioni S., Poppi S., 2005a, MNRAS, 358, 1

Carretti E., Gaensler B., Staveley-Smith L., et al., 2009, ATNF Proposal, 2265

Carretti E., McConnell D., McClure-Griffiths N. M., Bernardi G., Cortiglioni S., Poppi S., 2005b, MNRAS, 360, L10

Carretti E., Poppi S., Reich W., et al., 2006, MNRAS, 367, 132

Casassus S., Nyman Ring L. A., Pearson T. J., Readhead A. C., 2005, in Planetary Nebulae as Astronomical Tools, edited by R. Szczerba, G. Stasińska, S. K. Gorny, vol. 804 of American Institute of Physics Conference Series, 204–207

Chiang H. C., Ade P. A. R., Barkats D., et al., 2010, ApJ, 711, 1123

Cholis I., Goodenough L., Weiner N., 2009, Phys.Rev.D, 79, 12, 123505

Da Costa G. S., 1992, in Astronomical CCD Observing and Reduction Techniques, edited by S. B. Howell, vol. 23 of Astronomical Society of the Pacific Conference Series, 90

Davies R. D., Watson R. A., Gutierrez C. M., 1996, MNRAS, 278, 925

Davies R. D., Wilkinson A., 1999, in Microwave Foregrounds, edited by A. de Oliveira-Costa & M. Tegmark, vol. 181 of Astronomical Society of the Pacific Conference Series, 77

de Oliveira-Costa A., Kogut A., Devlin M. J., Netterfield C. B., Page L. A., Wollack E. J., 1997, ApJ, 482, L17

de Oliveira-Costa A., Tegmark M., Finkbeiner D. P., et al., 2002, ApJ, 567, 363

de Oliveira-Costa A., Tegmark M., Gutierrez C. M., et al., 1999, ApJ, 527, L9

Dennison B., Simonetti J. H., Topasna G. A., 1998, PASA, 15, 147

Dickinson C., Casassus S., Pineda J. L., Pearson T. J., Readhead A. C. S., Davies R. D., 2006, ApJ, 643, L111

Dickinson C., Davies R. D., Davis R. J., 2003, MNRAS, 341, 369

Dickinson C., Peel M., Vidal M., 2011, MNRAS, 418, L35

Dobler G., Draine B., Finkbeiner D. P., 2009, ApJ, 699, 1374

Dobler G., Finkbeiner D. P., Cholis I., Slatyer T., Weiner N., 2010, ApJ, 717, 825

Draine B. T., Lazarian A., 1998a, ApJ, 494, L19

Draine B. T., Lazarian A., 1998b, ApJ, 508, 157

Draine B. T., Lazarian A., 1999, ApJ, 512, 740

Draine B. T., Li A., 2007, ApJ, 657, 810

Emerson D., 2002, in Single-Dish Radio Astronomy: Techniques and Applications, vol. 278 of Astronomical Society of the Pacific Conference Series, 31–32

Erickson W. C., 1957, ApJ, 126, 480

Finkbeiner D. P., 2003, ApJS, 146, 407

Finkbeiner D. P., 2004, ApJ, 614, 186

Finkbeiner D. P., Davis M., Schlegel D. J., 1999, ApJ, 524, 867

Finkbeiner D. P., Schlegel D. J., Frank C., Heiles C., 2002, ApJ, 566, 898

Fixsen D. J., 2009, ApJ, 707, 916

Fraisse A. A., Brown J.-A. C., Dobler G., et al., 2009, in American Institute of Physics Conference Series, edited by S. Dodelson, D. Baumann, A. Cooray, J. Dunkley, A. Fraisse, M. G. Jackson, A. Kogut, L. Krauss, M. Zaldarriaga, K. Smith, vol. 1141 of American Institute of Physics Conference Series, 265–310

Gardner F. F., 1965, Australian Journal of Physics, 18, 385

Gardner F. F., Davies R. D., 1966, Australian Journal of Physics, 19, 441

Gaustad J. E., McCullough P. R., Rosing W., Van Buren D., 2001, PASP, 113, 1326

Gold B., Bennett C. L., Hill R. S., et al., 2009, ApJS, 180, 265

Gold B., Odegard N., Weiland J. L., et al., 2011, ApJS, 192, 15

Goodenough L., Hooper D., 2009, ApJ, 1–5

Goss W. M., Shaver P. A., 1970, Australian Journal of Physics Astrophysical Supplement, 14, 1

Grainge K., Carreira P., Cleary K., et al., 2003, MNRAS, 341, L23

Hafez Y. A., Davies R. D., Davis R. J., et al., 2008, MNRAS, 388, 1775

Haslam C. G. T., Salter C. J., Stoffel H., Wilson W. E., 1982, A&AS, 47, 1

Heiles C., 2002, in Single-Dish Radio Astronomy: Techniques and Applications, vol. 278 of Astronomical Society of the Pacific Conference Series, 131–152

Hester J. J., 2008, ARA&A, 46, 127

Hu W., White M., 1997, NEWA, 2, 323

Hummer D. G., Storey P. J., 1987, MNRAS, 224, 801

Jonas J. L., Baart E. E., Nicolson G. D., 1998, MNRAS, 297, 977

Kamionkowski M., Kosowsky A., Stebbins A., 1997, Phys.Rev.D, 55, 7368

King O. G., Copley C., Davies R., et al., 2010, in Society of Photo-Optical Instrumentation Engineers (SPIE) Conference Series, vol. 7741 of Society of Photo-Optical Instrumentation Engineers (SPIE) Conference Series

Kogut A., Banday A. J., Bennett C. L., et al., 1996a, ApJ, 464, L5

Kogut A., Banday A. J., Bennett C. L., Gorski K. M., Hinshaw G., Reach W. T., 1996b, ApJ, 460, 1

Komatsu E., Smith K. M., Dunkley J., et al., 2011, ApJS, 192, 18

Kovac J. M., Leitch E. M., Pryke C., Carlstrom J. E., Halverson N. W., Holzapfel W. L., 2002, Nature, 420, 772

Kraus J. D., 1986, Radio Astronomy, McGraw-Hill Book Company

Kuz'min A. D., Udal'Tsov V. A., 1959, Soviet Ast., 3, 39

Larson D., Dunkley J., Hinshaw G., et al., 2011, ApJS, 192, 16

Lawson K. D., Mayer C. J., Osborne J. L., Parkinson M. L., 1987, MNRAS, 225, 307

Leitch E. M., Kovac J. M., Halverson N. W., Carlstrom J. E., Pryke C., Smith M. W. E., 2005, ApJ, 624, 10

Leitch E. M., Readhead A. C. S., Pearson T. J., Myers S. T., 1997, ApJ, 486, L23

Low F. J., Young E., Beintema D. A., et al., 1984, ApJ, 278, L19

Maddalena R. J., 2002, in Single-Dish Radio Astronomy: Techniques and Applications, vol. 278 of Astronomical Society of the Pacific Conference Series, 336–338

Masi S., Ade P. A. R., Bock J. J., et al., 2001, ApJ, 553, L93

Mason B. S., Pearson T. J., Readhead A. C. S., et al., 2003, ApJ, 591, 540

Mennella A., Bersanelli M., Seiffert M., et al., 2003, A&A, 410, 1089

Montroy T. E., Ade P. A. R., Bock J. J., et al., 2006, ApJ, 647, 813

Neugebauer G., Habing H. J., van Duinen R., et al., 1984, ApJ, 278, L1

O'Neil K., 2002, in Single-Dish Radio Astronomy: Techniques and Applications, edited by S. Stanimirovic, D. Altschuler, P. Goldsmith, C. Salter, vol. 278 of Astronomical Society of the Pacific Conference Series, 293–311

Oster L., 1961, Review of Modern Physics, 33, 525

Paradis D., Veneziani M., Noriega-Crespo A., et al., 2010, A&A, 520, L8

Penzias A. A., Wilson R. W., 1965, ApJ, 142, 419

Piacentini F., Ade P. A. R., Bock J. J., et al., 2006, ApJ, 647, 833

Planck Collaboration, Ade P. A. R., Aghanim N., et al., 2011, A&A, 536, A1

Planck Collaboration, Ade P. A. R., Aghanim N., et al., 2013a, ApJ, 1–44

Planck Collaboration, Ade P. A. R., Aghanim N., et al., 2013b, ApJ, 1–67

Ponthieu N., Macías-Pérez J. F., Tristram M., et al., 2005, A&A, 444, 327

QUIET Collaboration, Bischoff C., Brizius A., et al., 2011, ApJ, 741, 111

Rees M. J., 1968, ApJ, 153, L1

Reich P., Reich W., 1986, A&AS, 63, 205

Reich P., Reich W., 1988, A&AS, 74, 7

Reich P., Testori J. C., Reich W., 2001, A&A, 376, 861

Reich W., 1982, A&AS, 48, 219

Reich W., Reich P., 2009, in IAU Symposium, edited by K. G. Strassmeier, A. G. Kosovichev, J. E. Beckman, vol. 259 of IAU Symposium, 603–612

Reynolds R. J., Haffner L. M., Madsen G. J., 2002, in Galaxies: the Third Dimension, edited by M. Rosada, L. Binette, L. Arias, vol. 282 of Astronomical Society of the Pacific Conference Series, 31

Rohlfs K., Wilson T., 2009, Tools Of Radio Astronomy, Springer

Rybicki G., Lightman A., 1979, Radiative processes in astrophysics, WILEY-INTERSCIENCE PUBLICATION, Chichester, UK

Schlegel D. J., Finkbeiner D. P., Davis M., 1998, ApJ, 500, 525

Seiffert M., Mennella A., Burigana C., et al., 2002, A&A, 391, 1185

Sievers J. L., Achermann C., Bond J. R., et al., 2007, ApJ, 660, 976

Smoot G. F., 1997, ApJ, 1–48

Smoot G. F., 1999, ApJ, 1–17

Smoot G. F., Bennett C. L., Kogut A., et al., 1992, ApJ, 396, L1

Spergel D. N., Verde L., Peiris H. V., et al., 2003, ApJS, 148, 175

Stokes G. G., 1851, Transactions of the Cambridge Philosophical Society, 9, 399

Strukov I. A., Skulachev D. P., 1984, Pisma v Astronomicheskii Zhurnal, 10, 3

Sun X. H., Han J. L., Reich W., et al., 2007, A&A, 469, 1003

Sunyaev R. A., Zeldovich I. B., 1980, ARA&A, 18, 537

Sutton D., Johnson B. R., Brown M. L., Cabella P., Ferreira P. G., Smith K. M., 2009, MNRAS, 393, 894

Sutton D., Zuntz J. A., Ferreira P. G., et al., 2010, MNRAS, 407, 1387

Tauber J. A., Mandolesi N., Puget J.-L., et al., 2010, A&A, 520, A1

Tegmark M., de Oliveira-Costa A., 1998, ApJ, 500, L83

Testori J. C., Reich P., Reich W., 2008, A&A, 484, 733

The Planck Collaboration, 2006, ApJ, 1–152

Uyaniker B., Fuerst E., Reich W., Reich P., Wielebinski R., 1998, A&AS, 132, 401

Valls-Gabaud D., 1998, Publications of the Astronomical Society of Australia, 15, 111

Vinyaikin E. N., 2007, Astronomy Reports, 51, 570

Watson R. A., Rebolo R., Rubiño-Martín J. A., et al., 2005, ApJ, 624, L89

Weiland J. L., Odegard N., Hill R. S., et al., 2011, ApJS, 192, 19

Wolleben M., Landecker T. L., Reich W., Wielebinski R., 2006, A&A, 448, 411

Wolleben M., Reich W., 2004, A&A, 427, 537

Wright E. L., Mather J. C., Bennett C. L., et al., 1991, ApJ, 381, 200

Wu J. H. P., Zuntz J., Abroe M. E., et al., 2007, ApJ, 665, 55

Ysard N., Verstraete L., 2010, A&A, 509, A12

Zainal Abidin Z., Leahy J. P., Wilkinson A., Reich P., Reich W., Wielebinski R., 2003, ApJ, 1–9

Zaldarriaga M., Spergel D. N., Seljak U., 1997, ApJ, 488, 1